AN ABSTRACT OF THE THESIS OF

Christopher Johnson for the degree of Master of Science in Ocean, Earth and Atmospheric Sciences presented on March 12, 2015.

Title: Bright Air: Geoprocessing Thermal Imagery to Map the Nocturnal Dynamics of the Boundary Layer in a Mountain Valley

Abstract approved: ____

Christoph K. Thomas

A thermal infrared (TIR) camera is used to remotely sense the foliage temperature in a mountain valley. The foliage temperature is used as a proxy for air temperature and can be used to study and map the dynamics of the nocturnal, weak-wind boundary layer in this valley. All radiative flux not originating from the forest canopy must be filtered out of the captured imagery. Once the image has been filtered it must be georeferenced and orthorectified before useful analyses can be performed. After geoprocessing is complete, a spatially explicit time series of temperatures for an entire forested mountain valley will be available for further exploitation. The geoprocessed thermal imagery can, when combined with various data recorded *in situ*, yield data sets such as sensible heat flux at the canopy surface, potential temperature profiles, the adiabatic lapse rate in the watershed, the state of static stability in the watershed, and to map cold-air pool dynamics. Evidence was established that two concepts underlying the Bright Air study are valid for this study site. The first is that a TIR camera can accurately record foliage canopy temperature. The second is that on clear nights, foliage canopy temperature can be a proxy for the temperature of air immediately adjacent to the canopy. This study indicates that a TIR camera can accurately measure foliage canopy temperature on clear nights. Furthermore, the study indicates that on clear or intermittently cloudy nights, foliage canopy temperatures as measured by a TIR camera can be a proxy for the temperature of air immediately adjacent to the canopy. A process to georeference and orthorectify thermal imagery was selected and a tool to geoprocess the thermal imagery was created. Vertical profiles of potential temperature in the study area were created for times of interest and classified according to flow regimes. Dominant

flow regimes were found to correlate well with earlier studies. Cold-air pool formation and drainage evolution were characterized for several clear nights. Nocturnal cold-air dynamics in the study area do not agree with common explanations of behavior of cold-air pools and drainage in mountain valleys. Up-valley flow patterns in the watershed indicate that nocturnal flows in mountain valleys are not driven solely by gravity. For the nights studied, flows in the watershed interact with flows from other connected basins and have identifiable patterns and typical evolutionary stages.

Bright Air: Geoprocessing Thermal Imagery to Map the Nocturnal Dynamics of the Boundary Layer in a Mountain Valley

by
Christopher Johnson

A THESIS

submitted to

Oregon State University

in partial fulfillment of
the requirements for the
degree of

Master of Science

Presented March 12, 2015
Commencement June 2015

Master of Science thesis of Christopher Johnson presented on March 12, 2015

APPROVED:

Major Professor, representing Ocean, Earth and Atmospheric Sciences

Dean of the College of Earth, Ocean and Atmospheric Sciences

Dean of the Graduate School

I understand that my thesis will become part of the permanent collection of Oregon State University libraries. My signature below authorizes release of my thesis to any reader upon request.

Christopher Johnson, Author

ACKNOWLEDGEMENTS

The author expresses sincere appreciation to his major advisor, Christoph Thomas. Members of the committee, Simon de Szoeke, Anne Nolin, and Bill Bogley, also deserve credit for the successful completion of this study. Mark Schulze and Adam Kennedy provided valuable support, guidance, and expertise at several important moments. Funding for this project was provided through National Science Foundation Career Grant 0955444 awarded to Christoph Thomas. Data and facilities were provided by the HJ Andrews Experimental Forest research program, funded by the National Science Foundation's Long-Term Ecological Research Program (DEB 1440409), US Forest Service Pacific Northwest Research Station, and Oregon State University.

TABLE OF CONTENTS

Page

TABLE OF CONTENTS (Continued)

LIST OF FIGURES

<u>Figure</u> <u>Page</u>

LIST OF FIGURES (Continued)

LIST OF TABLES

LIST OF APPENDIX FIGURES

LIST OF APPENDIX TABLES

BRIGHT AIR: GEOPROCESSING THERMAL IMAGERY TO MAP THE NOCTURNAL DYNAMICS OF THE BOUNDARY LAYER IN A MOUNTAIN VALLEY

1 INTRODUCTION

The Biomicrometeorology (BMM) group has been studying the nocturnal boundary layer dynamics of mountain valleys. This study and others such as the valley circulation experiment, an effort to characterize valley-scale air circulation using acoustic ground-based remote sensing, are conducted in support of the Advanced Resolution Canopy Flow Observation (ARCFLO) project. ARCFLO studies how air moves in plant canopies such as crops and forests where winds are usually relatively weak, and how it affects the transport of heat, water, and momentum at a variety of sites with different surface conditions and canopy architecture. Among these sites is the HJ Andrews long term ecological research site. The project is funded by the National Science Foundation. The broader impacts of ARCFLO are improved formulations of surface fluxes for regional and large-scale weather and climate models, as well as dispersion and diffusion models.

In this supporting study a thermal infrared (TIR) camera is used to remotely sense the foliage temperature in a mountain valley. The foliage temperature is used as a proxy for air temperature and serves as a basis to study and map the dynamics of the nocturnal, weak-wind boundary layer in this valley. The camera senses all the radiative flux in its field of view. However, not all of the flux sensed will have originated from the object of interest which, in this case, is the forest canopy. All flux not originating from the forest canopy must be filtered out. Once the image has been filtered it must be georeferenced and orthorectified before useful analyses can be performed. After geoprocessing is complete, the BMM group will have an orthorectified and spatially referenced time series of valley temperatures for an entire forested mountain valley. The geoprocessed thermal imagery, when combined with various data recorded *in situ*, can yield datasets such as sensible heat flux at the canopy surface, dry bulb and potential temperature profiles, the adiabatic lapse rate in the watershed, the state of static stability in the watershed, and to map cold air pool dynamics.

Spatially referenced temperature information is used as an input for climate models (Daly *et al.*, 2008). Analyzing and improving crop growth depends on knowledge of spatially referenced temperature data (Bonnardot *et al.*, 2002). More accurately characterizing boundary layer dynamics by helping close the surface energy balance may demand larger scale spatially referenced temperature data (Foken, 2008). Among other areas, Frei (2014) counts runoff forecasting, flood estimation, soil moisture monitoring, and snow cover analysis as areas where spatially referenced temperature information is essential. Spatially referenced temperature data may contribute to the understanding of how of the impacts of climate change on the frequency and degree of cold air pools will affect species distribution and diversity (Daly *et al*., 2010).

Remotely sensed TIR data have been used to derive foliage canopy temperatures since at least 1980 (Soer, 1980). Studies have used satellite based TIR data to derive surface energy fluxes such as sensible and latent heat flux (e.g. Kustas and Norman, 1997, Moran *et al*., 1997, Matsushima and Kondo, 2000). Moran (1997) used remotely sensed satellite data but did not explicitly correct for atmospheric effects on the thermal information. Instead a previously determined function relating satellite sensor based recorded radiance and ground temperature was used to correct for atmospheric effects. Other remotely sensed satellite data is corrected using an algorithm that incorporates atmospheric information (e.g.Matsushima and Kondo, 2000). However, the algorithm uses standardized atmospheric measurements, not measurements that are spatially and temporally coincident with the measurements acquired at the satellite. Other studies that have used TIR cameras to record temperature differences (e.g. Leuzinger and Körner, 2007, Leuzinger *et al*., 2010) correct only for emissivities and do not correct for other effects. This study explicitly corrects for atmospheric effects using information from atmospheric measurements that temporally and spatially coincide with the acquired TIR measurements.

The spatial scale of temperature data acquired in this study bridges the gap between scales of existing datasets acquired by TIR cameras. At scales of less than 1 m^2, studies have measured temperature values of leaves for potential use in calculating leaf area index (e.g. Nölke *et al*., 2015). The effects of temperature on crop growth at the scale tens to hundreds of square meters have been reviewed (e.g. Bonnardot *et al.*, 2002, Blum *et al*., 1982). Other researchers have mounted TIR cameras on cranes and measured temperatures at the multi-tree scale, 3000 m^2, to determine how tree species diversity affects canopy leaf temperatures (e.g. Leuzinger and Körner, 2007). Various satellite based TIR sensors have been in use since the 1960's and acquire regional and planetary scale data at spatial resolutions that range from 30 m pixels to kilometer scale pixels. In this study the area of interest is approximately 900,000 m^2 and the spatial resolution is between one and ten square meters per pixel.

The method developed to obtain a spatially referenced temperature map in this study is novel. The temperatures and their associated spatial information are directly recorded. A more traditional approach is to obtain multiple point temperature measurements in a given area and to spatially interpolate the data using various statistical methods. Reviews of traditional methods of kilometer grid square and larger spatial interpolation approaches can be found in the literature (DeGaetano, 2007, Frei, 2014, Courault and Monestiez, 1999). Others have applied these methods at smaller scales (e.g. Thomas, 2011). In summary, there are two traditional approaches. One approach makes temperature at any given location a function of factors such as nearby recorded temperature, the distance from the nearest recorded temperature, the elevation, whether the location of interest is wet or dry, atmospheric circulation patterns, distance from the coast, and the level of urbanization. The other approach is to use spatial interpolation methods such as inverse distance weighting and kriging.

The objective of this study is to use filtered and corrected spatially referenced thermal imagery to describe and map aspects of the dynamics of the nocturnal, weak-wind boundary layer in a mountain valley. I introduce a method to filter, correct, and geoprocess the imagery.

2 THEORY

2.1 RADIANT EXITANCE OF NATURAL OBJECTS

Objects with a temperature above absolute zero emit TIR radiation (Nölke *et al.*, 2015). This study focuses on a portion of the electromagnetic spectrum in the TIR band between 7.5 and 13 µm. What follows is a summary of applicable definitions and laws governing TIR radiation.

The energy of particles of molecular matter in random motion is called kinetic heat. The amount of kinetic heat can be measured. The concentration of this heat is called the true kinetic temperature (Jensen, 2007). A blackbody is a theoretical construct that absorbs all the radiation that falls on it and radiates energy at the maximum possible rate per unit area at each wavelength for any given temperature (Jensen, 2007). Nature contains objects that radiate at a rate that is a proportion of the rate at which a blackbody radiates for a given temperature and wavelength. The radiant flux density leaving a surface per wavelength as measured in W m^{-2} is called spectral radiant exitance. The radiant flux density incident upon a surface per wavelength as measured in W m^{-2} is called spectral irradiance. The total radiant exitance from a blackbody per wavelength is given by the Stefan-Boltzmann law:

$$M_\lambda = \sigma T^4 \qquad (1)$$

where M_λ [W m^{-2}] is the spectral radiant exitance leaving a surface, σ [W m^{-2} K^{-4}] is the Stefan-Boltzmann constant, 5.67 x 10^{-8}, and T [K] is the dry bulb temperature of an object (Jensen, 2007). Emissivity, ε, is the ratio between the actual spectral radiant exitance, M_r [W m^{-2}], emitted by a real world object and the spectral radiant exitance emitted by a blackbody, M_b [W m^{-2}] at the same kinetic temperature:

$$\varepsilon = \frac{M_r}{M_b} \qquad (2)$$

For this study, it is assumed that an object has a constant emissivity in our spectral band of measurement.

The general equation for the interaction of spectral radiant flux [W] with the terrain is:

$$\Phi i = \Phi r + \Phi \alpha + \Phi \tau \tag{3}$$

where Φ_i is the spectral radiant flux incident on the surface, Φ_r is the spectral radiant flux reflected by the surface, Φ_α is the spectral radiant flux absorbed by the surface, Φ_τ is the spectral radiant flux transmitted through the surface. Dividing each term by Φ_i and changing the notation to a widely recognized form gives:

$$1 = r + \alpha + \tau \tag{4}$$

where r is the spectral hemispherical reflectance by the surface, α is the spectral hemispherical absorptance by the surface, and τ is the spectral hemispherical transmittance through the surface. The Russian physicist Kirchoff found that the spectral emissivity of an object generally equals its spectral absorptance. Most real world objects are opaque to TIR radiation, $\tau = 0$ (Jensen, 2007). Thus, from Kirchoff's Law:

$$1 = r + \varepsilon \tag{5}$$

2.2 LEAF AND AIR TEMPERATURE EQUILIBRIUM

Noble (2012) developed a leaf energy balance. The difference between the energy input to and output from a leaf is equal to the energy stored in a leaf. Energy inputs are absorbed insolation, water condensing on the leaf, and absorbed TIR radiation reflected from or emitted by the leaf's surroundings. Energy outputs are heat convection, heat conduction, emitted TIR radiation, and latent heat loss. The storage term consists of photosynthesis, other metabolism, and temperature changes. Noble (2012), noting that individual plants and environments have tremendous variability, showed that in general leaf energy storage terms are relatively small and can be ignored.

This study is concerned with clear sky nocturnal dynamics, so the leaf energy balance will be adapted to typical conditions for these types of nights. On nights when air and leaf temperatures are above the dew point no water will condense on the leaf. At night stomata are generally closed (Noble, 2012). This implies a minimized loss of latent heat at night. Kirchoff's work indicated that the spectral emissivity of an object generally equals its spectral absorptance when the object is in equilibrium with its environment. These facts lead to the conclusion that leaf temperature at night depends on conduction and convection between the leaf and surrounding air. Conduction is driven by temperature gradients. This method of heat transfer is important in the processes leading to cold air pooling and drainage described in 2.3. In fact, these drainages and pooling give rise to the process which ultimately determines the energy balance at the leaf, convection.

The convective transfer coefficient [W m^{-2} K^{-1}], h_c, increases with increasing wind velocity (The Engineering Toolbox, 2015a). A time constant for equilibrium between the leaf and the air based on convective heat transfer is defined as follows:

$$\tau = \frac{c_p \rho V}{h_c A} \qquad (6)$$

Here τ [s] is the time constant to equilibrium, c_p [J kg^{-1} K^{-1}] is specific heat at constant pressure, ρ [kg m^{-3}] is density, V [m^3] is leaf volume, and A [m^2] is leaf area. As wind speed increases so does h_c. This results in a shorter time to equilibrium between the leaf and the surrounding air. Smaller leaf volume to area ratios also result in shorter times to equilibrium. Time constants for leaves in the study area are on the order of seconds.

2.3 NOCTURNAL BOUNDARY LAYER DYNAMICS OF MOUNTAIN VALLEYS

2.3.1 INVERSIONS

An inversion is a layer of air where dry bulb temperature increases with height (Wallace and Hobbs, 2006). This structure results in a statically stable layer of air. The stability inhibits vertical mixing (Daly *et al*., 2010). An inversion can also be defined in terms of potential temperature. Potential temperature typically increases with height. An inversion is indicated where the magnitude of the increase with height of potential temperatures is larger than normal. Wallace and Hobbs (2006) give the following equation (Poisson's equation) to calculate potential temperature:

$$\theta = T\left(\frac{p_0}{p}\right)^{\frac{R}{c_p}} \qquad (7)$$

In equation 7, Θ is potential temperature [K], T is temperature [K], p is pressure [Pa], p_0 is the reference pressure [Pa], R is the gas constant for dry air [J K^{-1} kg^{-1}], and c_p is the specific heat of dry air at constant pressure [J K^{-1} kg^{-1}].

To determine atmospheric pressure that spatially and temporally corresponds with the potential temperature information, the following form of the hypsometric equation was used:

$$p = p_0 e^{-\left(\frac{z}{\frac{R\bar{T}}{g}}\right)} \qquad (8)$$

In equation 8, p is the pressure [Pa], p_0 is the reference pressure [Pa], z [m] is the elevation at the point in space where the pressure is derived, R is the gas constant for dry air [J K^{-1} kg^{-1}], g is acceleration due to gravity [m s^{-2}], and $\bar{T}$ is the temperature that spatially corresponds to the location where the pressure is to be determined.

2.3.2 COLD-AIR POOLS AND DRAINAGE

A cold-air pool is a topographic depression filled with cold air (Lareau *et* al., 2013). Cold-air pools begin to form in valleys during the transition from day to night when the Earth's surface begins to cool radiatively (Mahrt *et al.*, 2010, Whiteman, 2000b). The compensating sensible heat flux from the air to the ground results in a cooler denser layer of air near the surface. This cooler denser layer drains and is replaced by warmer air from aloft (Daly *et al*., 2010). The cycle is repeated. This forms the common explanation of nocturnal flow in a mountain valley. The flow is typically downslope and down-valley and is gravity driven (Whiteman, 1990, Whiteman, 2000b, Pypker *et al.*, 2007a). Daytime flows are typically up-valley due to a flux of sensible heat from the ground to the air that causes convective currents (Whiteman, 2000b).

Cold air pools are inversions. The static stability resulting from the inversion can prevent vertical mixing. In this way cold air pooling can result in a decoupling between the pool and free atmosphere above (Daly *et al*., 2010). The topography of the depression containing the pool can prevent lateral flow. The lack of vertical mixing due to decoupling and the prevention of horizontal flow due to topography can lead to stagnant air (Lareau *et* al., 2013). In urban environments the lack of dilution and diffusion of air pollutants can lead to poor air quality (Whiteman, 2000b). In rural environments cold air pools can affect species phenology, distribution, and diversity (Daly *et al*., 2010).

3 MATERIALS AND METHODS

3.1 STUDY SITE LAYOUT

The study location was Watershed 1 at the HJ Andrews Experimental Forest. Watershed 1 is oriented along an east-southeast axis, and drains to Lookout Creek Valley at its northwestern outlet (Figure 1). The watershed is approximately 1.5 km in length along its east-southeast axis. Its width varies from approximately 1 km along Lookout Ridge to approximately 100 m at its northwestern outlet. The height difference between Lookout Ridge and the lowest point in the watershed is approximately 550 m. The majority of the watershed is forested. Detailed descriptions of the site's biology can be found in Pypker *et al.*, (2007) and of its geology in Swanson (1975). Places on the north side of the valley and the southeast corner are exposed rock.

As shown in Figure 2, the TIR camera, directed toward the east-southeast, overlooked the watershed. The camera was mounted in a tree approximately 36 m above ground level (AGL). The camera was contained in a fan-ventilated housing (Figure 3). The camera's lens was embedded in a black Delrin baffle machined to fit in the front of the camera housing. The baffle was equipped with a germanium window (63-215, Edmund Optics, Barrington, New Jersey, USA) that had a coating designed to maximize its transmissivity in the 8 -12 μm range of the electromagnetic spectrum. The window's temperature was recorded by proxy by a thermocouple (H08-031-08, Onset Computer Corporation, Bourne, Massachusetts, USA) embedded in the baffle. The camera housing, set up, and associated sensors are identical to that used for camera calibration as described in 3.3.1.3.

A flux and meteorological tower is located in Watershed 1. Temperature sensors are installed at 29m (roughly the canopy height) and 37m AGL. Water vapor pressure and atmospheric pressure sensors are installed at 37 m AGL. Pyranometers and pyrgeometers are mounted at 37 m AGL. Sonic anemometers were mounted at 4 and 37 m AGL.

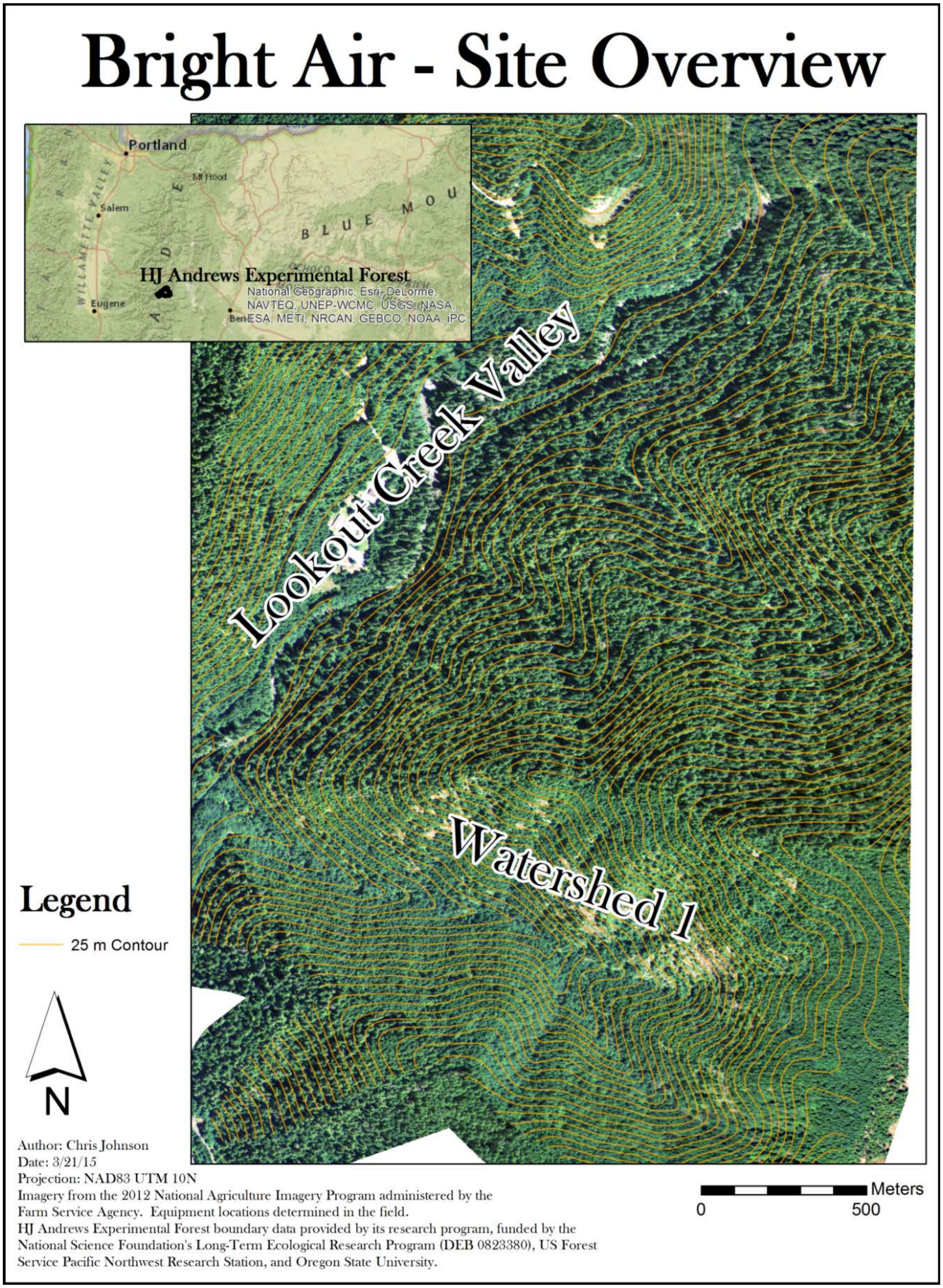

Figure 1: Site overview of Lookout Creek Valley and Watershed 1 in the HJ Andrews Experimental Forest.

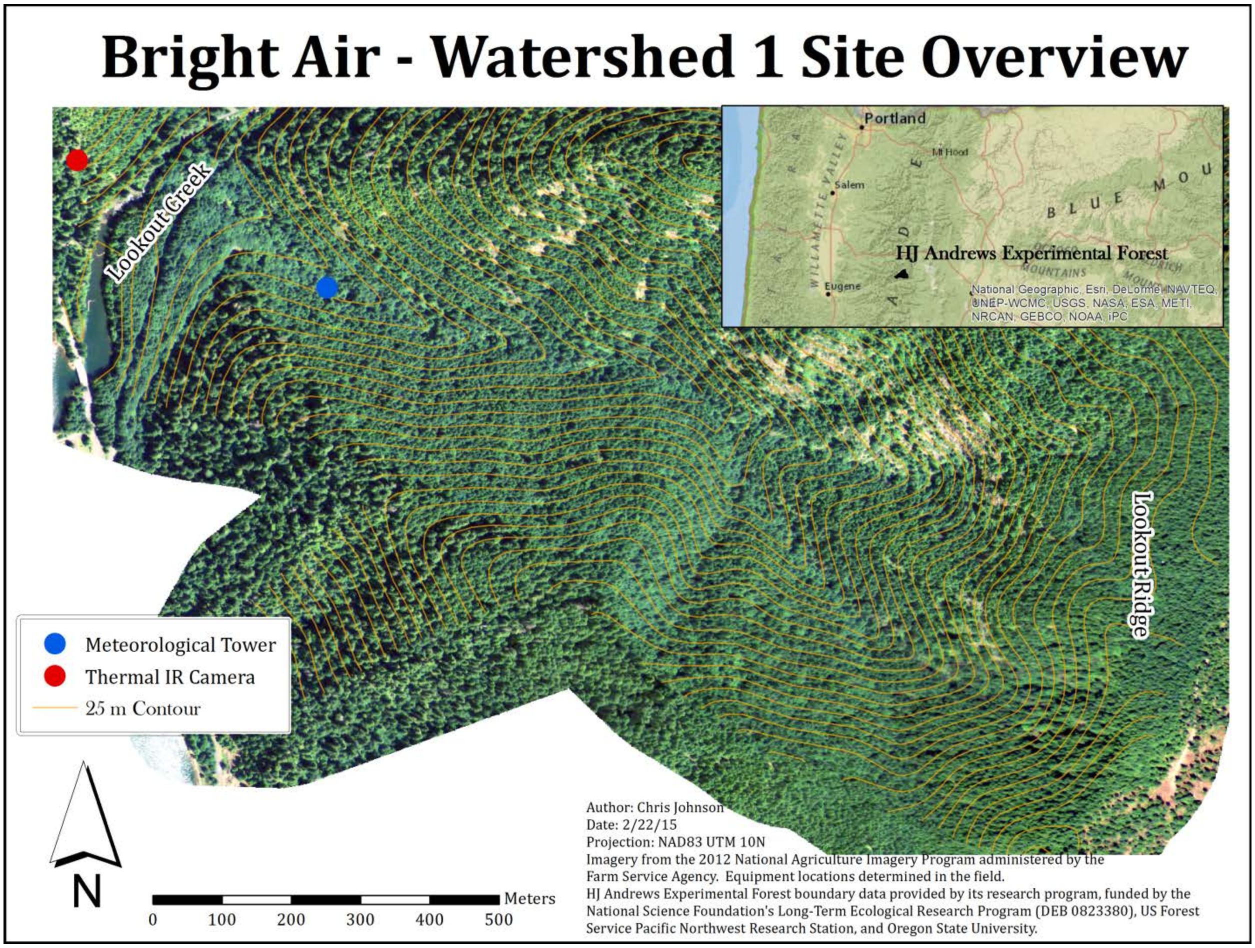

Figure 2: A site overview of Watershed 1 in the HJ Andrews Experimental Forest.

Figure 3: The camera was contained in a fan-ventilated housing. The camera's lens was embedded in a black Delrin baffle machined to fit in the front of the camera housing. The baffle was equipped with a germanium window that had a coating designed to maximize its transmissivity in the 8 -12 µm spectral range.

3.2 STUDY SITE INSTRUMENTATION

The FLIR SC305 camera uses an uncooled microbolometer to detect TIR radiation at wavelengths between 7.5 and 13µm. It has a resolution of 320 x 240 pixels. The accuracy of the camera is ±2 K or ±2% of the reading (FLIR, 2013). The camera acquired instantaneous measurements at one-minute intervals during the study period. Each pixel in the image has a temperature value associated with it. With the exception of an internal, automatic, and unmonitored correction for the body temperature of the camera itself, no corrections are incorporated into the data reported by the camera. The data analyzed for this study were acquired using a lens with a 25° × 18.8° field of view. A wider angle lens with a 45° × 33.8 field of view was used in subsequent portions of the Bright Air study.

The Hukseflex NR01 four component net radiation sensor consists of a downward facing pyranometer/pyrgeometer pair that measures radiation from the surface, an upward facing pyranometer/pyrgeometer pair that measures incoming radiation, and a resistance temperature detector that measures the device's internal temperature. The SR01 pyranometers detect short-wave radiation between 305 nm and 2800 nm. The IR01 pyrgeometers measure far infrared longwave radiation between 4,500 nm and 50,000 nm. The accuracy of the NR01 is ±10% (Huskeflux, 2013). The data recorded by the devices was sampled at 10 second intervals and subsequently linearly averaged to one-minute intervals for use in this study. As with the TIR camera, the longwave radiation sensors corrected for the device's body temperature before reporting its data.

A HOBO Pro Data Logger with external temperature sensor (Model H08-031-08) monitored the temperature of a Delrin baffle in the camera housing. The accuracy of the external temperature sensor over the range of temperatures encountered in this study is approximately ±0.17 K (Onset Computer Corporation, 2003). The external temperature sensor recorded instantaneous data at five-minute intervals. Its time constant is 122 ± 6 s (Whiteman *et al.*, 2000a). No corrections internal to the device were made.

Dry bulb temperatures at 29 m and 37 m AGL were recorded at one-minute intervals. Temperatures were recorded by a Campbell Scientific model 107 temperature probe contained in a double-walled aspirated radiation shield as described by Thomas and Smoot (2013). The accuracy of the thermistor over the range of temperatures encountered in this study is approximately ±0.4 K (Campbell Scientific, 2014).

Atmospheric pressure values were averaged across fifteen-minute intervals. Pressure values were measured with a Setra model 278 barometer. The accuracy of the barometer over the range of pressures encountered in this study is approximately ±60 Pa (Setra, 2011).

Water vapor pressure values were aggregated across fifteen-minute intervals and were measured with a Picarro G1101-i gas analyzer. The company datasheets do not report accuracies associated with these measurements.

Above canopy and sub-canopy wind speed and direction values were measured using sonic anemometers located on the flux and meteorological tower in Watershed 1. Above the canopy the sensor was located 37 m AGL and consisted of a Gill Instruments model R2 sonic anemometer. Its sampling frequency was 20.82 Hz and its output frequency was 20 Hz. In the sub-canopy at 4 m AGL a R.M. Young 81000 sonic anemometer was used. Its sampling frequency was 32 Hz and its output frequency was 20 Hz. All sonic anemometer data were averaged to one minute values for analysis.

The time interval of the dataset derived from these sensors matched the lowest frequency aggregated data. Data were analyzed at 15 minute intervals.

3.3 STUDY CONCEPT AND DESIGN

A method to filter and correct measurements acquired by the TIR camera and the tower-mounted pyrgeometer is presented in this section. The methodology is presented as an explanation of process and a proof of concept for the study. The geoprocessing method is then presented. Methods for using the resulting spatially referenced temperature data to describe and map aspects of the dynamics of the nocturnal, weak-wind boundary layer in a mountain valley are then explained.

3.3.1 FILTERING AND CORRECTING TIR MEASUREMENTS

Two concepts underlie the Bright Air study. Those concepts are:

1. A TIR camera can accurately record foliage canopy temperature.

2. On clear nights foliage canopy temperature can be a proxy for the temperature of air immediately adjacent to the canopy.

Proving the concepts will provide evidence for and greater confidence that any conclusions based upon the results of the study itself are reliable. This study builds upon fieldwork done in spring 2013 and a subsequent study of the calibration of the TIR camera used in the Bright Air study. The proof of concept compares foliage temperatures derived from two different sensors, a TIR camera (SC305, FLIR, Wilsonville, Oregon, USA) and a pyrgeometer (NR01, Huskeflux, Delft, Netherlands), for the same spatial area in the HJ Andrews Experimental Forest in Oregon, USA during a period of clear, cool nights in September 2013.

The methodology of this proof of concept is:

- Develop a process to compare foliage temperatures derived from a TIR camera to those derived from a pyrgeometer

- Prepare and incorporate time series data of air pressure, water vapor pressure, dry bulb air temperature, short wave radiant flux density, longwave radiant flux density, thermal imagery, and TIR camera enclosure dry bulb temperature into a process that seeks to compare foliage temperatures derived from two different sensors

- Determine a method to develop a time series of atmospheric TIR emissivity values for use in the analysis, derive the emissivity values, and compare the derived values to other studies for validation

- Determine accepted forest canopy TIR emissivity values for use in the analysis

- Compare foliage temperatures derived from a TIR camera to those derived from a pyrgeometer

- Compare foliage temperatures derived from TIR camera to those measured by an *in situ* air dry bulb temperature sensor

3.3.1.1 CAMERA-PYRGEOMETER TEMPERATURE COMPARISON SCHEME

As shown in Figure 4, the Watershed 1 flux and meteorological tower is within the TIR camera field of view. To show that a TIR camera can accurately record foliage canopy temperature, temperatures can be derived from the tower mounted downward facing pyrgeometer measurements and compared to those derived from the TIR camera. The pyrgeometer mounted near the top of the tower integrates all the longwave radiation in its 150° field of view to derive a temperature that is a spatial average. To directly compare a pyrgeometer derived temperature to one derived from the camera:

1. A spatially and temporally corresponding group of pixels from the thermal imagery must be extracted.

2. Each data point from both datasets must be corrected for various TIR effects (described in section 3.3.1.2).

3. A previously determined calibration function must be applied to the corrected camera data (described in section 3.3.1.3).

ExamineIR is proprietary thermal image processing software that accompanies the FLIR SC305 camera. This software is used to export data acquired by the camera. After exporting the data from ExamineIR, Python was used to call ArcGIS to extract the correct group of pixels from each one-minute interval image. Before exporting the time series of raw temperatures from ArcGIS and Python, the values from the pixels were spatially averaged. This dataset and time series data of atmospheric radiative and thermodynamic properties to make corrections for various TIR effects (described section 3.3.1.2) were imported into Matlab. The resulting values were then corrected using a

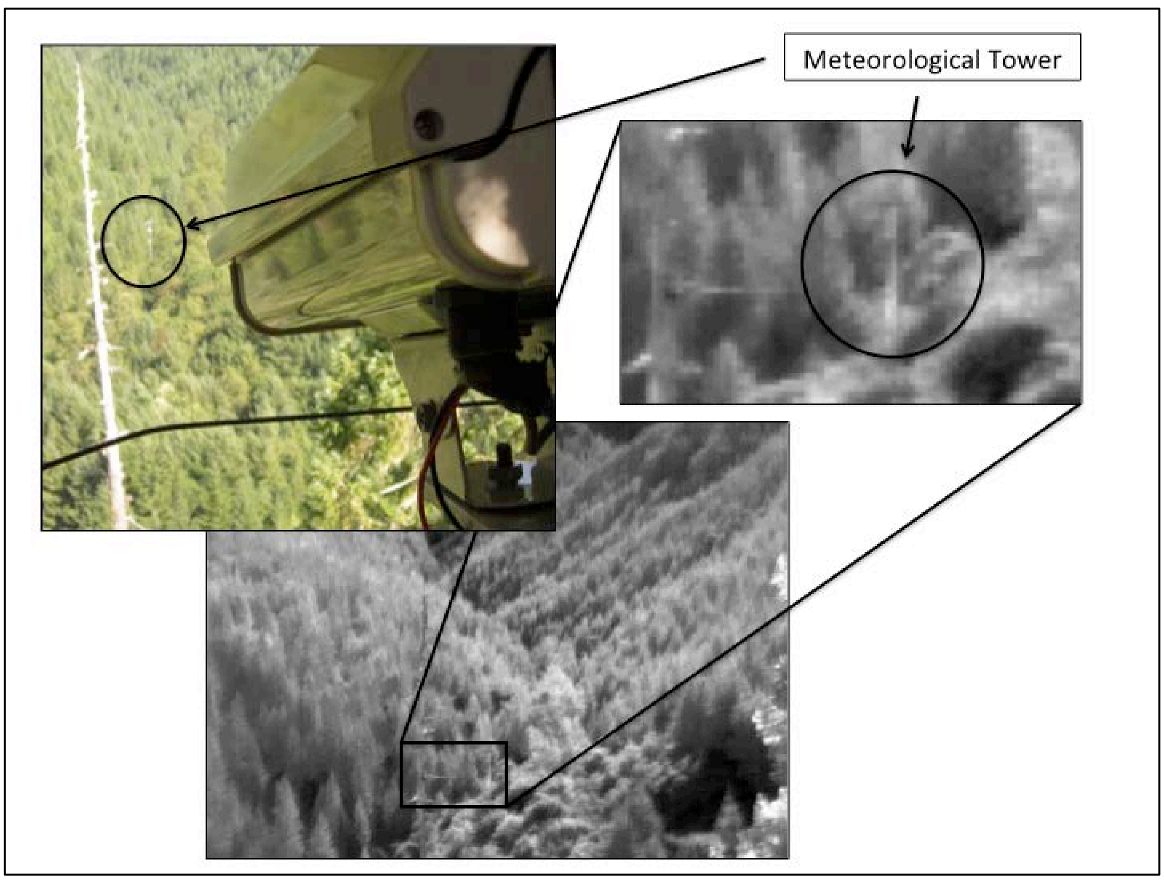

Figure 4: The Watershed 1 meteorological tower is within the TIR camera field of view. A visible spectrum photo in the upper left and grey scale thermal images show the tower. To compare pyrgeometer and camera derived temperatures, a spatially appropriate group of pixels must first be extracted from each thermal image.

calibration function developed in the lab during a TIR camera calibration study. This final corrected time series of camera derived foliage temperature values was compared to pyrgeometer derived temperature values, which were themselves corrected for TIR effects. This workflow is shown in Figure 5.

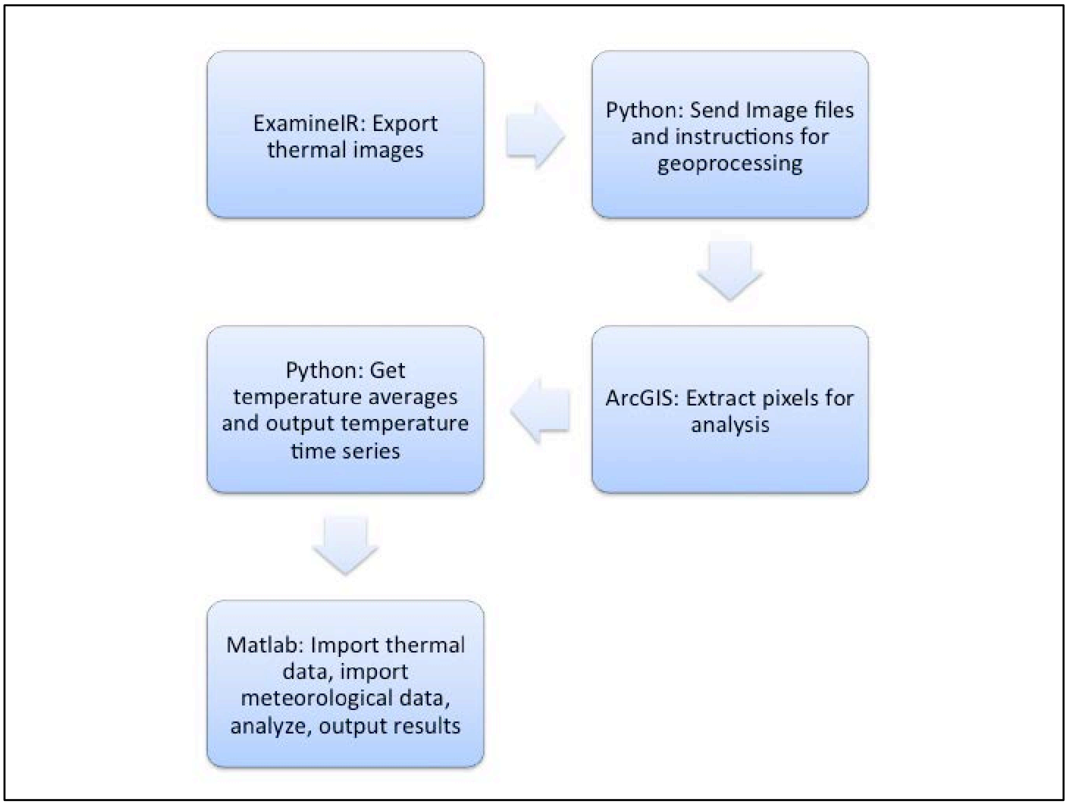

Figure 5: The data flow for processing thermal imagery begins with extracting imagery from ExamineIR. A python script is then used to call ArcGIS to extract the relevant portion of the images. The python script averages temperature values associated with each group of extracted pixels and writes the information to a text file along with its timestamp. A Matlab script uses this data, along with a host of other meteorological data, to compare the derived temperatures.

3.3.1.2 CAMERA CORRECTION METHOD

The radiant flux density [W m^{-2}] incident at the camera in the 7.5 μm to 13 μm spectral range, M_{cam}, is the sum of the radiant exitance in the same spectral range from the foliage canopy, M_{fol} [W m^{-2}], reflections off of the foliage canopy, M_{ref} [W m^{-2}], the atmospheric air in the camera's field of view, M_{atm} [W m^{-2}], and the germanium window in the camera housing, M_{win} [W m^{-2}].

$$M_{cam} = M_{fol} + M_{ref} + M_{atm} + M_{win} \tag{9}$$

Using the Stefan-Boltzman law and Kirchoff's law, the terms in equation 9 can be defined as follows:

$$M_{fol} = \varepsilon_{fol}\tau_{atm}\tau_{win}\sigma T_{fol}^4 \tag{10}$$

In equation 10, ε_{fol} is the emissivity of the foliage in the camera's spectral range, τ_{atm} is the transmissivity of the atmosphere in the camera's spectral range, τ_{win} is the transmissivity of the germanium window in the camera's spectral range, σ is the Stefan-Boltzman constant [5.67 $\times 10^{-8}$ W m^{-2} K^{-4}], T_{fol} is the temperature of the foliage canopy [K].

$$M_{ref} = \rho_{fol}\tau_{atm}\tau_{win}\left(\frac{M_{sky}}{\sigma\varepsilon_{atm}}\right) \tag{11}$$

In equation 11, ρ_{fol} is the reflectivity of the foliage in the camera's spectral range, ε_{atm} is the emissivity of the atmosphere in the camera's spectral range, and M_{sky} is the radiant exitance of the sky [W m^{-2}] in the camera's spectral range.

$$M_{atm} = \varepsilon_{atm}\tau_{win}\sigma T_{atm}^4 \tag{12}$$

In equation 12, T_{atm} is the temperature of the atmosphere [K].

$$M_{win} = \varepsilon_{win}\sigma T_{win}^4 \tag{13}$$

In equation 13, T_{win} is the temperature of the germanium window [K].

$$M_{cam} = \sigma T_{cam}^4 \tag{14}$$

In equation 14, T_{cam} is the temperature as recorded by the camera [K].
Solving for T_{fol} yields the following relationship:

$$T_{fol} = \left[\frac{T_{cam}^{4} - \rho_{fol}\tau_{atm}\tau_{win}\left(\frac{M_{sky}}{\sigma\varepsilon_{atm}}\right) - \varepsilon_{atm}\tau_{win}T_{atm}^{4} - \varepsilon_{win}T_{win}^{4}}{\varepsilon_{fol}\tau_{atm}\tau_{win}}\right]^{\frac{1}{4}} \qquad (15)$$

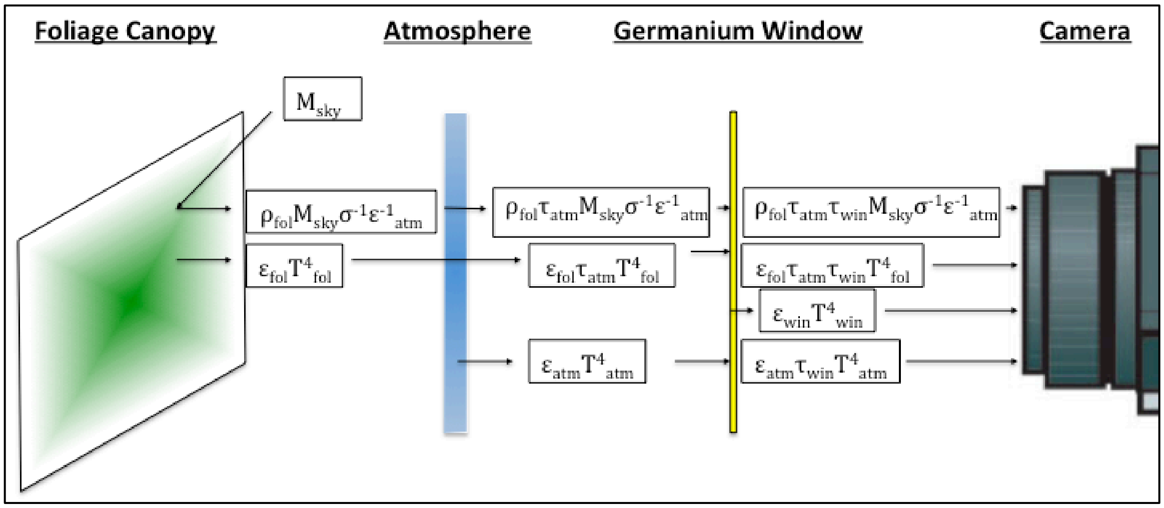

Figure 6: A conceptual representation depicting the foliage canopy, atmosphere, window, and thermal reflections sensed by the camera.

3.3.1.3 CAMERA CALIBRATION

A calibration function for the TIR camera used in the Bright Air study was established. The details of the statistical analysis are included as an appendix to this document. Field use of the camera in spring 2013 seemed to indicate that the temperatures recorded by the camera, even after correcting the data for longwave radiation sensed by the camera but not emitted by the object of interest, were systematically incorrect. During times of increasing temperatures the camera reported temperatures that, in general, increased at a greater rate and arrived at a greater maximum than those returned by other sensors measuring the same object. During times of decreasing temperatures the camera reported temperatures that, in general, decreased at a greater rate and arrived at a lower minimum than those returned by other sensors measuring the same object.

To calibrate the camera the following tasks were performed:

- Prepare and analyze two time series of temperature data and determine if there is a function that describes their relationship.

- Perform a statistical analysis of the relationship to establish its reliability for use as a correction for other data collected by the same TIR camera.

3.3.1.3.1 SET UP AND DATA

The data used for this analysis were collected between March 16th and 18th, 2014, at the Biomicrometeorology lab at Oregon State University. Two temperature sensors, shown in Figure 7, measured the same object as it was alternately heated and cooled. A temperature probe (RTD 810, Omega, Stamford, Connecticut, USA) was inserted in a piece of black Delrin plastic that was concurrently monitored by a TIR camera (SC305, FLIR, Wilsonville, Oregon, USA). The Delrin being monitored was affixed to the base of a black Delrin plastic tube and submerged in common automobile coolant. The coolant was contained in a refrigerator unit that was also equipped with a heating element.

The 3-wire temperature probe was used as a measure of the true kinetic temperature of the object. The sensor contains a 100 Ohm Class A DIN platinum element. The platinum element's resistance has a non-linear response to changes in temperature, so the probe's lead wire was connected to a linearizer (OM5-IP4-100-C, Omega, Stamford, Connecticut, USA). The linearizer's voltage output was in turn fed into a data logger (CR3000, Campbell Scientific, Logan, Utah, USA). The data logger's recorded information was accessed via Campbell Scientific's Loggernet 4.1 software. The data logger reported moving one minute averages for the temperature probe.

As shown in Figure 8, the TIR camera was contained in a fan ventilated housing and affixed to a mounting system that facilitated positioning the camera at the upper opening of the Delrin tube. The TIR camera recorded instantaneous images at one minute intervals. The camera's lens was embedded in a black Delrin baffle machined to fit in the front of the camera housing. The baffle was equipped with a germanium window (63-215, Edmund Optics, Barrington, New Jersey, USA) that had a coating designed to maximize its transmissivity in the relevant range of the electromagnetic spectrum. The window's temperature was recorded by proxy for later use in performing corrections to the camera's recorded temperatures. A thermocouple (H08-031-08, Onset Computer Corporation, Bourne, Massachusetts, USA) embedded in the baffle served as the proxy.

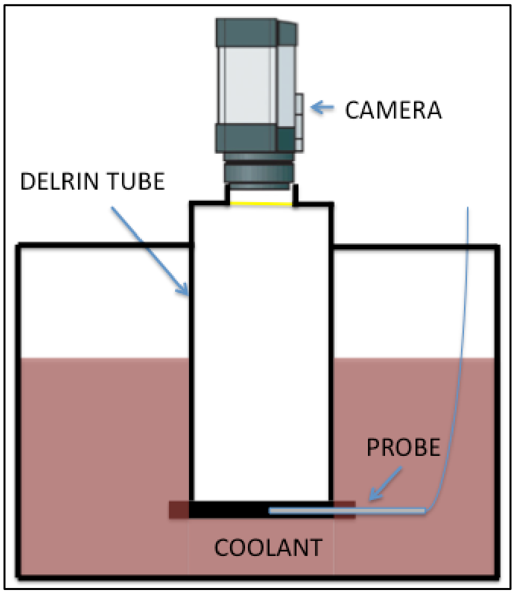

Figure 7: Experimental setup of the camera calibration study.

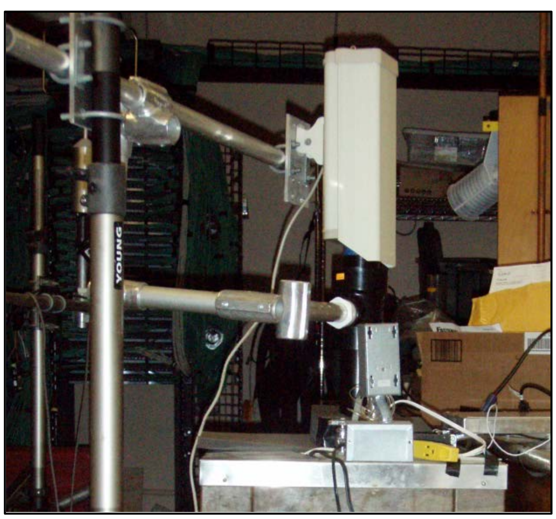

Figure 8: Photo showing camera housing, refrigeration unit, and Delrin tube.

The thermocouple recorded instantaneous temperatures at five minute intervals. The final dataset analyzed was therefore at that frequency.

The camera detects thermal infrared radiation between 7.5 μm and 13 μm. In this study it was assumed that the object being measured had a constant emissivity in that range. It was also assumed, due to the small distance between the camera lens and the object being measured, that any air in the path had a transmissivity of 1 in the relevant spectral range. The camera manufacturer states that the camera self-corrects for any effects of its own temperature. Another assumption is that the Delrin being measured had no horizontal temperature gradient.

Based on these assumptions and the camera's setup, the camera should only sense the radiant exitance, M, of the Delrin being measured, the germanium window, and of thermal reflections (see Figure 9). Lab testing confirmed that this configuration would result in a reflection of the camera's radiant exitance in this range of wavelengths off of the Delrin being monitored.

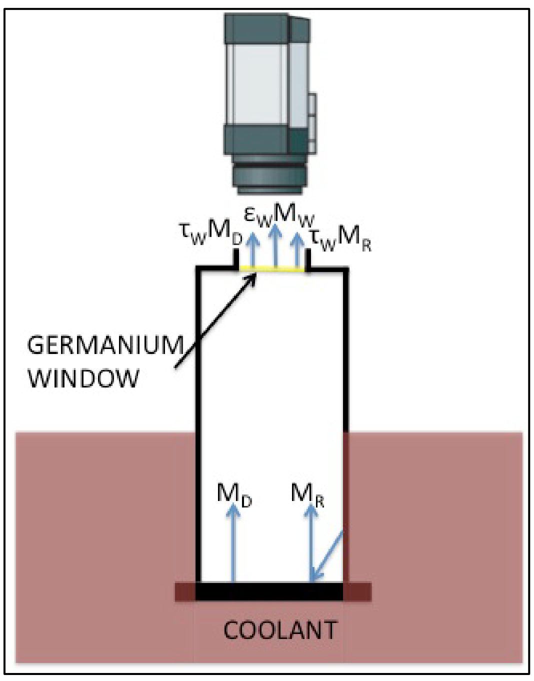

Figure 9: The Delrin, germanium window, and thermal reflections irradiate the camera.

3.3.1.3.2 CAMERA CALIBRATION METHOD

The radiant flux density sensed by the camera, M_{CAM} [W m^{-2}] is assumed to be:

$$M_{CAM} = \tau_W M_R + \tau_W M_D + M_W \tag{16}$$

where τ_W (unitless) is the transmissivity of the germanium window in the range of the spectrum measured by the camera, M is an object's radiant exitance [W m^{-2}], and the subscripts R, D, and W denote reflected, Delrin, and window respectively.

Using the Stefan-Boltzmann law, Kirchoff's law, and solving 16 for the temperature, T_D, of the Delrin being evaluated yields:

$$\left[\frac{T_{CAM}^4 - \tau_W(1-\varepsilon_D)T_R^4 - (1-\tau_W)T_W^4}{\tau_W \varepsilon_D}\right]^{\frac{1}{4}} = T_D \tag{17}$$

where the subscripts R, D, and W again denote reflected, Delrin, and window respectively, ε_D (unitless) is the emissivity of the Delrin in the range of the spectrum measured by the camera, and T is temperature [K].

A review in the lab determined that by carefully choosing pixels in the camera image to use in the analysis, reflected radiant exitance could be minimized. However, processing and subsequent analyses were carried out both including and excluding the reflections. The relationship used to derive the Delrin's true kinetic temperature based on the apparent temperature measured by the camera excluding reflected exitance was:

$$\left[\frac{T_{CAM}^4 - (1-\tau_W)T_W^4}{\tau_W \varepsilon_D}\right]^{\frac{1}{4}} = T_D \tag{18}$$

Figure 10 shows a scatterplot of the data used for the statistical analysis. Initially a simple linear regression was taken as the model. The data were separated by run and evaluated both on a per run basis and as a full set. Probe temperature readings (T_{Probe} in units of degrees Celsius) were regressed on the lagged camera temperature (T_{Cam} in units of degrees Celsius) readings. Each run and the full set were investigated to check for violations of the basic assumptions (linearity, constant variance, normality, independence) used to justify statistical statements based on a regression analysis. A review for serial correlation was also undertaken. This process was repeated for a fuller model that sought to correct for violations of assumptions so as to allow for a more reliable quantification of the uncertainty involved in the regression analysis.

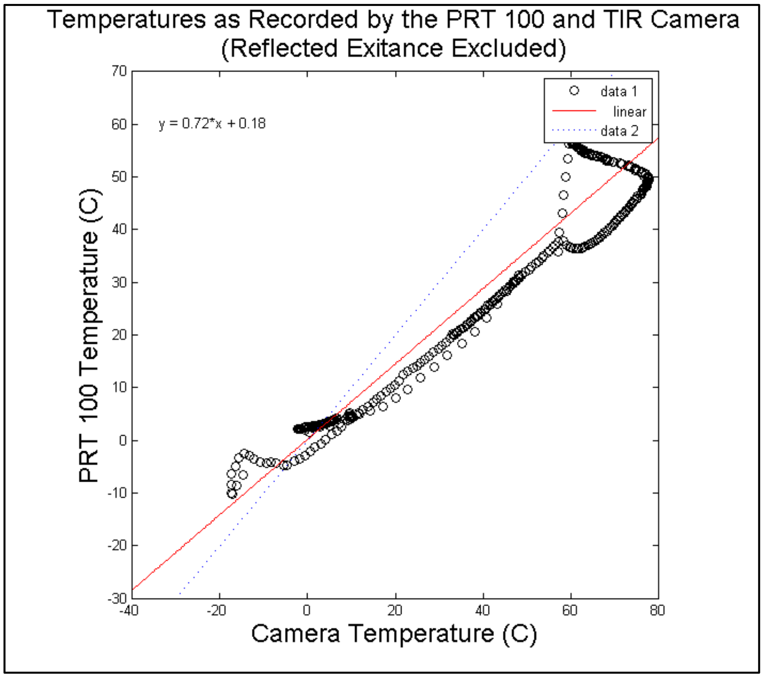

Figure 10: Initial assessment of the data indicated a linear relationship between the two datasets.

The initial model, model 6, is:

$$\mu\{T_{Probe}|T_{Cam}\} = \beta_0 + \beta_1 T_{Cam} \tag{19}$$

The fuller model, model 7, is:

$$\mu\{T_{Probe}|T_{Cam}\} = \beta_0 + \beta_1 T_{Cam} + \beta_2 T_{Cam}^2 \tag{20}$$

The statistical analysis seemed to support the simple linear relationship displayed in Figure 10. All model 6 results were applied to the data during the proof of concept to determine best fit with the physical system. The best fit was the full model 6 that included the camera's radiant exitance term. The calibration function used is the following:

$$T_{Probe} = 6.59 + .61 T_{Cam} \tag{21}$$

In this case T_{Cam} is equivalent to T_{fol} from equation 15. The calibration is applied after all the filtering described in section 3.3.1.2 is carried out so that the relationship used to determine the foliage canopy temperature, T_{fol}, is the following:

$$T_{fol} = 6.59 + .61\left[\frac{T_{cam}^4 - \rho_{fol}\tau_{atm}\tau_{win}\left(\frac{M_{sky}}{\sigma\varepsilon_{atm}}\right) - \varepsilon_{atm}\tau_{win}T_{atm}^4 - \varepsilon_{win}T_{win}^4}{\varepsilon_{fol}\tau_{atm}\tau_{win}}\right]^{\frac{1}{4}} \quad (22)$$

3.3.1.4 PYRGEOMETER CORRECTION METHOD

The radiant flux density [W m^{-2}] incident at the downward facing pyrgeometer in the 4.5 μm to 50 μm spectral range, M_{pyr}, is the sum of the radiant exitance in the same spectral range from the foliage canopy, M_{fol} [W m^{-2}], reflections off of the foliage canopy, M_{ref} [W m^{-2}], and the atmosphere between the foliage canopy and the sensor, M_{atm} [W m^{-2}].

$$M_{pyr} = M_{fol} + M_{ref} + M_{atm} \quad (23)$$

Using the Stefan-Boltzman law and Kirchoff's law, the terms in equation 23 can be defined as follows:

$$M_{fol} = \varepsilon_{fol}\tau_{atm}\sigma T_{fol}^4 \quad (24)$$

$$M_{ref} = \rho_{fol}\tau_{atm}\left(\frac{M_{sky}}{\sigma\varepsilon_{atm}}\right) \quad (25)$$

$$M_{atm} = \varepsilon_{atm}\sigma T_{atm}^4 \quad (26)$$

Solving for T_{fol} yields the following relationship:

$$T_{fol} = \left[\frac{\left(\frac{M_{pyr}}{\sigma}\right) - \rho_{fol}\tau_{atm}\left(\frac{M_{sky}}{\sigma\varepsilon_{atm}}\right) - \varepsilon_{atm}T_{atm}^{4}}{\varepsilon_{fol}\tau_{atm}}\right]^{\frac{1}{4}} \tag{27}$$

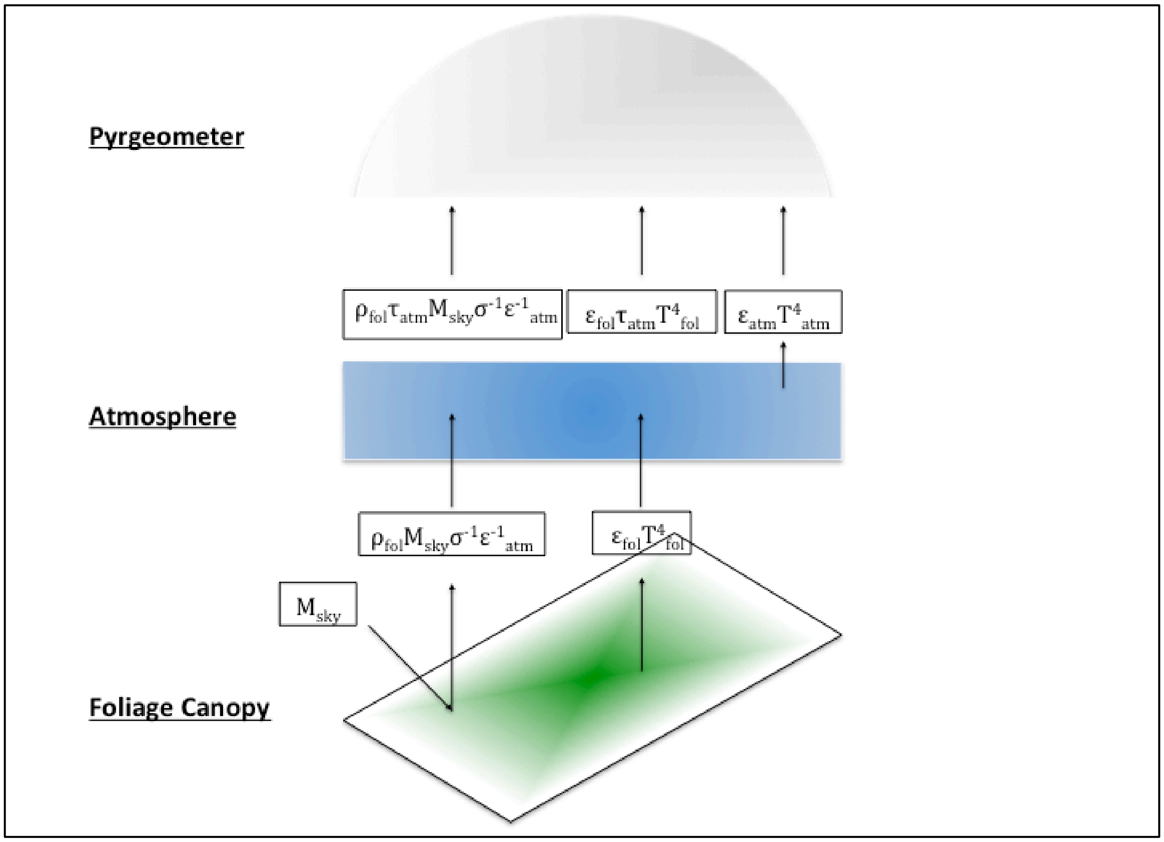

Figure 11: A conceptual representation depicting the foliage canopy, atmosphere, and thermal reflections sensed by the pyrgeometer.

3.3.1.5 ATMOSPHERIC CONDITIONS FOR SENSOR CORRECTIONS

In order to compare equation 22, the camera derived foliage canopy temperature, to equation 27, the pyrgeometer derived foliage canopy temperature, a great deal of information must be available about atmospheric conditions at the study site. Upwelling and downwelling longwave radiation fluxes must be measured. Additionally, TIR properties of the germanium window, the atmosphere, and the foliage canopy must be known or derived. Table 1 contains a summary of parameters used in equations 22 and 27 and the source of the data for each parameter.

Reported vegetation TIR emissivity values are in the range of .95 to 1.0. Canopy emissivity can vary according to soil emissivity, canopy structure, and geometry of measurements (Olioso, 1995). Foliage canopy TIR emissivity was taken to be .98. This accepted value has been used in other studies (Tunick, 2006, Sugita, 1996, French *et al*, 2000) for forest and grass canopies.

Clear sky atmospheric TIR emissivity mainly varies with concentration of water vapor and CO_2 (Siqueira and Katul, 2009). Various methods to estimate TIR atmospheric emissivity values have been investigated, reported, and compared since at least the early 20th century (Idso, 1981; Siqueira and Katul, 2009). The Bright Air study will consider two models. One model was developed by Brutsaert and uses water vapor pressure and surface temperature as parameters to characterize emissivity (Brutsaert, 1975). Brutsaert found that emissivity primarily depends on water vapor pressure. His model accounts for all absorbers over the entire range of the TIR spectrum. The model has been reviewed several times and has been found to be a reliable estimator of clear sky atmospheric TIR emissivity over the range of temperatures and pressures encountered in the study area (Mermier and Seguin, 1976, Idso, 1981, Siqueira and Katul, 2009). The formula was derived from physical measurements. Brutsaert's formula to determine atmospheric TIR emissivity is as follows:

$$\varepsilon_{atm} = 1.24 \left[\frac{e}{T}\right]^{\frac{1}{7}} \qquad (28)$$

In equation 28, e is the vapor pressure [mb] and T is the foliage canopy temperature [K].

Another model, developed by Idso, uses water vapor pressure and surface temperature as parameters to characterize emissivity (Idso, 1980). Idso's formulation applies specifically to the 8-µm to 14-µm range of the TIR spectrum (formulas for other spectral ranges were also developed). The model accounts for all absorbers over the relevant spectral range. The formula was derived from physical measurements. Idso's formula, using the notation as in equation 28, is as follows:

$$\varepsilon_{atm} = 0.24 + 2.98 \times 10^{-8} e^2 \exp\left[\frac{3000}{T}\right] \quad (29)$$

However, existing instrumentation at the meteorological tower in Watershed 1 recorded vapor pressure on a percent volume moist air basis, e_{pv}. To arrive at e in millibars, the following form of the Ideal Gas Law was used:

$$e = \frac{100 R_v T}{\alpha} \quad (30)$$

In equation 30, R_v [J kg^{-1} K^{-1}] is the gas constant for 1 kg of water vapor and equals 461.51. T [K] is the dry bulb air temperature at 37 m AGL on the meteorological tower, and α is the specific volume of water vapor [m^3 kg^{-1}]. T is a measured quantity and α is derived from a unit conversion of e_{pv}:

$$\alpha = \frac{(e_{pv}\ mol\ H_2O)\left[\frac{.018\ kg\ H_2O}{1\ mol\ H_2O}\right]}{(1\ mol\ air)\left[\frac{R_u T}{P_{amb}\left(\frac{1\ atm}{101.3\ kPa}\right)}\right]\left[\frac{1\ m^3 air}{10^3 L\ air}\right]} \quad (31)$$

In equation 31, R_u is .082 [L atm mol^{-1} K^{-1}] and P_{amb} [kPa] is air pressure at 37 m AGL on the meteorological tower.

Table 1: A summary of parameters used in equations 22 and 27 and the source of the data for each parameter.

Parameter	Description	Source of Data
T_{cam}	Temperature Recorded by Camera	FLIR SC350 TIR Camera
$\varepsilon_{fol}, \rho_{fol}$	Foliage Emissivity, Reflectivity	Accepted Values from Literature
T_{atm}	Air Temperature at 37 m Above Ground Level	Measured *in situ*
$\varepsilon_{atm}, \tau_{atm}$	Atmospheric Emissivity, Transmissivity	Derived from Brutsaert's and Idso's Formulations
M_{sky}	Sky Radiant Exitance	Measured *in situ*
T_{win}	Temperature of Germanium Window	Measured *in situ*
$\varepsilon_{win}, \tau_{win}$	Window Emissivity, Transmissivity	Product Literature
M_{pyr}	Upwelling Radiant Exitance Recorded by Pyrgeometer	Measured *in situ*
T	Air Temperature at 37 m Above Ground Level	Measured *in situ*
e	Vapor Pressure	Ideal Gas Law (Based on *in situ* Measurements)
α	Specific Volume of Water Vapor	Derived from *in situ* Measurements
P_{amb}	Air Pressure at 37 m Above Ground Level	Measured *in situ*

3.3.1.6 CAMERA AND AIR TEMPERATURE COMPARISON SCHEME

To test concept two, that on clear nights foliage canopy temperature can be a proxy for the temperature of air immediately adjacent to the canopy, the corrected, calibrated, and spatially coincident camera derived foliage temperature was compared to dry bulb temperature data recorded *in situ* at 29 m AGL on the tower.

3.3.2 GEOPROCESSING

Thermal imagery used in the Bright Air study was georeferenced and orthorectified. Georeferencing is the process of ‘aligning geographic data to a known coordinate system so it can be viewed, queried, and analyzed with other geographic data’ (ESRI, 2015). Orthorectification is ‘the process of correcting the geometry of an image so that it appears as though each pixel were acquired from directly overhead’ (ESRI, 2015).

The methodology of this part of the study is to:

- Research and identify methods to georeference and orthorectify digital imagery
- Select a method to use for this study
- Create a tool to process the thermal imagery
- Evaluate the tool’s output

3.3.2.1 SET UP AND DATA

The thermal imagery was acquired by the same FLIR SC305 camera used in the camera calibration and proof of concept. The details regarding this sensor are summarized in section 3.2. The dataset to be processed consists of a multi-day series of 15-minute interval comma separated value (csv) files each arranged in an array of rows and columns of the same dimensions as the camera output image. Each pixel of the thermal image corresponds to a temperature, in degrees C, in the corresponding location in the csv. The temperature values in each file were filtered and corrected according to the methods specified in 3.3.1.

3.3.2.2 REVIEW OF DIGITAL IMAGE GEOPROCESSING APPROACHES

Makarovic (1973) is cited as introducing and developing digital monoplotting, ‘a photogrammetric system where single oblique and unrectified photographs or aerial (nadir) images are related to the digital elevation models (DEM) of the corresponding real world’ (Bozzini *et al.*, 2012). Various researchers have used this general approach to geoprocess digital imagery (e.g. Fluehler *et al., 2005, Steiner 2011*, Bozzini *et al.*, 2012).

Aschenwald *et al.* (2001) introduced the JUKE method. This method projects the DEM onto the plane of digital image. This method requires exact knowledge of the ground location of the camera and the use of ground control points (GCP), ‘various locations on a paper or digital map that have known coordinates and are used to transform another dataset—spatially coincident but in a different coordinate system—into the coordinate system of the control points’ (ESRI, 2015). These inputs, among others, are introduced into the algorithm and the geoprocessing is carried out.

In Corripio (2004), a digital image geoprocessing method was described that has been used by others (e.g. Kerr *et al.,* 2013, Salvatori *et al.,* 2011). To summarize the process, the relevant portion of a DEM that covers an area of interest is obtained. To further constrict the DEM area a viewshed, ‘the locations visible from one or more specified points or lines’ (ESRI, 2015), is created using ArcInfo based on several parameters of the camera capturing the imagery. To orthorectify the images the DEM is rotated so that the perspective of its view matches that of the camera. The DEM is then resampled to match the spatial resolution of the camera. A function that relates the location of cells in the DEM to cells in the imagery is developed.

Exelis produces software called ENVI (Environment for Visualizing Images) for geospatial analysis. ENVI is run on IDL (Interactive Data Language). Many routines exist for the user to customize with his own data. One such routine is "ENVI_REGISTER_DOIT". It allows a user to orthorectify and georeference digital images. User input to this routine includes images to be orthorectified, a DEM, and GCP to register the image to the map. The user has options for specifying input/output projections, methods of image warping to use, and the size and type of the output raster. Using this routine within the ENVI-IDL interface, multiple files can be batch processed.

3.3.2.3 GEOPROCESSING WORKFLOW

As shown in Figure 12, the ENVI software from Exelis was selected for use in this study. Other processing related to the Bright Air study was carried out in ArcGIS. Customized tools created using the ENVI IDL interface were very well suited to process file types that are readily usable in both of these software environments. For instance, converting from text based data files to the ERDAS Imagine .img file format is a supported process. ENVI software is proprietary, but is available to university researchers. A customizable routine called "ENVI_REGISTER_DOIT" exists for the type of geoprocessing required for this study. For reasons of access, compatibility, and customizability ENVI was selected as the geoprocessing tool for this study.

Images are manually exported in csv format from ExamineIR, proprietary software that accompanied the FLIR SC305 camera. As shown in Figure 12 and using applied theory described in section 3.3.1, the image data are imported into Matlab, filtered and corrected by a custom designed tool, and exported in csv format. This corrected image data are processed by a tool designed in IDL to convert csv files to raster files in a widely compatible ERDAS Imagine .img format.

Before proceeding with geoprocessing, several parameters must be determined for use in the "ENVI_REGISTER_DOIT" routine. The creation of the points file (keyword PTS in the routine) is nothing but a set of GCP. A thermal image and a digital map that is spatially referenced, a DEM in this case, are reviewed for prominent features identifiable in both files. The points file consists of longitude and latitude points from the DEM and their corresponding pixel row and column number from camera space. The user must also specify the spatial reference system and various other parameters. With this information the routine geoprocesses the files and makes them ready for further analysis. The output of this process is shown in Figure 13.

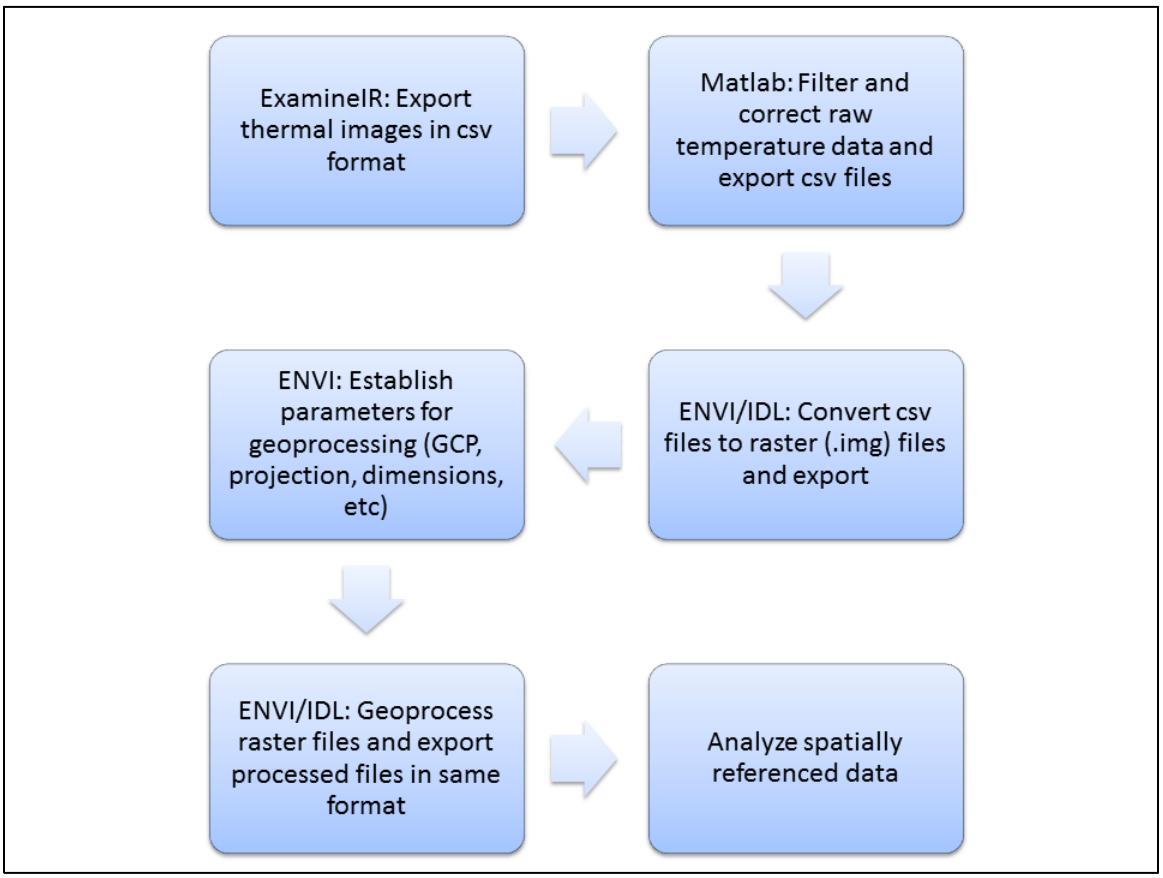

Figure 12: The data flow for processing thermal imagery begins with extracting imagery from ExamineIR in csv format. The image data are imported into Matlab, filtered and corrected by a custom designed tool, and exported in csv format. This corrected image data are processed by a tool designed in IDL to convert csv files to raster files in a widely compatible ERDAS Imagine .img format. Before proceeding with geoprocessing, several parameters must be determined for use in the ENVI_REGISTER_DOIT routine.

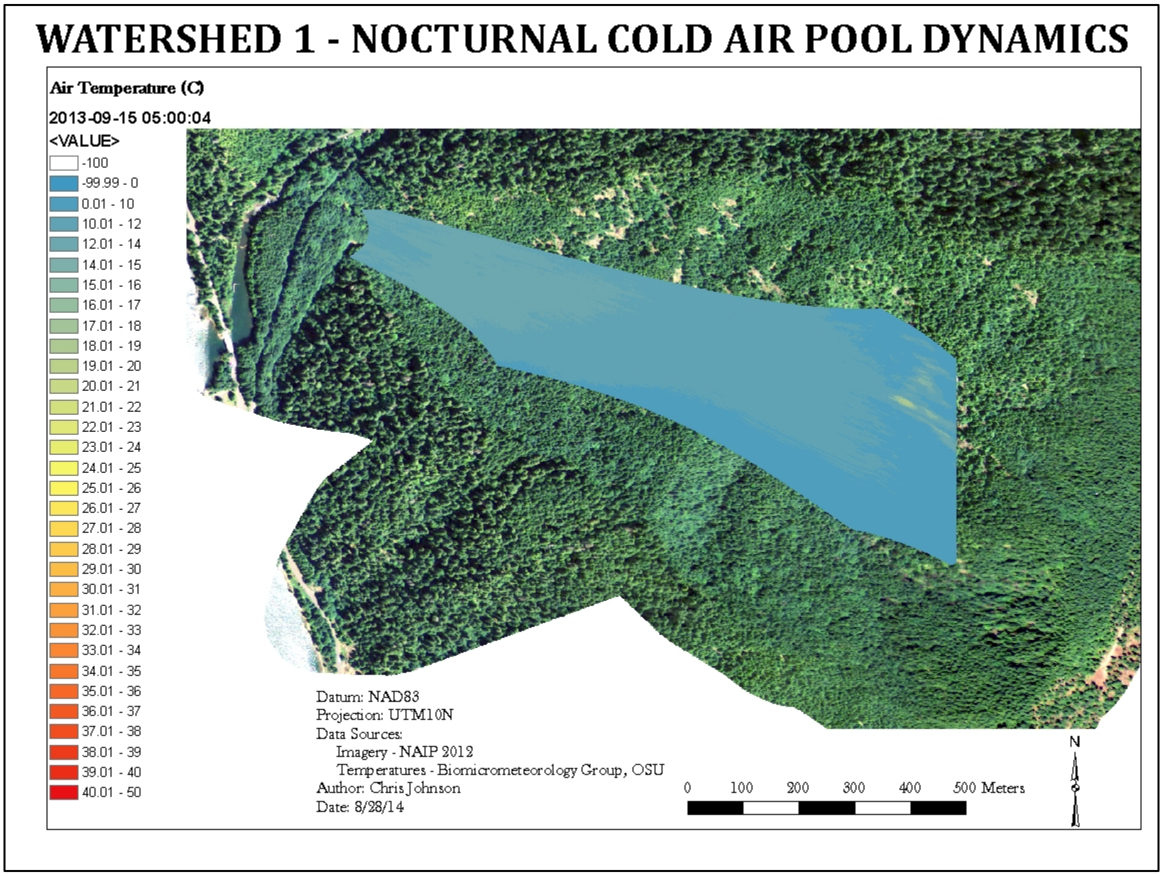

Figure 13: The map displays a geoprocessed thermal image from September 15, 2013 at 05:00. In degrees Celsius the minimum and maximum temperatures in the image are 6.97 and 18.51.

3.3.3 NOCTURNAL BOUNDARY LAYER DYNAMICS OF MOUNTAIN VALLEYS

The geoprocessed thermal imagery, when combined with various data recorded *in situ*, yields potential temperature profiles. Maps derived from the imagery show nocturnal cold air pooling and drainage. Two investigations of the data were undertaken:

1) Vertical profiles of potential temperature in the study area were created for times when inversions exist in Watershed 1 and classified according to flow regimes.

2) Cold air pool formation and drainage evolution were characterized for several clear nights.

3.3.3.1 DATA AND WORKFLOW – POTENTIAL TEMPERATURE PROFILES

The data consist of 15 minute interval spatially referenced temperature information for Watershed 1 and elevation information for each pixel in the image. Visual inspection of the data revealed times when inversions existed in the watershed. An attempt to characterize conditions under which these inversions occur is made.

Walley (2013) sought to evaluate valley processes based on flow regimes categorized by insolation, wind speed, wind direction, and cloud presence in Lookout Creek Valley in the HJ Andrews Experimental Forest. Lookout Creek Valley is the larger basin into which Watershed 1 drains (Figure 1). For consistency similar categories were used in this study. A southwesterly wind is defined as a wind originating from between 190° and 320°. In Watershed 1, a southwesterly wind is indicative of up-valley flow. A north-northeasterly wind is defined as a wind originating from between 350° and 155°. In Watershed 1, a north-northeasterly wind is indicative of down-valley flow. Strong winds are defined as mean winds with a magnitude greater than 0.4 m/s. Weak winds are defined as mean winds with a magnitude less than 0.4 m/s. Only clear or mostly clear nighttime conditions were reviewed in this study. Wind speed at canopy height in Watershed 1 was measured by a sonic anemometer as described in 3.2.

Using relationships described in 2.3.1 and the flow regime and wind strength classifications just presented, a geoprocessing workflow, Figure 14, was developed to output plots of potential temperatures at 10 meter vertical elevation intervals. The plots show averages of 15-minute potential temperature data binned in 10 meter vertical intervals. The plots are displayed per flow regime and by wind strength category. A 95% confidence interval for the potential temperatures was calculated.

The confidence interval was calculated according to the following relationships (Ramsey, 2002):

$$95\%\ Confidence\ Interval = \mu \pm 1.96(SE) \tag{32}$$

In equation 32, μ is the average of potential temperatures at 10 meter vertical elevation intervals and SE is the standard error. Standard error is calculated according to the following relationship:

$$SE = \frac{s}{\sqrt{n}} \tag{33}$$

In equation 33, s is the standard deviation and n is the sample size.

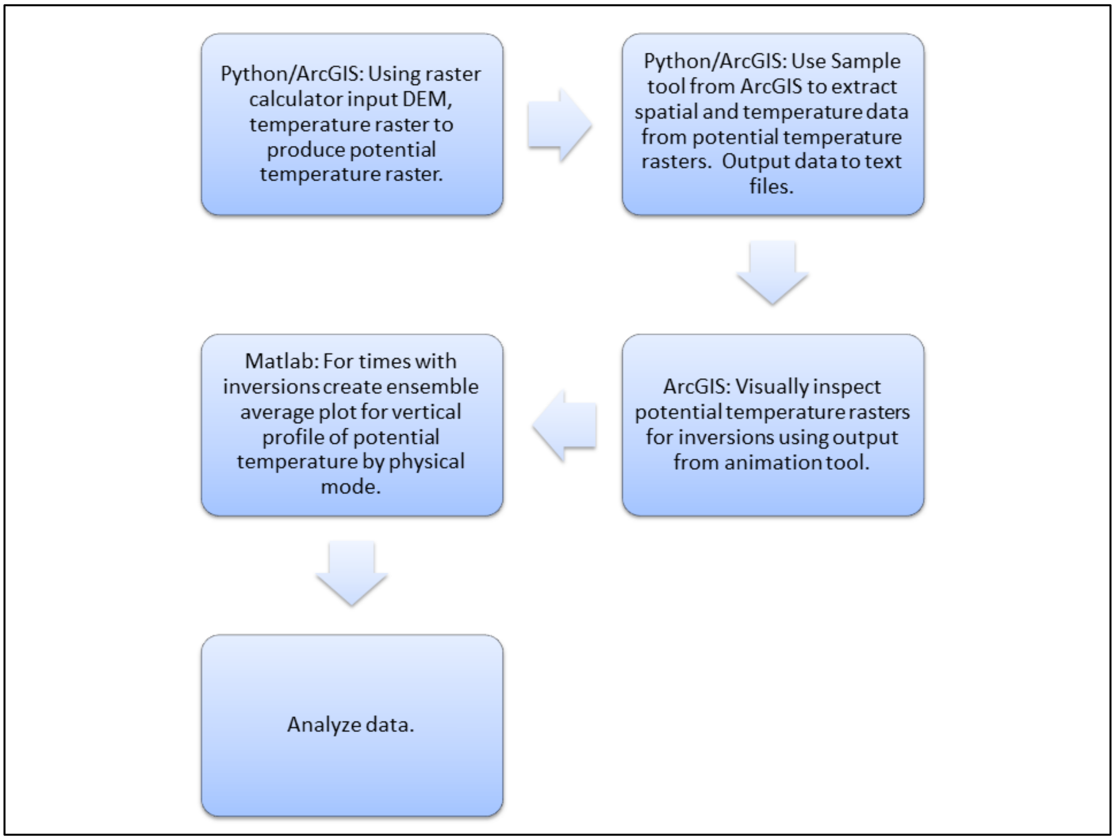

Figure 14: The geoprocessing workflow was developed to output plots of potential temperatures at 10 meter vertical elevation intervals. First spatially referenced temperature data were used to compute spatially referenced potential temperature data using Python/ArcGIS. Then an existing tool in ArcGIS was used to extract spatial information and potential temperature data from the raster. This information was written to a text file. Also, to quickly inspect the potential temperature rasters, the time series of data was animated for easy visual review. After noting times of interest, Matlab was used to input the text file based data, bin and average the potential temperatures, create confidence intervals, and output plots based on the flow regime in the watershed.

The standard deviation was calculated according to the following relationship:

$$s = \left(\frac{1}{n-1}\sum_{i=1}^{n}(x_i - \bar{x})^2\right)^{\frac{1}{2}} \quad (34)$$

In equation 34, x_i is a given potential temperature from the dataset and $\bar{x}$ is the average potential temperature for the 10 meter vertical elevation intervals.

3.3.3.2 DATA AND WORKFLOW – COLD AIR POOLS AND DRAINAGE

In an unpublished analysis conducted in 2012, measurements from a dense sub-canopy network of sonic anemometers in Watershed 1 indicated that flows in the watershed may not be solely gravity driven. However, sub-canopy flow is not what has been recorded in this study. Instead, the dataset produced by the methods described in this work provides a time series of spatially referenced temperature information of air at the canopy surface. Using this information it is possible to characterize the movements of the above canopy flow and to speculate as to how the flow is connected to the larger valley system circulation. Determining whether or not the above canopy flow is coupled to the sub-canopy flow requires measurement of wind speed and direction from multiple point sensors below the canopy (e.g. Thomas, 2011, Thomas and Foken, 2007, Vickers *et al.*, 2012, Vickers *et al.*, 2013). This type of data was unavailable during this study period. However, at 4 m AGL wind speed, wind direction, and statistical information associated with those metrics were recorded at the flux and meteorological tower in Watershed 1. Vickers *et al.* (2012) found that sub-canopy flow was more likely to decouple from above canopy flow in weak wind conditions (less than 4 m s^{-1}at that study site) than in strong wind conditions. The 4-meter wind data and statistics will also be useful in determining whether the base of the flux and meteorological tower was immersed in a cold-air pool or measuring down-valley drainage. Mahrt (2010) found that nocturnal flow at a given point in a valley will be downslope until the cold-air pool at its lower elevations rises to that point. He also found that the interaction between the flow and the rising cold-air pool is characterized by large unpredictable changes in wind direction, and that there is less variability in the wind direction during times of down-valley flow.

Limiting the scope of the investigation to nocturnal flows, the above and sub-canopy flows were examined for further evidence of nocturnal flows that are not solely gravity driven. 15 minute interval temperature map data described in section 3.3.2 formed the basis for analysis. The data were acquired using the wider angle lens for the TIR camera described in section 3.2 and provided some thermal information about the portion of Lookout Creek Valley immediately adjacent to Watershed 1. The data were animated and visually reviewed. This initial step indicated a physical basis to divide nocturnal flow in Watershed 1 into four time intervals that represent distinct stages of typical nocturnal flow in the watershed. With a basis for temporally categorizing the data established, wind speed and direction measurements recorded by a sonic anemometer (R2, Gill Instruments Ltd, Lymington, UK) mounted above the main tree canopy height (h_{canopy} = 29 m AGL) at 37 m AGL and those recorded by a sonic anemometer (81000, Manufacturer R.M. Young, Traverse City, MI, USA) in the sub-canopy at 4 m AGL were examined to further characterize the nocturnal cold-air dynamics observed by the camera. Comparing wind speeds and directions above and below canopy level gave an indication of the extent to which the two flow regimes were coupled. The variation in wind direction can offer an indication about interactions between cold-air pools and down-valley flows. Wind direction variability was characterized by calculating the change in wind direction between 1 minute measurements correcting for north jumps. These values were averaged by stage of nocturnal flow evolution.

The details of the physical characteristics of the four stages of typical nocturnal flow in the watershed are described in section 4.2.2. The general division scheme is the following:

- Stage 1 is the transition from evening to night and lasts one hour after sunset. It is characterized by cooling air in Lookout Creek Valley and Watershed 1. Flow is predominately down-valley during this period.

- Stage 2 lasts until approximately 22:30 local time (dependent on time of sunset) and is characterized by cold air pool formation in Lookout Creek Valley. In Watershed 1 down-valley flow is evident during this period, but up-valley flow is increasing and can even prevail above the canopy.

- Stage 3 lasts until approximately 02:00 local time (dependent on time of sunset) and is characterized by continued cold air pool growth in Lookout Creek Valley. In Watershed 1 up-valley flows are strengthening and occasionally prevail above and below the canopy.

- Stage 4 lasts until one hour after sunrise. Up-valley flows continue to strengthen during this stage. It is characterized by a higher likelihood of decoupled above and sub-canopy flows.

Each stage is an average of two nights of data from clear nights available for study between September 9th and 17th and the night of October 26th 2013. The exact time periods for these stages depend on sunrise and sunset times for the date being investigated. Each stage is an average of two nights that correspond to a composite case. Each composite case exhibits general trends described in the four stages but displays unique features. The details of each composite are described in section 4.2.2. Composite cases are divided as follows:

- Composite case 1 corresponds to the nights of October 26th and September 14th.

- Composite case 2 corresponds to the nights of September 9th and September 10th.

- Composite case 3 corresponds to the nights of September 12th and September 13th.

The full discussion of cold air pooling and drainage in section 4.2.2 includes a review of wind speed, direction, and direction variability by stage and composite. These metrics' averages are based on the one minute interval values from the sonic anemometer dataset described in section 3.2. Each of these one minute values was categorized by composite case, stage, and wind direction. Wind direction was then categorized according to the scheme defined by Walley (2013) discussed in section 3.3.3.1. Because only wind direction measurements that met the classification scheme requirements were analyzed, the number of one minute interval measurements discussed in section 4.2.2 varies by composite and stage. Stage 1 varied between 160 and 180 samples, stages 2 and 3 varied between 150 and 180 samples, and stage 4 varied between 330 and 335 samples.

4 RESULTS AND DISCUSSION

4.1 FILTERING AND CORRECTING TIR MEASUREMENTS

4.1.1 ATMOSPHERIC TIR EMISSIVITY

The terms in the numerators of equations 22 and 27 are in units of K^4. In terms of these units, the total quantity of longwave radiation sensed by each sensor is on the order of 10^9. The contribution to the total quantity of longwave radiation measured by each sensor that is attributable to the atmosphere (the 'atmosphere' term) is on the order of 10^9. Quantities attributable to reflections from the sky and the germanium window are on the order of 10^8. The correction of the greatest magnitude is the atmosphere term. As discussed earlier (also displayed in Table 1), atmospheric emissivity in the spectral range of interest is the only term in equations 22 and 27 sensitive to choice of computational model.

TIR emissivities derived from Brutsaert's and Idso's formulations generally agreed with previous results (Brutsaert, 1975; Idso, 1980). However, the upper limit of the range of emissivities derived here from Idso's formulation (8-µm to 14-µm range) is approximately .18 higher than that reported in Idso's results (Idso, 1980). Atmospheric TIR emissivities derived from Brutsaert's formulation ranged from approximately .79 to .87 over the range of vapor pressures measured at the study site for the data analyzed. The small data spread seen in the left pane of Figure 15 indicates emissivity values from Brutsaert's formulation are relatively insensitive to changes in surface air temperature. Atmospheric TIR emissivities derived from Idso's formulation (8-µm to 14-µm range) ranged from approximately .33 to .74 over the range of vapor pressures measured at the study site for the data analyzed. The large data spread seen in the right pane Figure 15 indicates emissivity values from Idso's formulation are sensitive to changes in surface air temperatures. Figure 16 shows temperature dependencies for each formulation. Only Idso's formulation has a visibly discernable temperature dependency for emissivity values. The figure shows that for a given vapor pressure increasing temperatures result in decreasing emissivities.

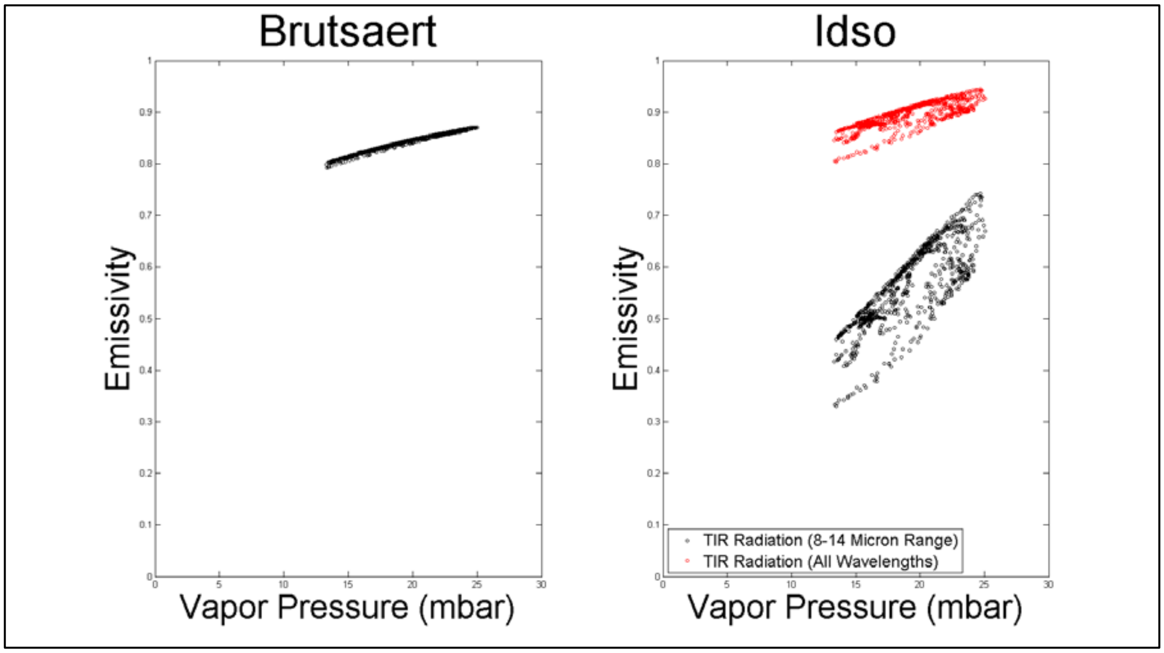

Figure 15: Atmospheric TIR emissivities as derived from Brutsaert's and Idso's formulations. The emissivity derived from Brutsaert's work accounts for a broad range of TIR wavelengths. The formulations developed by Idso are (in black) for the 8-µm to 14-µm range of the TIR spectrum and (in red) the entire TIR spectrum.

Using Brutsaert's formulation for atmospheric TIR emissivity resulted in camera derived temperatures that were tens of degrees different from the temperatures recorded by the thermistors and those derived from the pyrgeometer. The right pane of Figure 16 shows that increasing water vapor pressure results in increasing TIR atmospheric emissivity. As just noted, it also shows that for a given water vapor pressure, increasing temperature results in decreasing values for TIR atmospheric emissivity. The left pane of Figure 16 shows that Brutsaert's formulation does not parse out the differing effects of these two parameters. Noting that prior formulations for estimating atmospheric TIR emissivity show that increasing emissivities correspond to increasing temperatures, Idso wrote:

> *"The relative successes of all prior equations have been due to general correlations between e_0 and T_0…prior equations can in no way be expected to give accurate instantaneous results for the same reason."*

Based on this review of methods of determining atmospheric TIR emissivity, Idso's formulation was selected for use in this study.

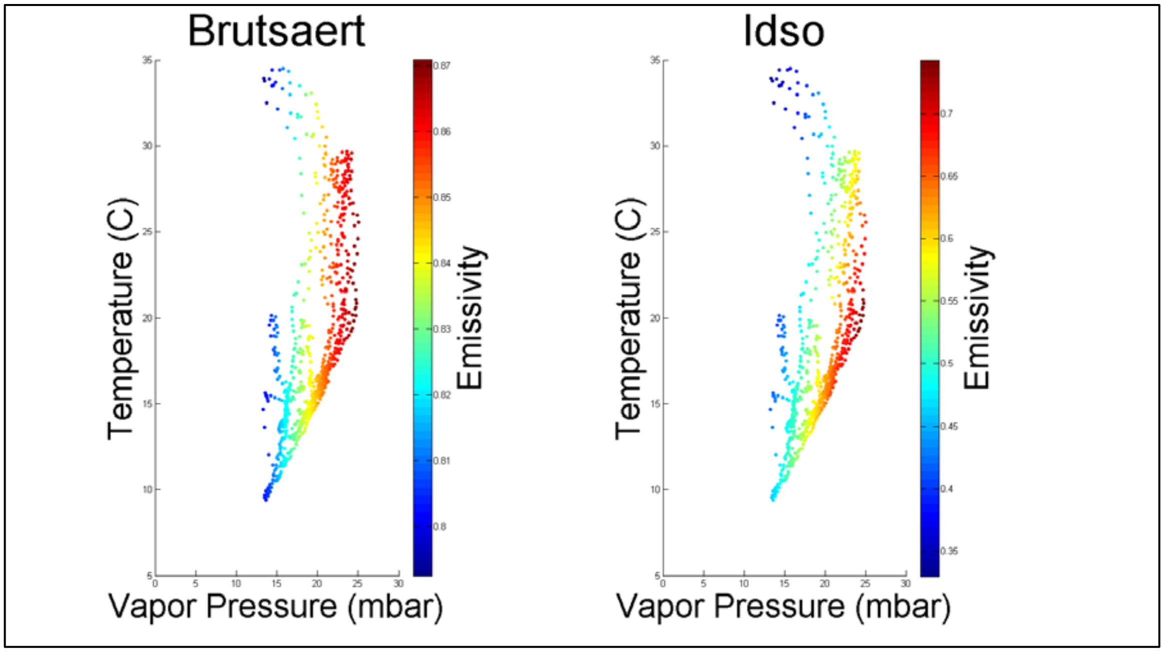

Figure 16: Atmospheric TIR emissivities as derived from Brutsaert's and Idso's formulations. The emissivity derived from Brutsaert's work accounts for a broad range of TIR wavelengths whereas the formulation used from Idso is for the 8-µm to 14-µm range of the TIR spectrum. Only Idso's formulation has a visibly discernable temperature dependency for emissivity values. For a given vapor pressure, increasing temperatures result in decreasing emissivities.

4.1.2 TEMPERATURE COMPARISONS

Temperatures were compared for the nights of September 8, 2013 to September 17, 2013. For the purposes of this comparison, night is defined as whenever downwelling shortwave radiation as measured by a pyranometer mounted on the Watershed 1 meteorological tower is less than 10 W/m^2. Nights were reliably clear until the morning of September 13th. After that date clouds were intermittent. The results were characterized for the overall dataset and broken out into groups corresponding to the cloud conditions. This distinction between clear and intermittently cloudy nights is based on the importance of atmospheric emissivity, as discussed in section 4.1.1, in determining the foliage canopy temperature. For example, a cloud could envelop the camera but not the instrument tower in the watershed. In this case the camera would see the cloud's emissivity but be corrected by the emissivity values derived from tower based data. This would introduce uncertainty into the filtering process. Idso's formulation for emissivity, equation 29, was used to derive the results presented in these comparisons.

4.1.2.1 COMPARISON OF CAMERA AND PYRGEOMETER DERIVED TEMPERATURES

For the full dataset, the maximum and minimum differences between the derived foliage canopy temperatures are 5.9 K and .01 K. A paired t-test was performed (t=12.7, two sided p-value of 2.2×10^{-16} on 443 degrees of freedom). The results indicate with 95% certainty that the camera gives a lower estimate of the foliage canopy temperature than the pyrgeometer. The 95% confidence interval for the difference is between 1.0 K and 1.4 K with an average difference of 1.2 K.

For reliably clear nights, the maximum and minimum differences between the derived foliage canopy temperatures are 5.9 K and .02 K. A paired t-test was performed (t=3.11, two sided p-value of .002, on 222 degrees of freedom). The results indicate with 95% certainty that the camera gives a lower estimate of the foliage canopy temperature than the pyrgeometer. The 95% confidence interval for the difference is between .15 K and .67 K with an average difference of .41 K. These results are presented in Figure 17.

For cloudy nights, the maximum and minimum differences between the derived foliage canopy temperatures are 4.6 K and .01 K. A paired t-test was performed (t=17.3, two sided p-value of 2.2×10^{-16}, on 221 degrees of freedom). The results indicate with 95% certainty that the camera gives a lower estimate of the foliage canopy temperature than the pyrgeometer. The 95% confidence interval for the difference is between 2.3 K and 1.8 K with an average difference of 2.0 K. These results are presented in Figure 18.

4.1.2.2 COMPARISON OF CAMERA DERIVED TEMPERATURE AND CANOPY LEVEL AIR TEMPERATURE

For the full dataset, the maximum and minimum differences between the derived foliage canopy temperatures are 8.1 K and .003 K. A paired t-test was performed (t=3.53, two sided p-value of .0005 on 394 degrees of freedom). The results indicate with 95% certainty that the camera gives a higher estimate of the air temperature than the tower mounted temperature sensor. The 95% confidence interval for the difference is between .18 K and .63 K with an average difference of .40 K.

For reliably clear nights, the maximum and minimum differences between the derived foliage canopy temperatures are 8.1 K and .02 K. A paired t-test was performed ($t=2.54$, two sided p-value of .01, on 172 degrees of freedom). The results indicate with 95% certainty that the camera gives a lower estimate of the foliage canopy temperature than the tower mounted temperature sensor. The 95% confidence interval for the difference is between .12 K and .98 K with an average difference of .55 K. These results are presented in Figure 19.

For cloudy nights, the maximum and minimum differences between the derived foliage canopy temperatures are 4.9 K and .003 K. A paired t-test was performed ($t=13.3$, two sided p-value of 2.2×10^{-16}, on 221 degrees of freedom). The results indicate with 95% certainty that the camera gives a higher estimate of the foliage canopy temperature than the tower mounted temperature sensor. The 95% confidence interval for the difference is between .98 K and 1.3 K with an average difference of 1.1 K. These results are presented in Figure 20.

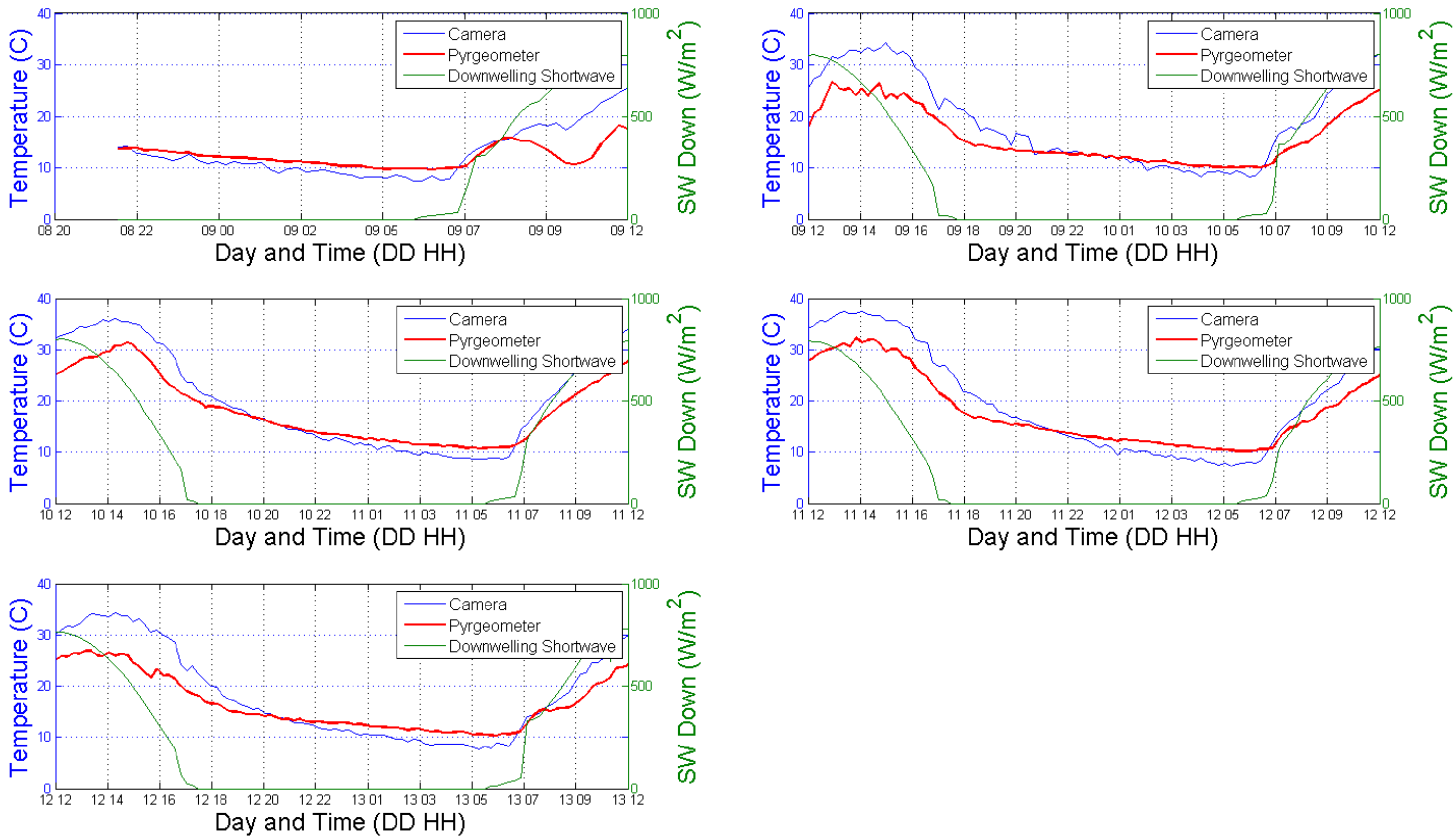

Figure 17: TIR camera and pyrgeometer derived foliage canopy temperatures are compared for reliably clear nights in September 2013. Downwelling shortwave radiation is included as an indicator for nighttime conditions. The maximum and minimum differences between the derived foliage canopy temperatures are 5.9 K and .02 K. A paired t-test was performed (t=-3.11, two sided p-value of .002, on 222 degrees of freedom). The results indicate with 95% certainty that the camera gives a lower estimate of the foliage canopy temperature than the pyrgeometer. The 95% confidence interval for the difference is between .15 K and .67 K with an average difference of .41 K. Camera temperatures corrected by best fitting model from calibration study.

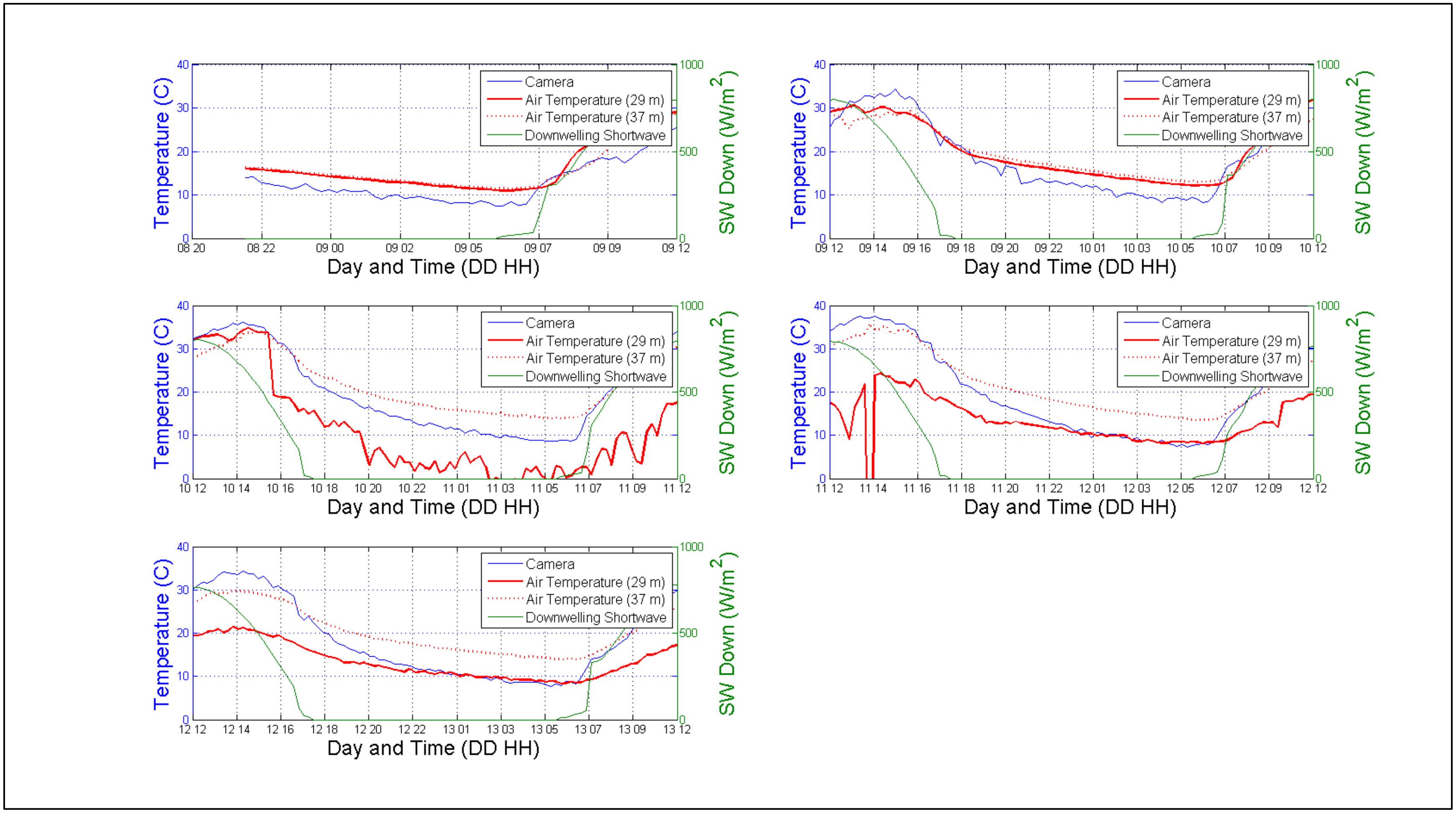

Figure 18: TIR camera and pyrgeometer derived foliage canopy temperatures are compared for intermittently cloudy nights in September 2013. Downwelling shortwave radiation is included as an indicator for nighttime conditions. The maximum and minimum differences between the derived foliage canopy temperatures are 4.6 K and .01 K. Paired t-test was performed (t=-17.3, two sided p-value of $2.2{\times}10^{-16}$, 221 degrees of freedom). The results indicate with 95% certainty that the camera gives a lower estimate of the canopy temperature than the pyrgeometer. The 95% confidence interval is between 2.3 K and 1.8 K with an average difference of 2.0 K. Camera temperatures corrected by best fitting model from calibration study.

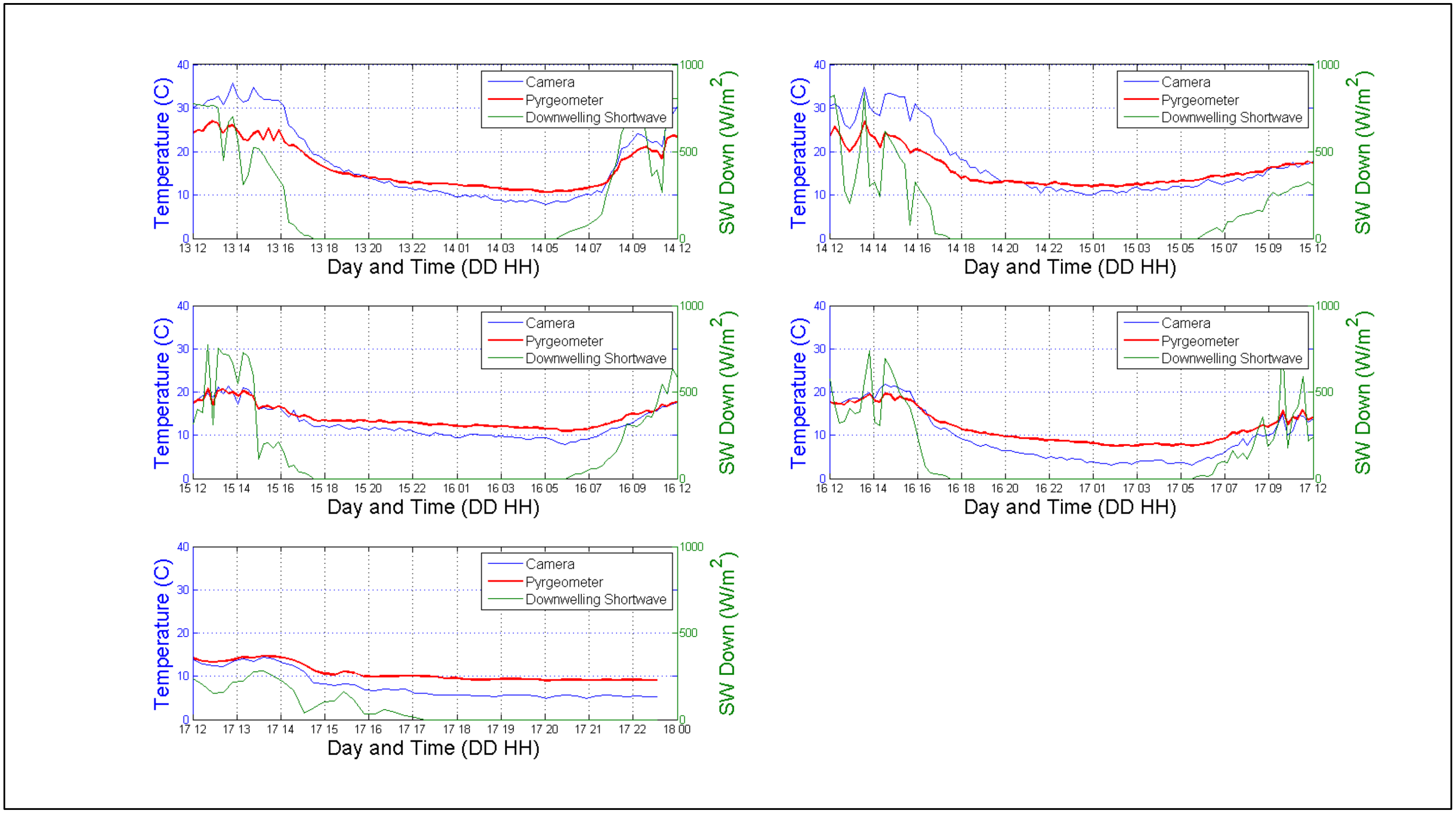

Figure 19: TIR camera derived foliage canopy temperature and measurements for tower mounted air temperature sensors are compared for reliably clear nights in September 2013. Downwelling shortwave radiation is included as an indicator for nighttime conditions. The maximum and minimum differences between the derived foliage canopy temperature and the 29-meter level temperature are 8.1 K and .02 K. A paired t-test was performed (t=-2.54, two sided p-value of .01, on 172 degrees of freedom). The results indicate with 95% certainty that the camera gives a lower estimate of the foliage canopy temperature than the tower mounted temperature sensor. The 95% confidence interval for the difference is between .12 K and .98 K with an average difference of .55 K. Data from night 3 have been excluded from the analysis. Camera temperatures corrected by best fitting model from calibration study.

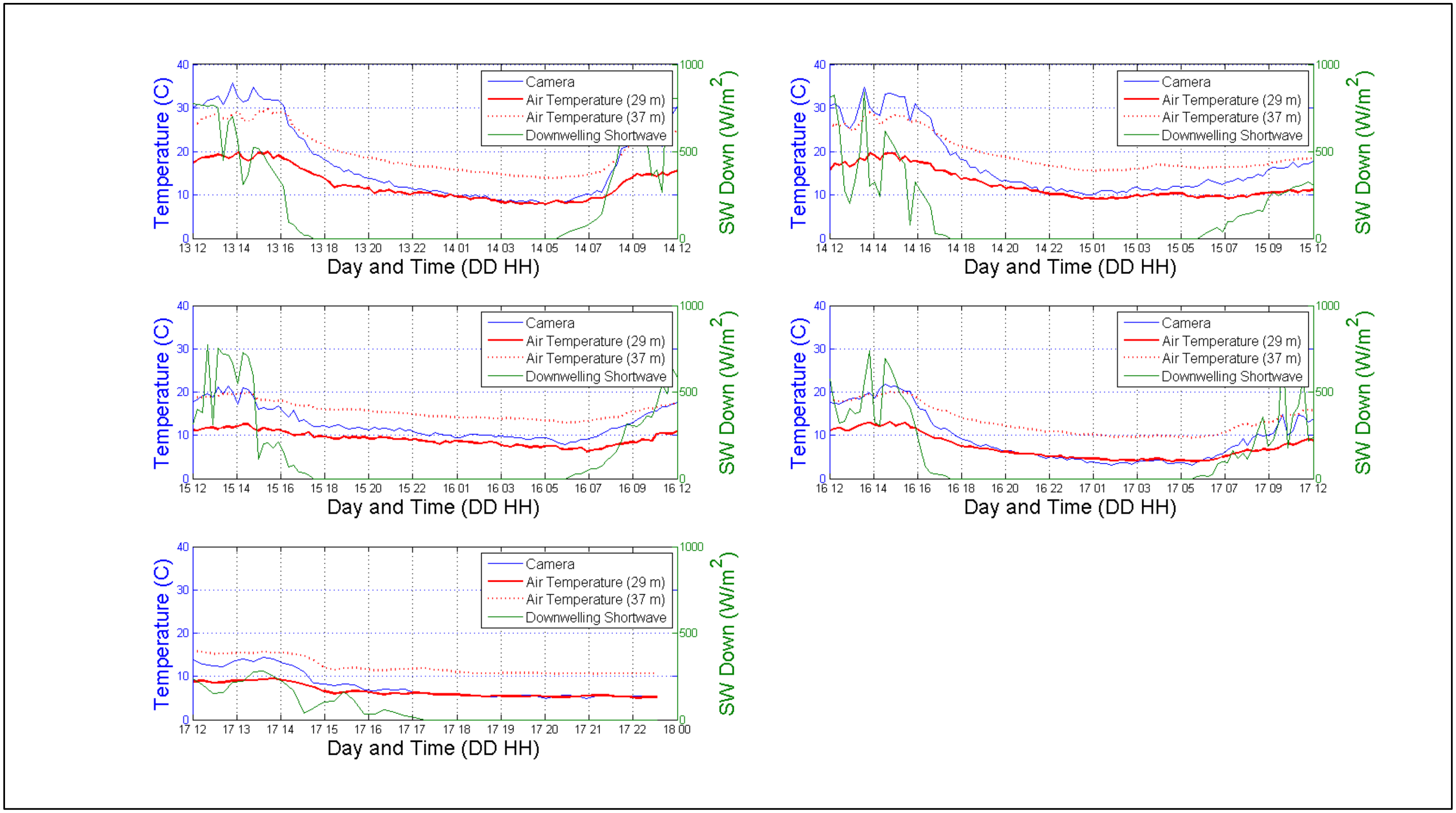

Figure 20: TIR camera derived foliage canopy temperature and measurements for tower mounted air temperature sensors are compared for intermittently cloudy nights in September 2013. Downwelling shortwave radiation is included as an indicator for nighttime conditions. The maximum and minimum differences between the derived foliage canopy temperature and the 29-meter level temperature are 4.9 K and .003 K. A paired t-test was performed (t=13.3, two sided p-value of 2.2×10^{-16}, on 221 degrees of freedom). The results indicate with 95% certainty that the camera gives a higher estimate of the foliage canopy temperature than the tower mounted temperature sensor. The 95% confidence interval for the difference is between .98 K and 1.3 K with an average difference of 1.1 K. Camera temperatures corrected by best fitting model from calibration study.

4.2 NOCTURNAL BOUNDARY LAYER DYNAMICS OF MOUNTAIN VALLEYS

4.2.1 POTENTIAL TEMPERATURE PROFILES BY FLOW REGIME

Figure 21 shows the vertical profile of potential temperature during periods of up-valley (southwesterly) winds. Up to the base of the inversion, the lowest altitude at which a departure from the expected increase in potential temperature with height is found, the atmosphere is statically neutral for strong winds and statically unstable for weak winds. In Figure 22, which shows the vertical profile of potential temperature during periods of down-valley (north-northeasterly) winds, the atmosphere is statically unstable up to the base of the inversion. In every case the atmosphere is statically neutral above the inversion layer.

Lookout Creek Valley is the valley into which Watershed 1 drains (Figure 1). Walley (2013) found the three most common modes of flow regimes in Lookout Creek Valley to have weak synoptic forcing. Weak synoptic forcing was classified as the presence of wind speeds less than 5 m s^{-1} for more than 6 hours of a 12 hour period at elevations between 490 m ASL (47 m AGL) and 540 m ASL (97 m AGL). As outlined in section 3.3.3.1, the physical characteristics of Watershed 1 guide the threshold for weak winds to values less than 0.4 m s^{-1}. Wind speeds in Watershed 1 were measured at 518 ASL (39 m AGL) and analyzed at 1 minute intervals. 10 % of the values used to create the potential temperature profiles were in the strong winds category.

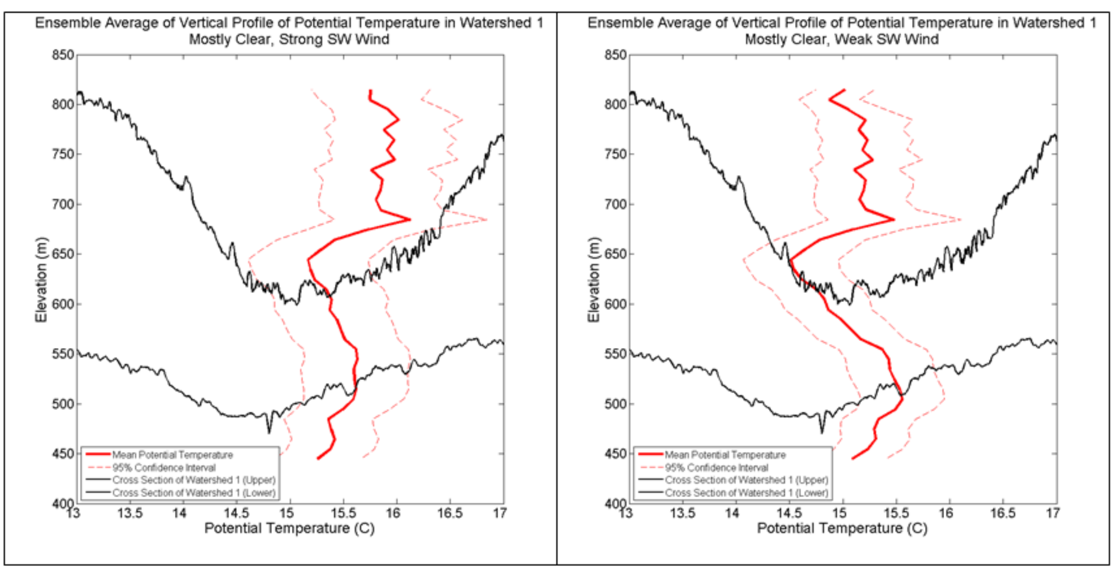

Figure 21: The plots show averages of 15-minute interval potential temperature data binned in 10 meter vertical intervals in Watershed 1 on mostly clear nights with up-valley (southwesterly) winds.

Of those, 75% were strong up-valley (southwesterly) forcing. Walley (2013) found that 20% of the nights studied had strong synoptic forcing. Of those, 60% were strong southwesterly forcing.

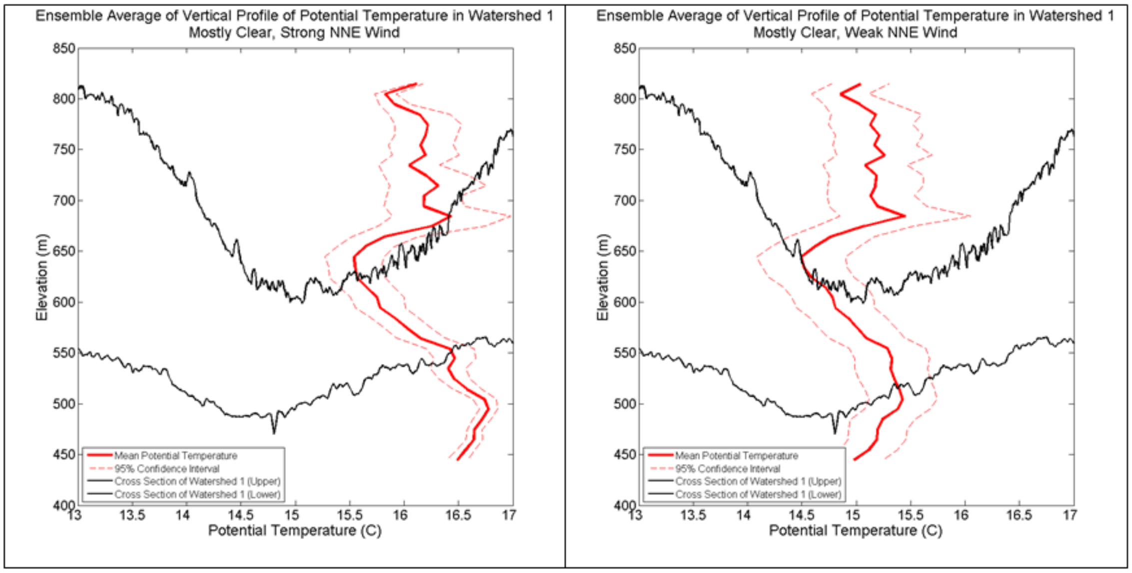

Figure 22: The plots show averages of 15-minute interval potential temperature data binned in 10 meter vertical intervals in Watershed 1 on mostly clear nights with down-valley (north-northeasterly) winds.

On clear nights when inversions are present in Watershed 1 flow regime direction, strength, and frequency correspond well with those found for Lookout Creek Valley in Walley (2013). In fact, for the dataset used to plot the vertical profiles of potential temperature when inversions are present, only 10% of the measurements don't correspond to the north-northeasterly or southwesterly flow regimes described by Walley (2013). This correlation suggests that flows between Watershed 1 and Lookout Creek Valley are subject to the same larger scale synoptic flow and may be physically connected through mass transport. The following section investigates that connection.

4.2.2 COLD AIR POOLS AND DRAINAGE

In section 3.3.3.2 four stages of nocturnal cold air pooling and drainage in Lookout Creek Valley and Watershed 1 were introduced. These stages were determined as a result of a visual inspection of an animation of temperature maps for Watershed 1. Figure 23 displays a summary of the animation. The four stages describe general trends in the watershed, however, a review of ten nights of data revealed three composite cases that reflect the overall trends but display unique features.

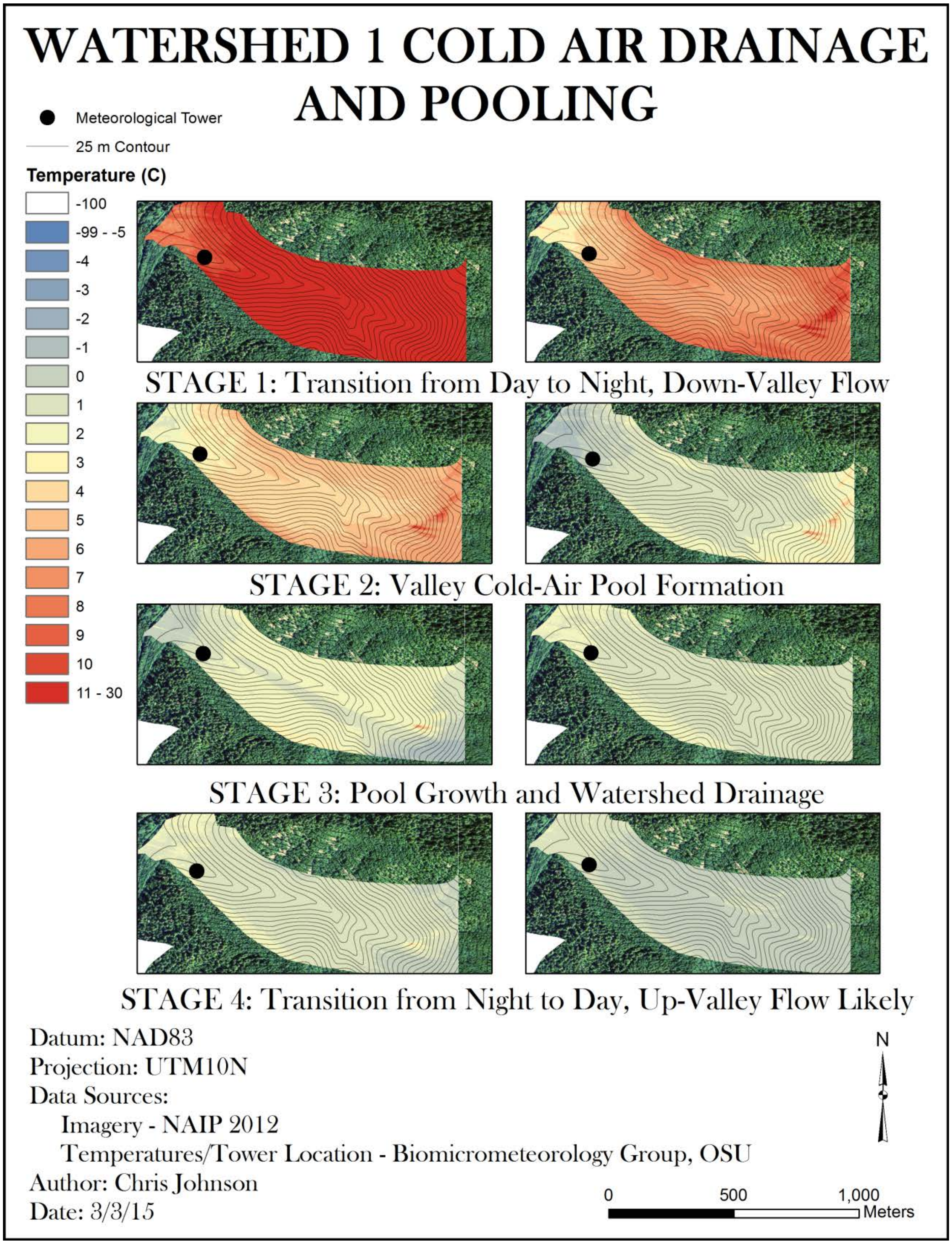

Figure 23: The left panels represent the start of each stage. The right panels show the end of each stage. This data is from the night of October 26, 2013. Stage 1 is the transition from evening to night. It is characterized by cooling air in Lookout Creek Valley and Watershed 1. Flow is predominately down-valley during this period. Stage 2 is characterized by cold air pool formation in Lookout Creek Valley. Down-valley flow is evident during this period, but up-valley flow is increasing and can even predominate above the canopy. Stage 3 is characterized by continued cold air pool growth in Lookout Creek Valley. Up-valley flows are strengthening and occasionally predominate above and below the canopy. Stage 4 lasts until an hour after sunrise. It is characterized by a higher likelihood of decoupled above and sub-canopy flows.

4.2.2.1 COMPOSITE 1

Stage 1 is characterized by cooling air in both Lookout Creek Valley and Watershed 1. Air temperatures for both valleys cool by approximately 5° C during this stage. As shown in Figure 24, the immediate response to the cooling air near the ground and canopy is a prevailing down-valley flow both above and below the foliage canopy. Mean wind speeds above and below canopy level are 0.28 m s^{-1}. If typical shear flow dominated the above canopy wind speed would be greater than the sub-canopy wind speed. This is an indicator that cold air flow depth is from the ground to at least the canopy height of 37 m AGL. Mean changes of wind direction above and below canopy are 32° and 44° respectively. At the tower location the two flows have very similar characteristics and appear to be coupled during this period.

A visual inspection of stage 2 temperature maps seems to show a cold air pool forming in Lookout Creek Valley. The cold air pool appears to deepen and begin to spill into Watershed 1. Air temperatures as shown on the temperature maps for both valleys again cool by approximately 5° C during this period. At this point the cold air pool from Lookout Creek Valley has reached the flux and meteorological tower location (elevation 488 m ASL). Figure 24 reveals an increase in the frequency of up-valley flows compared to down-valley flows relative to stage 1 at both measurement heights. Up-valley flow now dominates above the canopy. Sub-canopy trends are less clear. There are fewer data points for this time period that fit into the up-valley and down-valley flow regimes in Watershed 1 than during any other stage for this composite. The temperature maps show that air continues to cool at higher elevations in the watershed. This implies continued down-valley flows originating at those elevations. Average wind speeds above and below canopy level are both 0.28 m s^{-1}. As in stage 1, this indicates that the cold air flow depth is from the ground to at least the canopy height of 37 m AGL. Mean changes of wind direction above and below canopy are 28° and 50° respectively. Although the frequency of up-valley flow is less than that for down-valley flows in the sub-canopy, the mean wind direction for this stage, 247°, falls in the up-valley category and is very similar to the above canopy mean of 236°. The two flows remain coupled though less strongly than during stage 1.

For the time period of stage 3 the temperature maps reveal cooling of about 1° C in all parts of the watershed. Up-valley flow now dominates above canopy flow at the tower location. The number of up-valley and down-valley flow regime measurements in the sub-canopy has increased relative to stage 2. However, neither regime dominates in the sub-canopy. Mean changes of wind direction above and below canopy are 47° and 24° respectively. While above canopy flow is dominated by up-valley flow at the tower location, the interplay between the deepening Lookout Creek Valley cold air pool and down-valley flow in Watershed 1 is responsible for more variability in sub-canopy flows. Average wind speeds above and below canopy level are both 0.29 m s^{-1}. The trend is for less wind direction variability above the canopy leading into Stage 4. This is not the case for the sub-canopy.

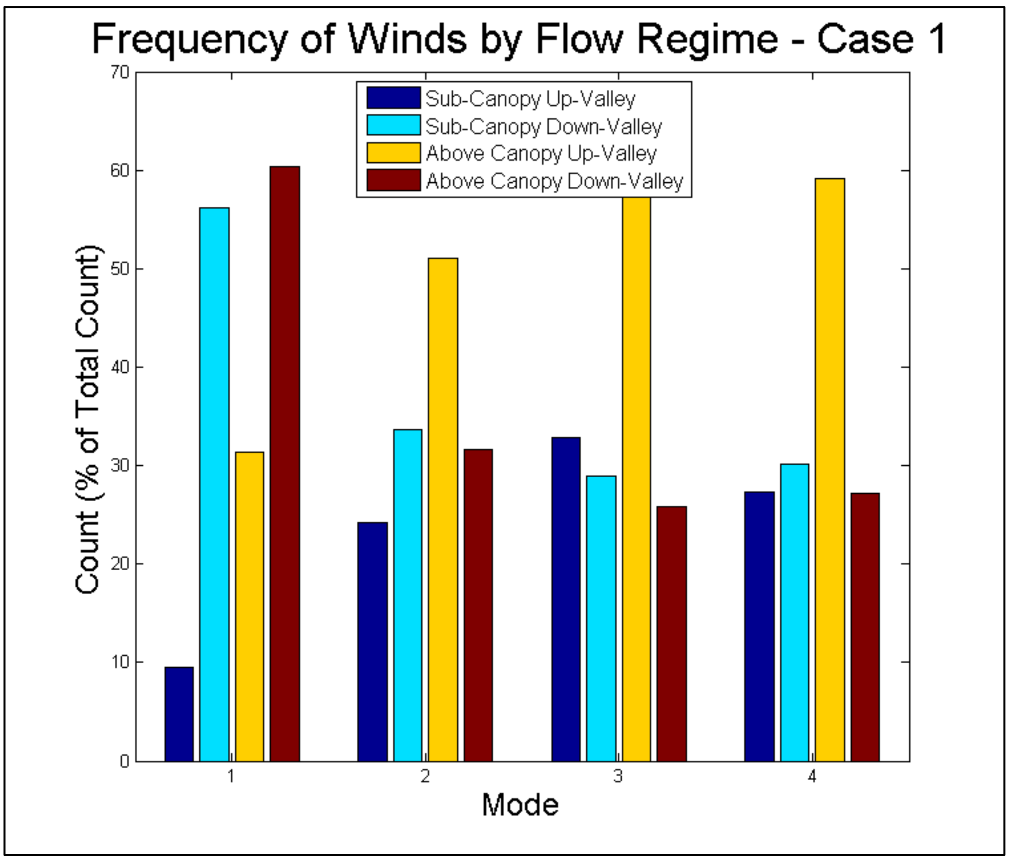

Figure 24: Frequency of flow regimes is displayed by physical stage for one minute interval wind direction data. Up-valley flows are between 190° and 320°. Down-valley flows are between 350° and 150°. For composite 1, the response to the cooling air during stage 1 is a predominating down-valley flow both above and below the foliage canopy. An increase in the frequency of up-valley flows compared to down-valley flows relative to stage 1 at both measurement heights is seen in stage 2. In stage 3 up-valley flow dominates above the canopy, but sub-canopy trends are less clear. In stage 4 up-valley flow continues above the canopy. In the sub-canopy neither flow regime dominates.

During stage 4 colder air appears at upper elevations at the east end of Watershed 1, and temperatures in all parts of the watershed decrease by approximately 1° C. Average wind speeds above and below canopy level are both 0.28 m s^{-1}. At the meteorological tower, up-valley flow dominates above canopy flow. In the sub-canopy neither flow dominates. Variability in wind direction has increased in the sub-canopy and decreased above the canopy. Mean changes of wind direction above and below canopy were 25° and 32° respectively. The total number of one minute interval measurements in this stage that fall into up-valley and down-valley flow regimes increases as the night progresses suggesting that at the tower location there is a significant interplay between the larger valley cold air pool and down-valley flows in the watershed sub-canopy. Above the canopy flow is becoming more consistently up-valley. Flow is less coupled during this period than any other. For one of the nights analyzed in this stage down-valley flow in the sub-canopy predominated. On that night the flows were decoupled.

4.2.2.2 COMPOSITE 2

Two of the warmest nights during the study period were characterized by much more apparent down-valley flows during every stage than for the other composite cases. Temperatures were on the order of 10° to 12° C. Figure 25 displays an ensemble average of flow regimes on those nights. Flow is consistently down-valley during all four stages. During stage 1, winds were strong. During composite 1, winds were weak for every stage. This composite supports the theory that strong winds are less likely to be associated with decoupled above and sub-canopy flows than weak winds.

As in composite 1, stage 1 is characterized by cooling air in both Lookout Creek Valley and Watershed 1. Mean wind speeds above and below canopy level are 0.74 m s^{-1}. There is a prevailing down-valley flow both above and below the foliage canopy. The average above and below canopy wind directions in this stage are 137° and 123° respectively. The similarity of mean wind speeds and their strength are an indicator that flow is strongly coupled both above and below the canopy. Mean changes of wind direction above and below canopy are 32° and 7° respectively. Both values are much lower than those for the first stage of composite 1 and indicate a more organized flow at both levels relative to composite 1.

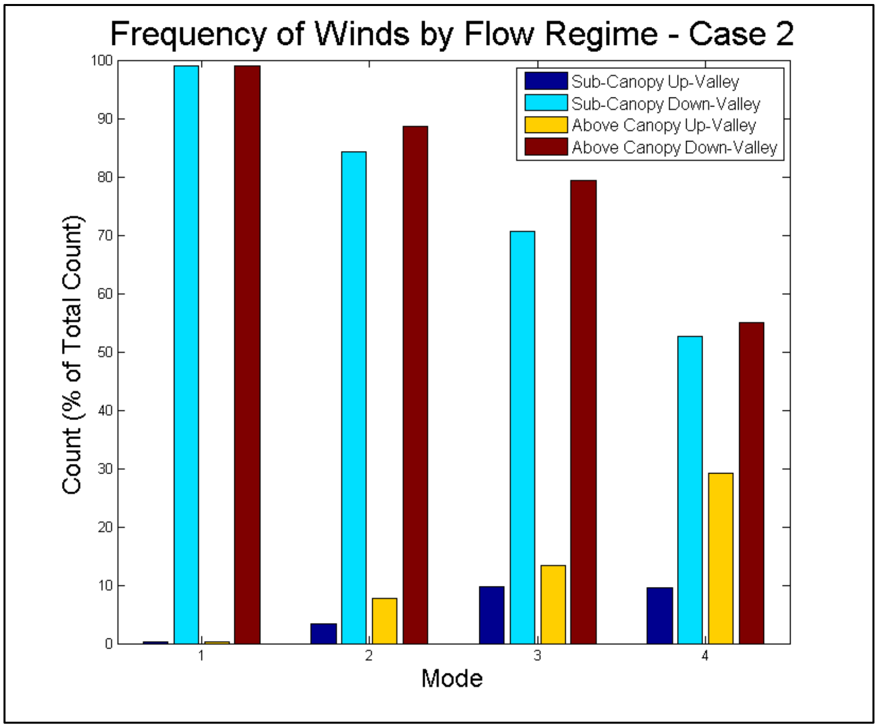

Figure 25: Frequency of flow regimes is displayed by physical stage for one minute interval wind direction data. Up-valley flows are between 190° and 320°. Down-valley flows are between 350° and 150°. For composite 2, down-valley flow dominates throughout the night. However, underlying general trends are still evident. Up-valley flow frequency increases during stages 2 and 3. In stage 4 above canopy up-valley flow accounts for one-third of recorded wind direction measurements.

Stages 2 and 3 continue to display strong coupling in above and below canopy flow. Additionally, the flow continues to be organized. However, trends in stages 2 and 3 reflect the general trends for the watershed. In the sub-canopy mean changes of wind direction are 18° for stage 2 and 27° for stage 3. Above the canopy mean changes of wind direction are 14° for stage 2 and 16° for stage 3. At both levels wind speeds decrease to 0.28 m s^{-1} from 0.34 m s^{-1}. As winds transition from strong to weak variation in wind direction increases at both levels. The increases are greatest in the sub-canopy where the number of wind direction measurements that correspond to up-valley and down-valley flow has decreased from 160 to 130 to 120 in stages 1, 2, and 3.

In stage 4 both wind speed and variation in wind direction measurements in the sub-canopy have returned to levels consistent with those in composite 1, 0.24 m s^{-1} and 34° respectively. Above canopy flow continues to be less variable than sub-canopy flow. The number of wind direction measurements that correspond to up-valley and down-valley flow for this period is 35% greater above the canopy than below the canopy. While flow is still coupled for this period, the coupling is the weakest of any stage for this composite. These characteristics agree with the overall trends for the watershed.

4.2.2.3 COMPOSITE 3

In many respects composite 3 appears to be a hybrid of composites 1 and 2. Temperatures in the watershed are on the order of 10° C. As in composite 2 there are strong winds for stage 1 that decrease to composite 1 levels throughout the night. As in composite 2 there is down-valley flow at both heights for stages 1, 2, and 3. However, as in composite 1, up-valley flow above the canopy increases rapidly in stage 3 and comes to dominate above canopy flow in stage 4. In further agreement with composite 1, in stage 4 the flow becomes decoupled at the tower location. Above canopy flow is up-valley. Sub-canopy flow is predominately down-valley. Figure 26 displays composite 3 flow regimes.

Above and below canopy mean speeds for stage 1 are strong, 0.56 m s^{-1} and 0.57 m s^{-1} respectively. Variability in mean direction above and below the canopy is the lowest recorded during the study period, 26° and 7° respectively. The number of wind direction measurements in this stage that correspond to up-valley and down-valley flow is as high as in stage 1 of composite 2. These metrics all indicate organized flow above and below the canopy. With one exception both above and below the canopy metrics for stage 2 of this composite are extremely similar to those for stage 2 in composite 2. The exception is that wind direction variation above the canopy is 12° higher in composite 3.

Mean wind direction above and below the canopy shifts from down-valley to up-valley between stage 2 and stage 4. Both above and below the canopy variability in the mean wind direction peaks in stage 2 or 3 and then rapidly decreases in stage 4 as the mean wind direction becomes up-valley. However, after the change in wind flow regimes, wind direction variability in stage 4 for above the canopy is 8° and in the sub-canopy it is 23°. These variabilities in wind direction

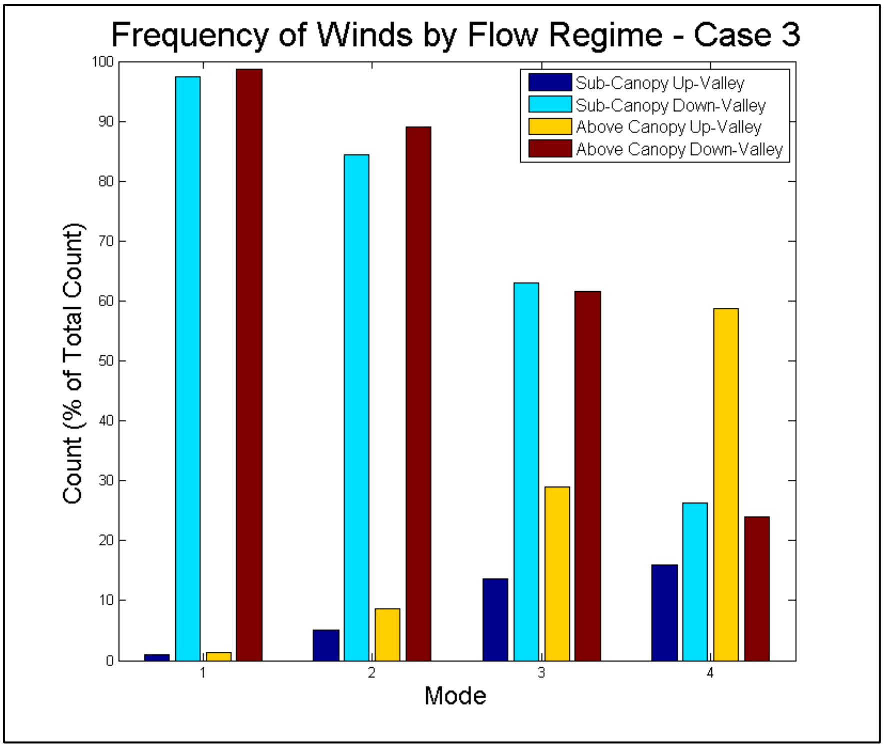

Figure 26: Frequency of flow regimes is displayed by physical stage for one minute interval wind direction data. Up-valley flows are between 190° and 320°. Down-valley flows are between 350° and 150°. For composite 3, the response to the cooling air during stage 1 is a predominating down-valley flow both above and below the foliage canopy. An increase in the frequency of up-valley flows compared to down-valley flows relative to stage 1 at both measurement heights is seen in stages 2 and 3. In stage 4 up-valley flow predominates above the canopy. In the sub-canopy down-valley flow is the most frequent flow regime. In stage 4 the flow becomes decoupled at the tower location.

are some of the lowest recorded in each category. Flow above the canopy is more organized than below the canopy. This organizational differential is also reflected in the fact that the number of wind direction measurements that correspond to up-valley and down-valley flow for this period is 96% greater above the canopy than below the canopy. This is an indication that flow above and below the canopies has become less coupled and possibly decoupled in this stage. Mean wind speeds are both 0.22 m s^{-1}, however, and this metric does not support the characterization of decoupling.

4.2.2.4 REVIEW

Mahrt (2010) observed that nocturnal flow at a given point in a valley will be downslope until the cold air pool at its lower elevations rises to that point. That observation is confirmed here by the transition from stage 1 to stage 2 in composite 1. During stages with strong winds (composite 2: stage 1; composite 3: stage 1) the above and below canopy flows are strongly coupled, and remain so throughout the following stage. In Watershed 1, when above canopy flow becomes predominately up-valley (composite 1: stages 2, 3, and 4; composite 3: stage 4) sub-canopy flow is not typically associated with a dominant wind flow regime. With the possible exception of stage 4 in composite 3, in the sub-canopy, up-valley flow was not observed to be the dominant flow regime for any stage in any composite. However, when reviewing specific nights it was noted that up-valley flow predominated in the sub-canopy during stage 4 on the night of September 14th. Down-valley flow is the only flow regime always associated with strong coupling between the above and sub-canopy flows (composite 1: stage 1; composite 2; stages 1, 2, 3, and 4; composite 3: stages 1, 2, and 3) for the composites reviewed.

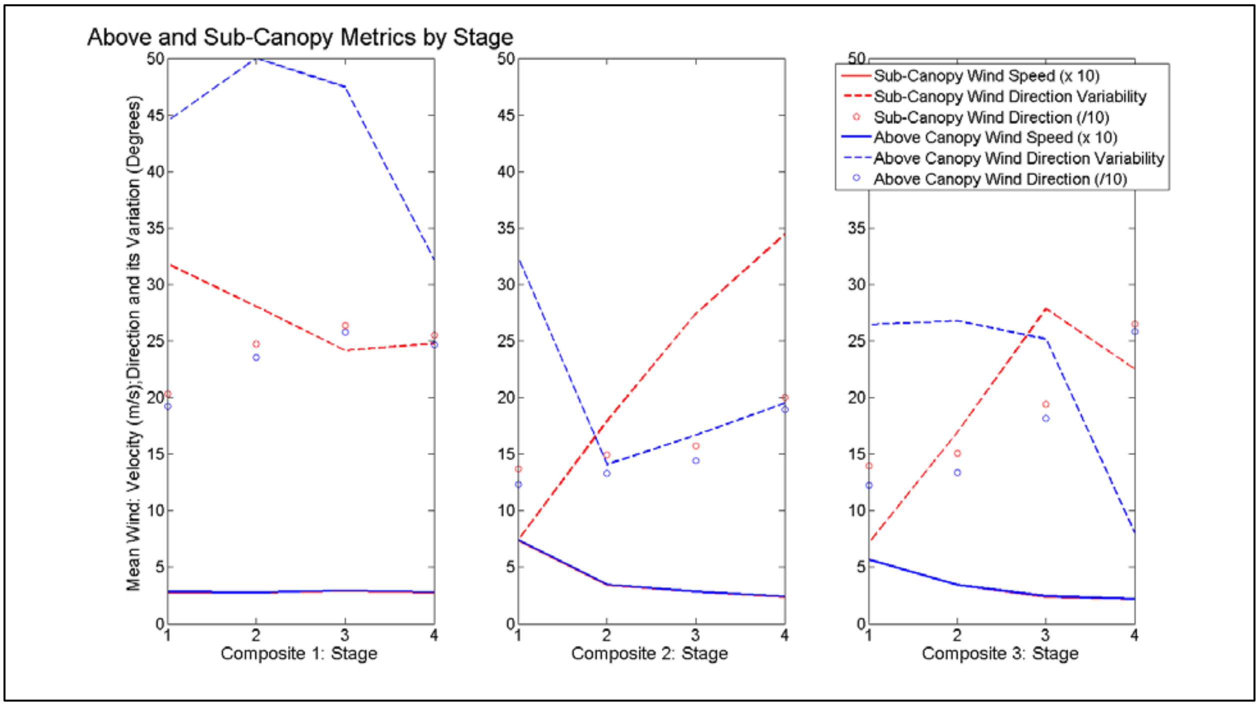

Figure 27: Above and sub-canopy mean wind velocity (multiplied by 10 for display purposes), mean wind direction (divided by 10 for display purposes), and mean wind directional variability are shown. These metrics are displayed by composite and stage.

Less variability in mean wind direction is associated with the dominance of one flow regime over another. For every composite reviewed, this type of dominance occurred during stage 1 both above and below the canopy and is associated with down-valley flows. Figure 27 shows mean wind direction variability by composite and stage. Above the canopy stage 1 variability can be as high as 44° but is more typically on the order of 30°. In the sub-canopy stage 1 variability can be as high as 32° but is more typically on the order of 7°. This measure of variability typically decreased throughout the night above and increased below the canopy. These opposing trends help explain the tendency for weaker coupling in stage 4. In every composite up-valley flow frequency increased in stages 2 and 3 relative to stage 1. During these stages there is interaction between the Lookout Creek Valley cold air pool and down-valley flows from the watershed. This interaction increases the variability in wind direction and is an indicator of when the cold air pool from Lookout Creek Valley reaches the elevation of the flux and meteorological tower.

Watershed 1 is connected to a larger system of valleys. For the nights studied, flows in the watershed interact with flows from these other connected basins. The primary interaction occurs with the cold air pool in Lookout Creek Valley. As the pool deepens during the night, it drains into Watershed 1 creating up-valley flow. This flow is recorded at the location of the flux and meteorological tower. As evidenced by the increased variability of the mean wind direction, during several of the nights examined during this study the tower was located in a zone where the Lookout Creek Valley cold air pool and watershed down-valley flows interacted. This is an indication of the depth of the cold air pool. However, on many of the nights studied the tower's instruments did not record this interaction. This suggests a cold air pool with variable depth. On warmer nights noted in composite 2 there was consistent down-valley flow at both above and sub-canopy heights. This implies that the valley cold air pool was shallower on these nights than on other nights.

The weakening of the coupling between the above canopy flow and sub-canopy flow was in every composite associated with up-valley flow above and stronger down-valley flows below. At the same time the valley cold air pool spilled into the watershed, the watershed flowed into the valley. Above the canopy during these times, the depth of the cold air pool reached elevations higher than that of the tower. This occurred on cold nights and more mild ones. The weakening of the connection between the above and below canopy flows suggests the possibility of a circulation pattern. The mass of air leaving the watershed, if it is not ultimately being blocked before leaving, must be replaced by air entering the watershed. On the nights when this type of decoupling occurs, there must be a net downward flux of momentum up-valley from the meteorological tower.

These results are based on categories for typical flow regimes as determined by Walley (2013). Changing the definition of up-valley to include flows between 190° and 349° (instead of 320°) leads to the conclusion that flows in stages 2, 3, and 4 for composite 1 were up-valley and coupled. For composite 2 stage 4 changes from coupled and down-valley to coupled and up-valley. Stage 3 results for composite 2 show no predominant flow above or below the canopy. For composite 3 only stage 4 results change. In stage 4 flow becomes coupled and up-valley. The axis of Watershed 1 runs along a 290° heading. The mouth of the watershed opens to headings between 240° and 330°. There are very few wind direction data points with values between 190° and 240°. However, there are a significant number between 320° and 340°. These results are sensitive to wind flow regime definitions.

5 SUMMARY AND CONCLUSIONS

5.1 FILTERING AND CORRECTING TIR MEASUREMENTS

As shown in section 4.1.1, the atmosphere term of equations 22 and 27 is the most important correction to make for raw longwave radiation measurements. An accurate determination of TIR atmospheric emissivity is necessary to make this correction. Results presented in section 4.1.1 showed that in this case, Brutsaert's model for estimating TIR atmospheric emissivity is not appropriate for use in making corrections to a TIR camera that measures in the 8-μm to 14-μm range of the TIR spectrum. Applying Idso's model for estimating TIR atmospheric emissivity in the 8-μm to 14-μm range yielded results that ultimately agreed with those derived from two other sensors measuring the same thing as the TIR camera.

While a direct comparison between the temperatures derived from the pyrgeometer and canopy level temperature sensors was not made, one can still compare the relative differences between those sensors and the camera derived temperatures using the results from the paired t-tests presented in section 4.1.2. On nights without any cloud cover the implied difference in air temperature as measured at 29 m AGL (canopy height) and the canopy temperature derived from the downward facing pyrgeometer is 0.1 K. This is well within the uncertainty levels inherent in the sensors. Canopy temperature as derived by the camera on nights without any cloud cover, on average, is within 0.5 K of both of the other sensors. These differences are also within the uncertainty levels inherent in the sensors. The best conditions for using this method to derive foliage canopy temperatures occur on very clear nights.

However, on nights with even intermittent cloud cover there is a 3 K difference between the air temperature as measured at 29 m AGL and the canopy temperature derived from the downward facing pyrgeometer. An explanation for this discrepancy was not found. Canopy temperature as derived by the camera on nights with intermittent cloud cover, on average, is within 2 K of the canopy temperature derived from the downward facing pyrgeometer. If the intermittent clouds were above the mounting height of the pyrgeometer but below the mounting height of the camera it would imply the vapor pressure reading used as the basis to calculate atmospheric emissivity and transmissivity could not reliably be used for corrections on the readings of both sensors. Also it would mean that air temperatures measured at canopy level could not be reliably used for corrections to the readings of both sensors. Also the amount of longwave radiation reflected by the foliage canopy (seen by the pyrgeometer) and top of the cloud (seen by the camera) would be different values. In this case camera readings would be less reliable because the data available to filter and correct the camera readings were not applicable to what is sensed by the camera. The same type of reasoning applies to the difference in temperatures recorded by the camera and the thermistor.

The proof of concept demonstrates that the best results for this method of determining air temperature in a mountain valley are obtained on very clear nights. On those nights the differences between temperatures derived from the TIR camera, pyrgeometer, and the air temperature sensor were all within the devices' margin of error. Furthermore, the study indicates that on clear or intermittently cloudy nights foliage canopy temperatures as measured by a TIR camera can be a proxy for the temperature of air immediately adjacent to the canopy.

5.2 GEOPROCESSING

Georeferencing the images can be made simpler and even more reliable. There were many prominent features to use for GCP in this study. Supplementing these features by placing thermally reflective markers in the area viewed by the camera at points recorded by global positioning system devices would likely decrease the error associated with the geoprocessing. However, in Watershed 1, a valley with slopes up to 70° and trees commonly as tall as 25 m, placing the thermally reflective markers does present its own challenge.

The angle the camera viewed the watershed was not an advantage. The camera was placed at an angle 18° above horizontal looking up into the watershed. Images recorded at a less oblique angle would capture more data. Additionally, any warping and spatial interpolation associated with the geoprocessing would tend to decrease as the angle approaches a view from directly overhead. The possibility of achieving a better viewing angle is study site dependent.

Figure 28: The thermal images acquired deciduous and non-deciduous trees, branches and tree trunks, rocks, and soil. All of the items have unique thermal properties. The emissivity for each item differs in the 7.5 µm to13 µm range. The bright rocks in the top left of the image illustrate this point. The bright tree in the foreground also shows the effects of differing emissivities on the image. Additionally, the tree is not actually in Watershed 1.

As shown in Figure 28, the thermal images captured deciduous and non-deciduous trees, branches and tree trunks, rocks, and soil. All of the items have unique thermal properties. The emissivity for each item differs in the 7.5 µm to13 µm range. No attempt was made to correct for this variability. The implication of this fact is that for a number of pixels, approximately 1% of the pixels in the original images, bad data are being analyzed. There are at least two methods to address this variability. One is to mask out any items that do not form a part of the forest canopy. This would include bare rocks, soil, and any tree tops visible in the imagery that are simply in the camera's field of view but not physically in the watershed. The other approach is to use the concept of raster math. A raster could be created that contains cell values (emissivities) that spatially correspond to each item that needs to be accounted for. This raster could be referenced in subsequent calculations any time the foliage emissivity or reflectivity needed to be used.

5.3 NOCTURNAL BOUNDARY LAYER DYNAMICS OF MOUNTAIN VALLEYS

Nocturnal cold air dynamics in Watershed 1 do not reflect the typical behavior of cold-air pools and drainage as introduced in 2.3.2. This statement supports the analysis and conclusions reached based upon the 2012 data mentioned in 3.3.3.2. Up-valley flow patterns in the watershed observed in this study indicate that nocturnal flows in mountain valleys are not driven solely by colder denser air near the surface that drains down-slope and down-valley. However, the up-valley flow patterns in Watershed 1 are related to growth in the cold air pool that forms in Lookout Creek Valley each night as a direct result of the drainage of this colder denser surface air. However, this study did not isolate and measure any effects of the transport of turbulence at the meteorological tower. It can't be stated conclusively that all variability in wind direction at the tower is due to the growth of the valley cold-air pool. However, the temperature maps show temporal correlation between higher frequency up-valley flows at the flux and meteorological tower and growth in the valley cold-air pool.

Cold-air pools in Lookout Creek Valley and drainage in Watershed 1 have a typical nightly evolution that can be broken down into four stages. Though there is variation in specific aspects of each stage, the overall trends for each stage apply to each case reviewed in this study. In the sub-canopy a denser network of sensors in the watershed may have been able to track the growth in the valley cold air pool and characterize its depth (e.g. Thomas, 2011, Thomas and Foken, 2007, Vickers *et al.*, 2012, Vickers *et al.*, 2013). Spatial patterns of sub-canopy flows would also be more clearly defined. A similar design above the canopy would complement the sub-canopy information and provide a more complete dataset.

The results and conclusions in this section are sensitive to wind flow regime classification. Based on the physical processes observed in the watershed, the classification scheme used in Walley (2013) for Lookout Creek Valley is applicable to Watershed 1. The scheme captures up-valley and down-valley flows, but may not capture all upslope and downslope flows that are occurring in the watershed. However, since these flows were measured close to the base of the valley, downslope flows will have been funneled into the range of down-valley angles. It also excludes down slope flows that move down from the slopes near the entrance to Watershed 1 to the flux and meteorological tower from being considered up-valley.

A study site such as Watershed 1 provides some desirable conditions for this type of study. The watershed connects to a larger system of valleys and basins. Recording between valley interactions is useful in more completely characterizing nocturnal flows in mountain valleys.

The foliage canopy is very dense. This minimizes effects of differing emissivities between branches, trunks, and leaves. Valley slopes are very steep. These slopes are conducive to measureable density driven nocturnal flows. Additionally, as this watershed is located in a forest dedicated to scientific research, it and the nearby Lookout Creek Valley have been extensively studied. These studies provide a good basis for comparison. A more ideal study site would have more uniform ground cover. There are rocky outcrops along the north side of the watershed and near the top of the valley (Figure 28). The varying emissivities add extra computational steps when fully addressed. Additionally, the basaltic outcrops have a different heat capacity than the foliage. This implies a variable time constant for equilibrium between air temperature and the surface. These rocks have a time constant of greater magnitude than the leaves and will take longer to equilibrate with air temperature. Vegetation species variation in the watershed has the same complicating effects as the rocky outcrops. However, TIR emissivity differences and time constant differences between vegetation types will be much less than between large basaltic outcrops and leaves.

6 BIBLIOGRAPHY

A. Ansari, A. and W. Loomis, 1959: Leaf Temperatures. *American Journal of Botany*. **46(10)**, 713-717.

Aschenwald, J., K. Leichter, E. Tasser, U. Tappeiner, 2001: Spatio-temporal landscape analysis in mountainous terrain by means of small format photography: a methodological approach. *IEEE Transactions on Geoscience and Remote Sensing*. **39(4)**, 885-893. doi: 10.1109/36.917917

Baltsavias, E., 1996: Digital ortho-images — a powerful tool for the extraction of spatial- and geo-information. *ISPRS Journal of Photogrammetry and Remote Sensing.* **51(2)**, 63-77. doi:10.1016/0924-2716(95)00014-3

Blum, A., J. Mayer and G. Gozlan, 1982: Infrared thermal sensing of plant canopies as a screening technique for dehydration avoidance in wheat. *Field Crops Research*. **5**, 137—146.

Bonnardot, V., V. Carey, M. Madelin, S. Cautenet, Z. Coetzee, and H. Quénol, 2002: Spatial variability of night temperatures at a fine scale over the stellenbosch wine district, south africa. *Journal International des Sciences de la Vigne et du Vin*. **46(1)**, 1-13.

Bozzini, C., M. Conedera, P. Krebs, 2012: A new monoplotting tool to extract georeferenced vector data and orthorectified raster data from oblique non-metric photographs. *International Journal of Heritage in the Digital Era.* **1(3)**, 499-518. Doi: 10.1260/2047-4970.1.3.499

Brutsaert, W., 1975: On a derivable formula for long-wave radiation from clear skies. *Water Resources Research*. **11(5)**, 742–744. doi: 10.1029/WR011i005p00742

Campbell Scientific, Inc., 2014: *Model 107 Temperature Probe* [Specification Sheet]. Retrieved from https://s.campbellsci.com/documents/us/manuals/107.pdf.

Corripio, J., 2004: Snow surface albedo estimation using terrestrial photography. *International journal of remote sensing*. **25(24)**, 5705-5729. doi:10.1080/01431160410001709002

Courault, D., P. Monestiez, 1999: Spatial interpolation of air temperature according to atmospheric circulation patterns in southeast france. *International Journal of Climatology*. **19(4),** 365-378. doi: 10.1002/(SICI)1097-0088(19990330)19:4<365::AID-JOC369>3.0.CO;2-E

Daly, C., M. Halbleib, J. Smith, W. Gibson, M. Doggett, G. Taylor, J. Curtis, P. Pasteris, 2008: Physiographically sensitive mapping of climatological temperature and precipitation across the conterminous United States. *International Journal Of Climatology*. **28(15)**, 2031-2064. doi: 10.1002/joc.1688

Daly, C., D. Conklin, and M. Unsworth, 2010: Local atmospheric decoupling in complex topography alters climate change impacts. *International Journal of Climatology*. **30(12)**, 1857-1864. Doi: 10.1002/joc.2007

DeGaetano, A., 2007: Spatial interpolation of daily maximum and minimum air temperature based on meteorological model analyses and independent observations. *Journal of Applied Meteorology and Climatology*. 46(11), 1981-1992. doi: http://dx.doi.org/10.1175/2007JAMC1536.1

Doytsher, Y., J. Hall, 1995: FORTRAN programs for coordinate resection using an oblique photograph and high-resolution DTM. *Computers & Geosciences*. **21(7)**, 895-905. doi:10.1016/0098-3004(95)00023-2

ESRI, 2014: *ArcGIS Help 10.1 - Georeferencing tools*. Retrieved from http://resources.arcgis.com/en/help/main/10.1/index.html#/Georeferencing_tools/009t000000mp000000/

ESRI, 2015: *GIS Dictionary*. Redlands: Retrieved from http://support.esri.com/en/knowledgebase/Gisdictionary/browse.

Excelis, 2014: *ENVI_REGISTER_DOIT (ENVI API) | Excelis VIS Docs Center*. Retrieved from http://www.exelisvis.com/docs/ENVI_REGISTER_DOIT.html

FLIR Systems, 2013: *FLIR SC305* [Data Sheet]. Retrieved from https://www.instrumart.com/assets/Flir-SC305-Datasheet.pdf.

Fluehler, M., J., Niederöst, and D., Akca, 2005: Development of an educational software system for the digital monoplotting. ETH, Eidgenössische Technische Hochschule Zürich, Institute of Geodesy and Photogrammetry. doi: 10.3929/ethz-a-005126679

Foken, T. 2008: The energy balance closure problem: An overview. *Ecological Applications*. **18(6)**, 1351-1367. http://dx.doi.org/10.1890/06-0922.1

Frei, C. 2014: Interpolation of temperature in a mountainous region using nonlinear profiles and non-euclidean distances. *International Journal Of Climatology*. **34(5)**, 1585-1605. doi: 10.1002/joc.3786

French, A., T. Schmugge, and W. Kustas, 2000: Discrimination of senescent vegetation using thermal emissivity contrast. *Remote Sensing of Environment*. **74(2)**, 249–254. doi:10.1016/S0034-4257(00)00115-2

Hinkler, J., S. Pederson, M. Rasch, and B. Hansen, 2002: Automatic snow cover monitoring at high temporal and spatial resolution using images taken by a standard digital camera. *International Journal of Remote Sensing*. **23(21)**, 4669–4682. doi: 10.1080/01431160110113881

Hukseflux, 2013: *NR01 Net Radiometer*. Retrieved from http://www.hukseflux.com/product/nr01-net-radiometer.

Idso, S., 1981: A set of equations for full spectrum and 8- to 14-μm and 10.5- to 12.5-μm thermal radiation from cloudless skies. *Water Resources Research*. **17(2)**, 295–304. doi: 10.1029/WR017i002p00295

Jensen, J., 2007: *Remote Sensing of the Environment: An Earth Resource Perspective*. Upper Saddle River, NJ: Pearson Prentice Hall.

Kerr, T., M. Clark, J. Hendrikx, and B. Anderson, B., 2013: Snow distribution in a steep mid-latitude alpine catchment. *Advances in Water Resources*.55, **17–24**. doi:10.1016/j.advwatres.2012.12.010

Kustas, W., and J. Norman 1997: A two-source approach for estimating turbulent fluxes using multiple angle thermal infrared observations, *Water Resources Res*earch, **33(6)**, 1495–1508, doi:10.1029/97WR00704

Lareau, N., E. Crosman, C. Whiteman, J. Horel, S. Hoch, W. Brown, and T. Horst, 2013: The persistent cold-air pool study. *Bulletin of the American Meteorological Society*. **94(1)**, 51-63. doi: http://dx.doi.org/10.1175/BAMS-D-11-00255.1

Leuzinger, S. and C. Körner, 2007: Tree species diversity affects canopy leaf temperatures in a mature temperate forest. *Agricultural and Forest Meteorology*. **146(1-2)**, 29–37. doi: 10.1016/j.agrformet.2007.05.007

Leuzinger, S., R. Vogt, and C. Körner, 2010: Tree surface temperature in an urban environment. *Agricultural and Forest Meteorology*, **150(1)**, 56-62. doi:10.1016/j.agrformet.2009.08.006

Mahrt, L., S. Richardson, N. Seaman, and D. Stauffer, 2010: Non-stationary drainage flows and motions in the cold pool. *Tellus Series A-Dynamic Meteorology and Oceanography*. **62(5)**, 698-705. doi: 10.1111/j.1600-0870.2010.00473.x

Makarovic, B., 1973: Digital monoplotters. *The ITC Journal*. **4**, 583-600.

Marshall, J., A., Plumb, and R. Plumb, 2008: *Atmosphere, Ocean, and Climate Dynamics: An Introductory Text*. Amsterdam; Boston: Elsevier Academic Press.

Matsushima, D. and J. Kondo, 2000: Estimating regional distribution of sensible heat flux over vegetation using satellite infrared temperature with viewing angle correction. *Journal of the Meteorological Society of Japan*, **78(6)**, 753-763.

Mermier, M., and B. Seguin., 1976: Comment on ‘on a derivable formula for long-wave radiation from clear skies’ by w. Brutsaert. *Water Resources Research*. **12(6)**, 1327-1328. doi: 10.1029/WR012i006p01327

Meron, M., M. Sprintsin, J., Tsipris, V., Alchanatis, and Y., Cohen, 2013: Foliage temperature extraction from thermal imagery for crop water stress determination. *Precision Agriculture*. **1(4)**, 467–477. doi: 10.1007/s11119-013-9310-0

Meyers, D., 1994: Spatial interpolation: an overview. *Geoderma*. **62**, 17–28. doi:10.1016/0016-7061(94)90025-6

Moran, M., K. Humes, and P. Pinter, 1997: The scaling characteristics of remotely-sensed variables for sparsely-vegetated heterogeneous landscapes. *Journal of Hydrology*. **190(3-4)**, 337–362. doi:10.1016/S0022-1694(96)03133-2

Noble, P., 2012: *Physicochemical and Environmental Plant Physiology*. Elsevier Science.

Nölke N., P. Beckschäfer, and C. Kleinn, 2015: Thermal canopy photography in forestry - an alternative to optical cover photography. *Journal of Biogeosciences and Forestry*. **8**, 1-5. doi: 10.3832/ifor1129-007

Olioso, A., 1995: Estimating the difference between brightness and surface temperatures for a vegetal canopy. *Agricultural and Forest Meteorology*. ***82***, 237-242. doi:10.1016/0168-1923(94)02163-E

Onset Computer Corporation, 2015: *HOBO Pro Series H8*. Retrieved from http://www.onsetcomp.com/products/data-loggers/h08-031-08.

Pypker, T., M., Unsworth, B., Lamb, E., Allwine, S., Edburg, E., Sulzman, A., Mix, and B., Bond, 2007a: Cold air drainage in a forested valley: investigating the feasibility of monitoring ecosystem metabolism. *Agricultural and Forest Meteorology*. **145(3)**, 149-166. doi:10.1016/j.agrformet.2007.04.016

Pypker, T., M., Unsworth, A., Mix, W., Rugh, T., Ocheltree, K., Alstad, and B., Bond, 2007b: Using nocturnal cold air drainage flow to monitor ecosystem processes in complex terrain. *Ecological Applications*, **17(3)**, 702-714. doi: 10.1890/05-1906

Ramsey, F., and D., Schafer, 2002: *The Statistical Sleuth: A Course in the Methods of Data Analysis*. Australia; Pacific Grove, CA: Duxbury/Thomson Learning.

Salvatori, R., P., Plini, M., Giusto, M., Valt, R., Salzano, and M., Montagnoli, M., 2011: Snow cover monitoring with images from digital camera systems. *Italian Journal of Remote Sensing*. **43**, 137-45. doi: 10.5721/ItJRS201143211

Setra, 2015: *Model 278 Barometric Pressure Sensor*. Retrieved from http://www.setra.com/products/pressure/high-accuracy-pressure-transducer-model-278/.

Siqueira, M., and G., Katul. , 2009: A sensitivity analysis of the nocturnal boundary-layer properties to atmospheric emissivity formulations. *Boundary-Layer Meteorology*. **134(2)**, 223–242. doi:10.1007/s10546-009-9440-0

Soer, G., 1980: Estimation of regional evapotranspiration and soil-moisture conditions using remotely sensed crop surface temperature. *Remote Sensing of Environment*. **9**, 27–45.

Steiner, L., 2011: *Reconstruction of glacier states from geo-referenced historical postcards*. MS Thesis, ETH Zurich.

Sugita, M. T., Hiyama, and T., Ikukawa., 1996: Determination of canopy emissivity: how reliable is it?. *Agricultural and Forest Meteorology*. **81(3-4)**, 229–239. doi:10.1016/0168-1923(95)02313-5

Swanson, F., M., James, Michael, 1975: Geomorphic history of the lower blue river-lookout creek area, western cascades, oregon. *Northwest Science*. **49(1**), 1-11.

The Engineering Toolbox, 2015: Emissivity Coefficients of Some Common Materials. www.engineeringtoolbox.com.

The Engineering Toolbox, 2015a: Convective Heat Transfer Coefficient. Retrieved from http://www.engineeringtoolbox.com/convective-heat-transfer-d_430.html.

Thomas, C., and T., Foken, 2007: Flux contribution of coherent structures and its implications for the exchange of energy and matter in a tall spruce canopy. *Boundary-Layer Meteorology*. **123(2)**, 317-337. doi: 10.1007/s10546-006-9144-7

Thomas, C., 2011: Variability of sub-canopy flow, temperature, and horizontal advection in moderately complex terrain. *Boundary-Layer Meteorology*. **139(1)**, 61-81. doi: 10.1007/s10546-010-9578-9

Tunick, A., 2005: A radiation and energy budget algorithm for forest canopies. *Meteorology and Atmospheric Physics*. **91(1-4)**, 237–246. doi: 10.1007/s00703-005-0145-8

Vickers, D., and C., Thomas, 2013: Some aspects of the turbulence kinetic energy and fluxes above and beneath a tall open pine forest canopy. *Agricultural and Forest Meteorology*. **181**, 143-151. doi:10.1016/j.agrformet.2013.07.014

Vickers, D., J., Irvine, J., Martin, and B., Law, 2012: Nocturnal subcanopy flow regimes and missing carbon dioxide. *Agricultural and Forest Meteorology*. **152**, 101-108. doi:10.1016/j.agrformet.2011.09.004

Wallace, J., and P. Hobbs, 2006: *Atmospheric Science: An Introductory Survey*. Amsterdam; Boston: Elsevier Academic Press.

Walley, Jerilyn. 2013: *Valley Circulation Experiment: A Classification of Wind Flow in the H.J. Andrews Experimental Forest*. MS Thesis, The Evergreen State College.

Whiteman, C., 1990: Observations of thermally developed wind systems in mountainous terrain. Chapter 2 in *Atmospheric Processes Over Complex Terrain*, (W. Blumen, Ed.), Meteorological Monographs, **23(45)**. American Meteorological Society, Boston, Massachusetts, 5-42.

Whiteman, C., J., Hubbe, and W., Shaw, 2000a: Evaluation of an inexpensive temperature datalogger for meteorological applications. *Journal Of Atmospheric And Oceanic Technology*. **17(1)**, 77-81. doi: http://dx.doi.org/10.1175/1520-0426(2000)017<0077:EOAITD>2.0.CO;2

Whiteman, C., 2000b: *Mountain Meteorology: Fundamentals and Applications*. New York: Oxford University Press.

7 APPENDIX

8 STATISTICAL ANALYSIS OF CAMERA CALIBRATION DATA

A set of 360 data points with a temporal resolution of five minutes spread over several runs of heating and cooling the assembly was prepared using Matlab. A first glance, shown in Figure 29, at the data suggested a simple linear relationship between the camera derived object temperature and the object temperature recorded by the probe. To evaluate this initial assessment, a full statistical analysis was carried out using R.

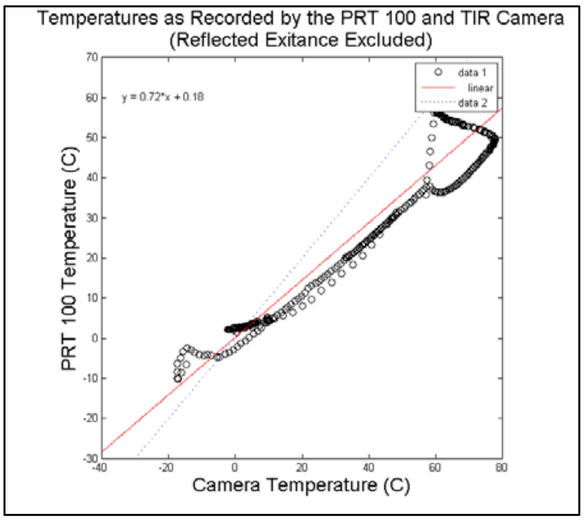

Figure 29: Initial assessment of the data indicated a linear relationship between the two datasets.

8.1.1 EXAMINATION OF THE DATA

Run 1 data begin at 13:04 (all times PST) on March 16th, 2014. The heating element had been turned on at 13:03. The refrigerator was turned on at 14:45. Run 1 data end at 16:29. The refrigerator was turned off at 16:24. Run 2 data begin at 16:34. Run 2 data consist of the assembly equilibrating with its environment. Run 2 data end at 21:59. On March 17th, 2014, at 11:28 the heating element was turned on and the refrigerator was turned off. Run 3 data begin at 11:19 that morning and end at 19:04 that evening. At 19:02 the heater was shut off. Run 4 data begin at 19:09 and ends at 07:29 on March 18th, 2014. At 07:32 the refrigerator was turned on. Run 5 data begin at 07:34 and end at 08:14. Each run is a continuous set of data.

Run 1 shows a linear relationship between the sensors during heating by the element and a non-linear relationship during cooling by refrigeration. Run 2 shows a linear relationship, different from that expressed in Run 1, between the sensors during heating without using the heating element. For the first few data points of Run 3 the refrigerator was on. Subsequently the heater was turned on. During this process the submersible pump in the coolant was on (as it was the entire study). The temperature probe recorded runs of heating and cooling that did not align exactly with the heating/cooling controls.

The resulting relationship for this time period is unclear, but after 12:19 on March 17th the constant heating by the element began to be clearly expressed in the data. The constant heating portions of Runs 1 and 3 appear to agree. From 13:34 to 14:14, while the heating element was on, both the camera and the probe recorded declining temperatures. The element may not have had constant output during this period. The disruption in the linear relationship, as well as other instances of camera temperatures lagging probe temperatures is likely a consequence of the nature of heat conduction. The time it takes for the Delrin to communicate the coolant's temperature to the camera is different from the time it takes for the probe to record that information. A discussion of this thermal inertia can be found later in this section.

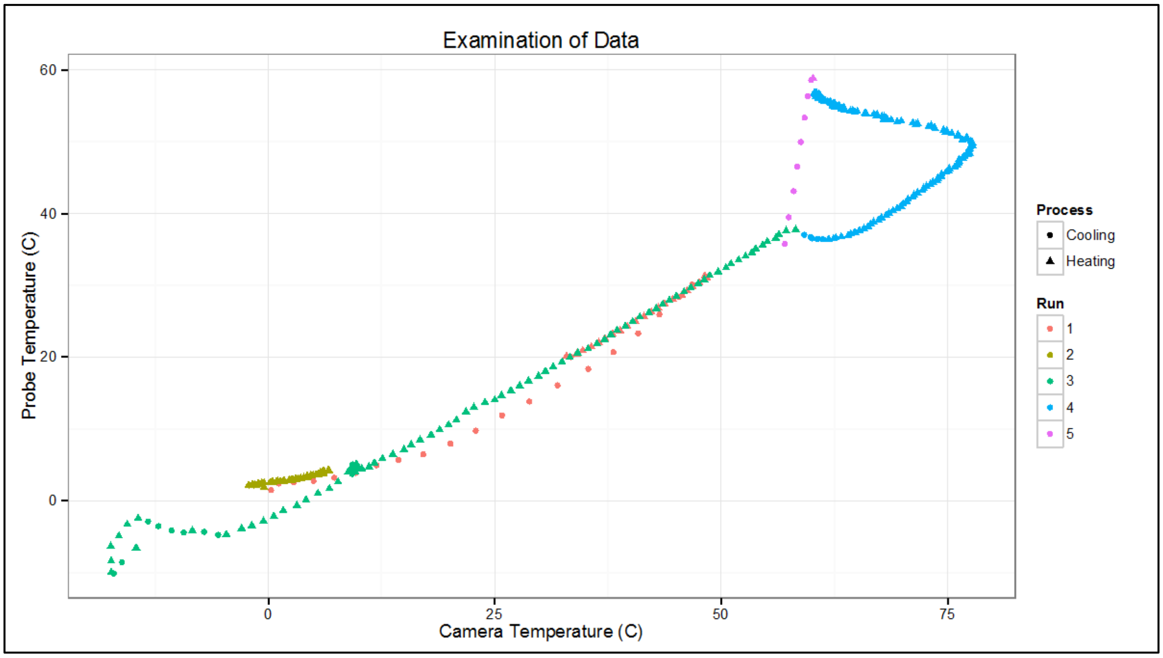

Figure 30: Scatterplot showing temperature as measured by the probe and camera. Triangles indicate measurement recording during heating. Circles indicate measurement recorded during cooling. Each run is uniquely colored.

Portions of the relationship between the sensors expressed in Run 4 defy explanation. At 19:02 on March 17th the heating element was turned off. The probe records declining temperatures at 19:09. However, by 19:34 the temperature (as measured by the probe) is again increasing. The instrument records increasing temperatures for the remainder of Run 4. The camera does not record decreasing temperatures between 19:09 and 19:34. At 19:19 the camera records its lowest recorded temperature increase, .03° C, during this period. At 23:59 the camera again begins recording decreasing temperatures and does so until the end of Run 4 in direct contradiction to the data recorded by the probe. This portion of Run 4 must have some recording errors by one of the sensors. Run 5 was a cooling run. It shows a linear relationship between the sensors. This relationship does not agree with the cooling portion of Run 1.

8.1.2 THERMAL CONDUCTIVITY OF DELRIN AND ITS EFFECTS ON RECORDED TEMPERATURES

As earlier noted, instances of camera temperatures lagging probe temperatures are likely a consequence of the nature of heat conduction. A typical timescale in terms of seconds, t, for heat to diffuse through a body is given by:

$$t = \frac{x^2}{\alpha} \tag{1}$$

where x is the body's thickness measured in meters and α is the thermal diffusivity of the body in terms of $m^2\ s^{-1}$. Thermal diffusivity is defined as the ratio of a substance's thermal conductivity to its capacity to store thermal energy. In equation form:

$$\alpha = \frac{k}{\rho c_p} \tag{2}$$

In (2) k is thermal conductivity in units of $W\ m^{-1}\ K^{-1}$, ρ is density in units of $kg\ m^{-3}$, and c_p is specific heat in units of $J\ kg^{-1}\ K^{-1}$. The Delrin being measured was ½" (.0127 m) thick and had a thermal diffusivity of $1.72 \times 10^{-7}\ m^2\ s^{-1}$. The resulting characteristic time scale for heat to diffuse throughout the Delrin is about 15 minutes. The temperature probe was only ¼" from the coolant. The characteristic time scale for heat to be sensed by the temperature probe is about 4 minutes.

This results in an approximately 11 minute lag between when the probe and the camera sense the same input energy. In this study 11 minutes represents approximately two time steps in measurements. This implies that a correction may be made by lagging the camera temperature relative to the probe temperature.

However, thermal conductivity is itself dependent on temperature. This in turn means thermal diffusivity and the characteristic time scale for heat to diffuse through a body are also temperature dependent. The temperature dependency implies that any possible correction made by time lags will be non-constant. Data obtained from DuPont and the vendor for the Delrin 150 used in this study did not include a description of the temperature dependence of the thermal conductivity of Delrin 150 acetal. For this analysis a constant two step (10 minute) time lag between the camera and probe temperature readings is assumed.

As mentioned before, a portion of Run 4 recorded increasing probe temperatures and decreasing camera temperature. This is likely a recording error. The data are excluded from the analysis. The same phenomenon is expressed at the beginning of Run 3. The data are excluded from the analysis. Run 5, as a standalone dataset, is too small to be statistically robust (seven data points after the time lag adjustment is made). Additionally, even after applying the time lag Run 5 displays a different pattern than the remainder of the data. This raises questions about the appropriateness of a two time step lag for these seven points. The data are excluded from the analysis. After applying the time lag adjustments, the cooling portion of Run 1 continued to display a non-linearity that is believed to be correctable by applying an appropriate correction for thermal inertia. No data upon which to base a correction are available from the Delrin manufacturer or vendor. That portion of the data set is assumed to be a recording error and is excluded from the analysis. After applying the time lag adjustments a portion of Run 3 (as mentioned earlier) passed through a brief period of heating and cooling that resulted in a non-linearity that is believed to be correctable by applying an appropriate correction for thermal inertia. No data upon which to base a correction are available from the Delrin manufacturer or vendor. That portion of the data set is assumed to be a recording error and is excluded from the analysis.

8.1.3 EFFECTS OF GERMANIUM WINDOW

The germanium window temperature stayed fairly constant during the time period this report addresses. Measurements were taken at five-minute intervals with a thermocouple. The range of temperatures varied approximately 1.7 K. The camera, in its ventilated housing, was on the entire time in question. As shown in Figure 6, the window temperature trend in Run 2 is unique in this group. Run 2 was conducted during time periods analogous to portions of Runs 3 and 4. This implies that any effects of the lab's HVAC system or other heat sources that vary with time on the window temperature should be similar for these runs. There was no on site monitoring during Run 2. It is possible that conditions in the lab during Run 2 were distinct from those during the other runs. That suggests that, by the statistical meaning, Run 2 data are from a population distinct from those of the other runs. The data are excluded from the analysis.

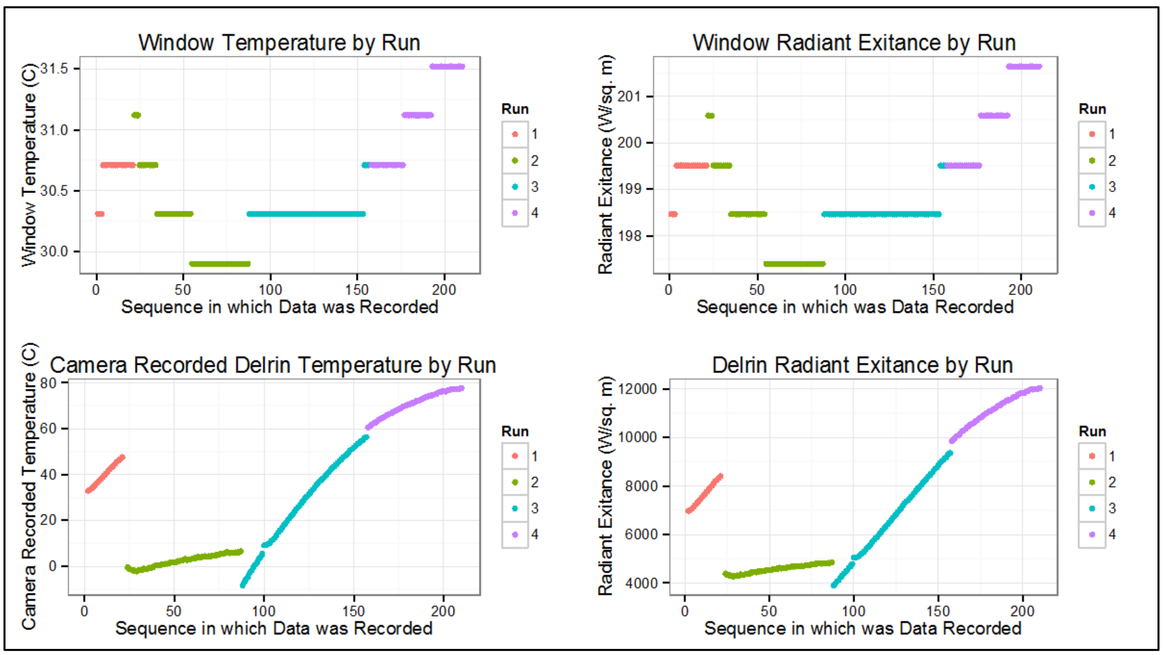

Figure 31: The window temperature trend in Run 2 is distinct from that of the other runs.

8.1.4 STATISTICAL ANALYSIS

Figure 32 shows a scatterplot of the data to be used for the statistical analysis. Initially a simple linear regression was taken as the model. The data were separated by run and evaluated both on a per run basis and as a full set. Probe temperature readings (T_{Probe} in units of degrees Celsius) were regressed on the lagged camera temperature (T_{Cam} in units of degrees Celsius) readings.

Each run and the full set were investigated to check for violations of the basic assumptions (linearity, constant variance, normality, independence) used to justify statistical statements based on a regression analysis. A review for serial correlation was also undertaken. This process was repeated for a fuller model that sought to correct for violations of assumptions so as to allow for a more reliable quantification of the uncertainty involved in the regression analysis.

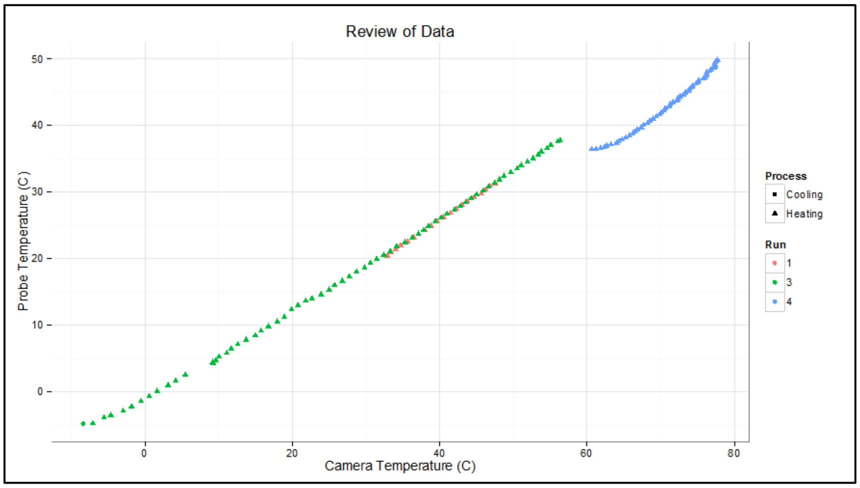

Figure 32: A scatterplot of the data used in the statistical analysis.

The initial model, model 6, is:

$$\mu\{T_{Probe}|T_{Cam}\} = \beta_0 + \beta_1 T_{Cam} \tag{3}$$

The fuller model, model 7, is:

$$\mu\{T_{Probe}|T_{Cam}\} = \beta_0 + \beta_1 T_{Cam} + \beta_2 T_{Cam}^2 \tag{4}$$

8.1.4.1 LINEARITY

A graphical analysis confirms that all runs display a linear relationship between the recorded probe temperatures and the lagged camera recorded temperatures. A more formal Lack-of-Fit F-test can't be applied here to quantify the appropriateness of the simple linear regression model because there is a maximum of one measurement for each value of the explanatory variable.

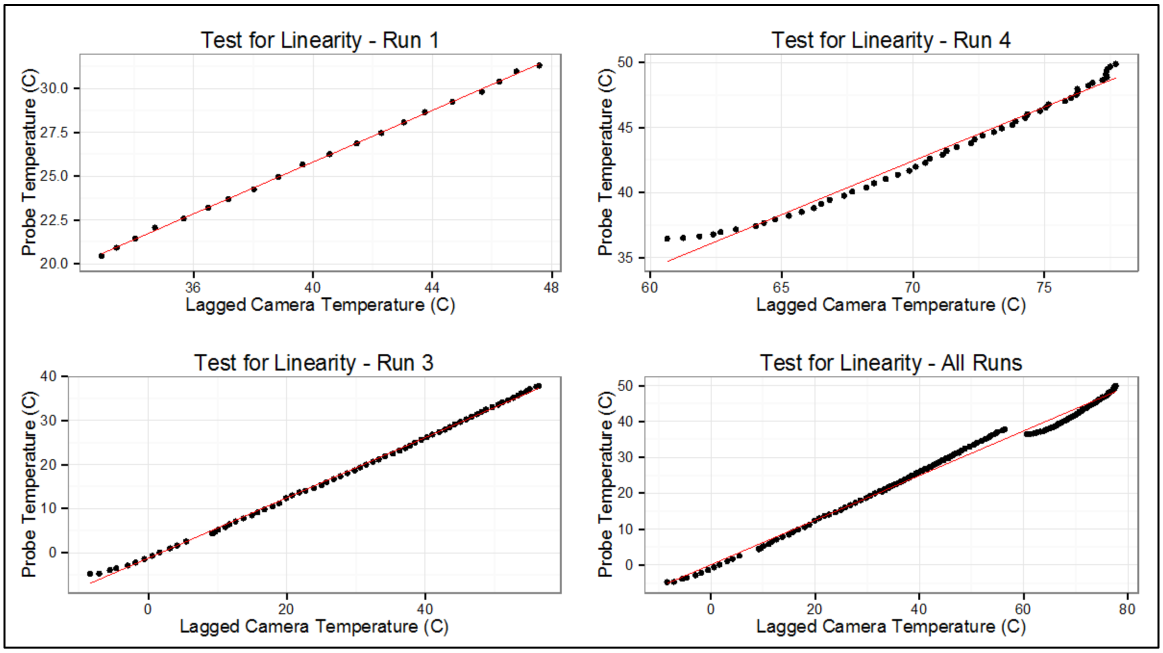

Figure 33: A graphical analysis confirms all runs display a linear relationship between the recorded probe temperatures and lagged camera recorded temperatures.

8.1.4.2 CONSTANT VARIANCE

As shown in Figure 34, model (6) Run 1 residuals show a random distribution about the fitted line consistent with the distribution expected to satisfy the assumption of constant variance. Runs 3 and 4 show an ordered pattern with residuals above the fitted line at high and low temperatures and below the fitted line at temperatures in between. Not satisfying the equal spread assumption causes standard errors derived from the regression to be inaccurately described. As shown in Figure 35, adding a term to the model appears to result in equal variances about the regression line on a per run basis, but not for the whole dataset. Although, Run 4 may have violations.

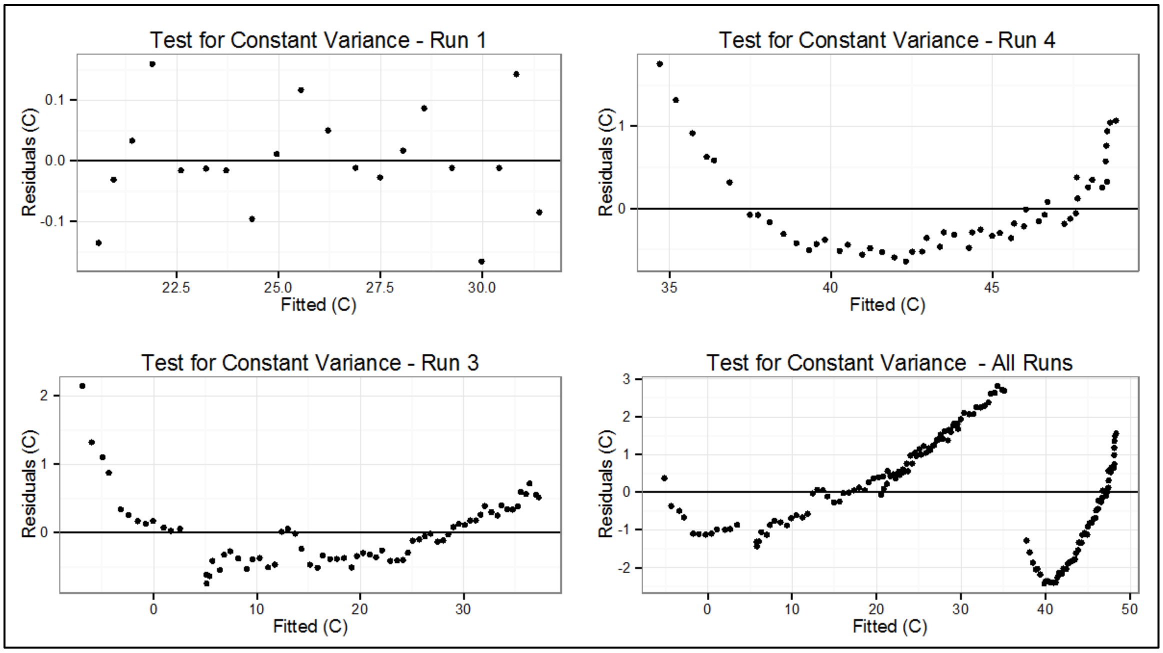

Figure 34: Graphical review of variance for model (6).

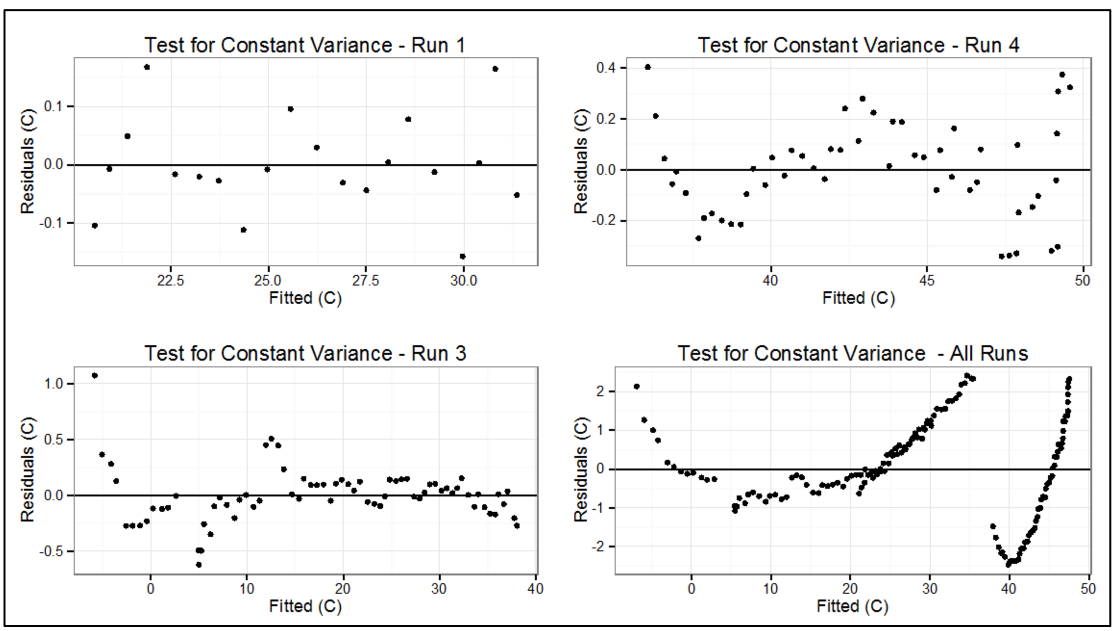

Figure 35: Graphical review of variance for model (7).

8.1.4.3 NORMALITY

Model (6) Run 1 residuals and residuals from the whole dataset show a long-tailed distribution. Runs 3 and 4 show a skewed distribution. These plots are evidence of a non-normal distribution. Coefficient estimates and associated standard errors are robust to non-normal distributions. However, prediction intervals are not valid. Model (7) results in long-tailed distribution for the whole set but well behaved runs.

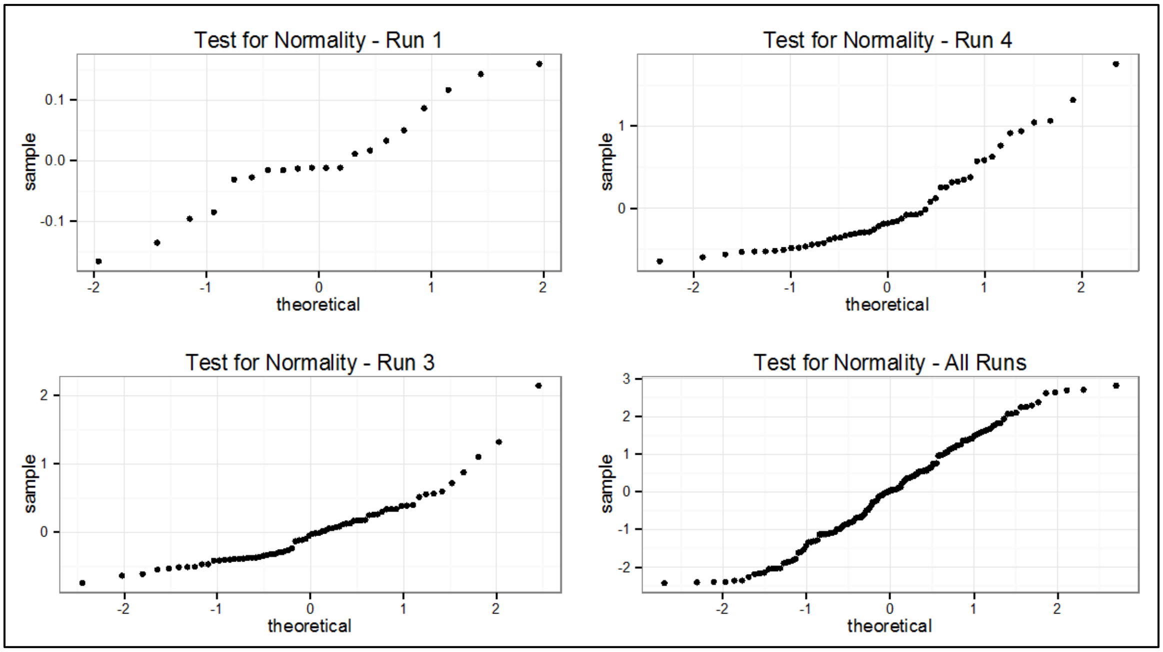

Figure 36: Graphical review of the normality of the distribution for model (6).

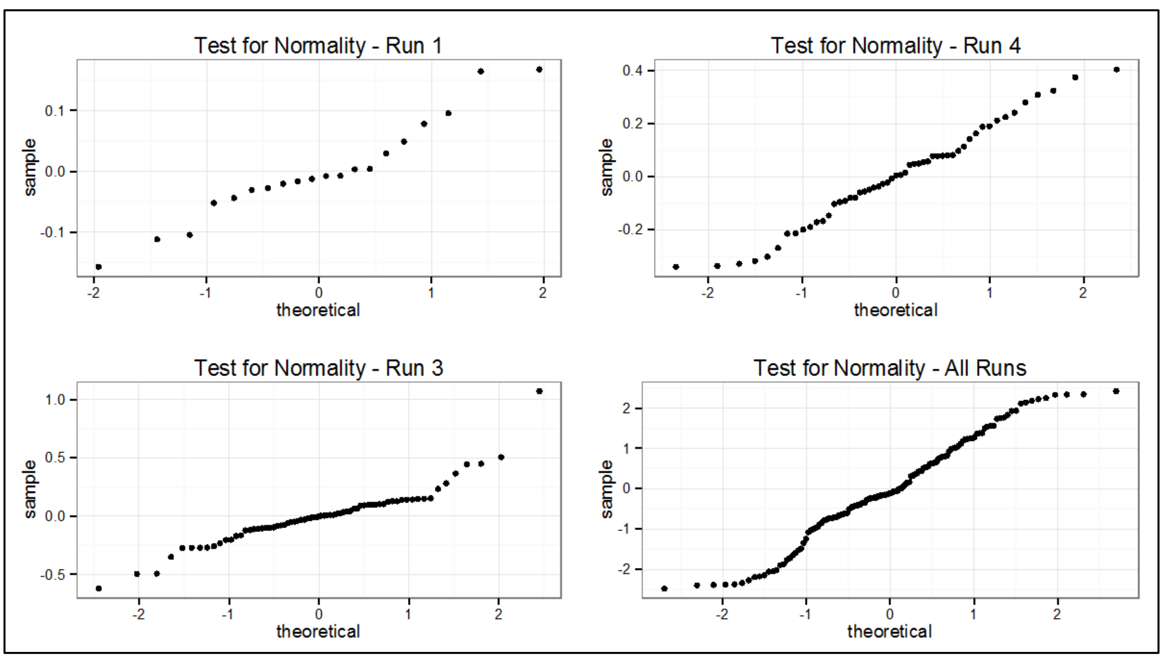

Figure 37: Graphical review of the normality of the distribution for model (7).

8.1.4.4 INDEPENDENCE/SERIAL CORRELATION

Model (6) Run 1 residuals display no particular pattern, so no serial correlation is indicated. Runs 3, 4, and the entire dataset have obvious runs above and below the regression line. Serial correlation is indicated for these runs and the assumption of independence is not satisfied. Standard errors derived from these regressions may underestimate the true variation in the sample average. Model (7) displays the same serial correlation trends as model (6).

Serial correlation is present, so any standard errors associated with coefficient estimates of either of the regression models will be underestimated. These standard errors must be corrected using a serial correlation coefficient. Determining which correlation coefficient to use (corresponding to first or higher order autoregressive models) was accomplished graphically based on a partial autocorrelation function analysis. A first order autoregressive model is appropriate for runs 3, 4, and the whole dataset. The correction factor for the standard errors of the coefficient estimates for runs 3 and 4 was on the order of 2 (standard errors were about twice as large as reported by the regression model) and for the whole set was on the order of 5 (standard errors were about five times as large as reported by the regression model).

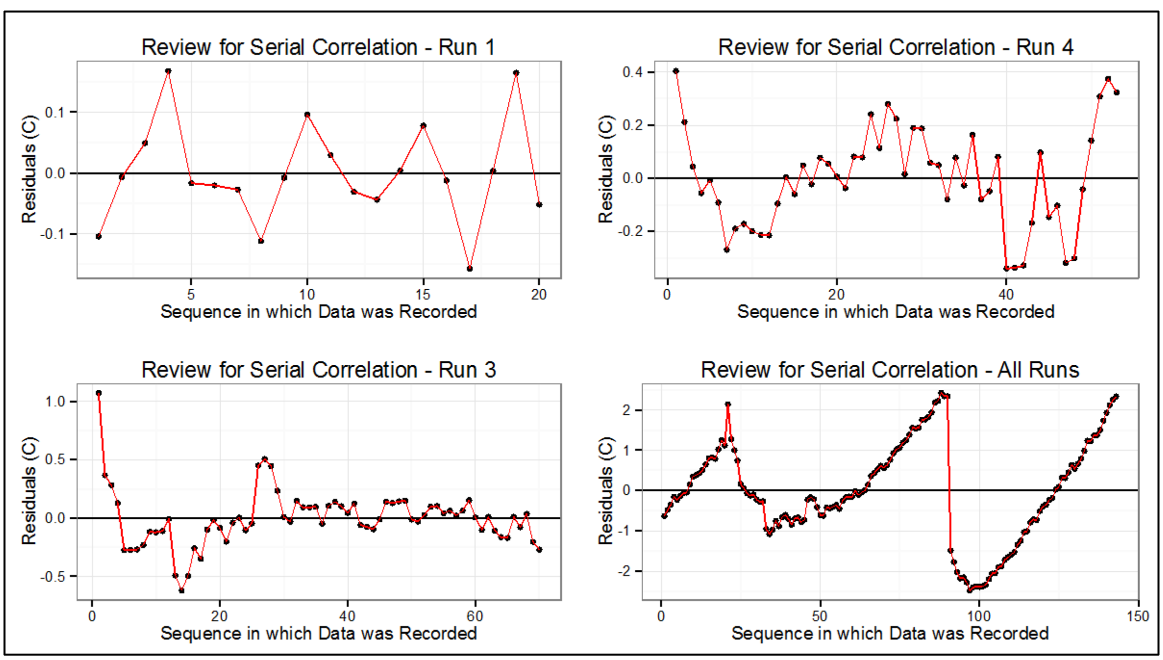

Figure 38: Graphical review for serial correlation for model (6).

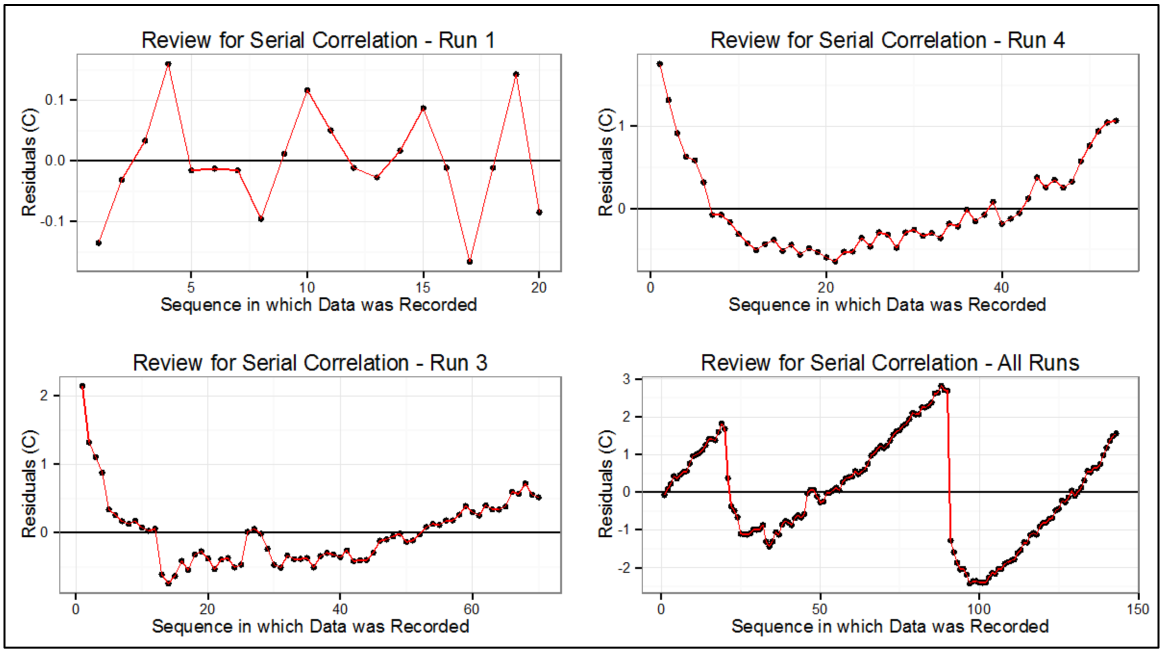

Figure 39: Graphical review for serial correlation for model (7).

8.1.5 REVIEW OF REFLECTED RADIANT EXITANCE ASSUMPTION

It was assumed that by carefully choosing the pixels in the thermal image created by the camera the analysis avoided the necessity of including effects of radiant exitance reflected off of the Delrin base and sensed by the camera. The pixels chosen did not contain a reflection of the camera itself, but it is possible the Delrin base reflected the radiant exitance of portions of the Delrin tube. In an attempt to better account for non-linearity in the relationship between the temperatures recorded by the two sensors, a review of the data was conducted based on a Delrin temperature derived from the following equation:

$$\left[\frac{T_{CAM}^4 - \tau_W(1-\varepsilon_D)T_R^4 - (1-\tau_W)T_W^4}{\tau_W \varepsilon_D}\right]^{\frac{1}{4}} = T_D \qquad (5)$$

Equation (5) retains the term, not present in equation (3) from section 2.1.2, that accounts for the temperature, T_R in units of Kelvin, of the surrounding environment reflected off of the Delrin base.

To arrive at T_R, the probe temperature was used as a proxy for the surface temperature of the Delrin tube. The tube was ¼" thick and the probe was inserted in the Delrin base approximately ¼" from the coolant. The temperature at which the portion of the tube submerged in the coolant emitted is assumed to be equal to the probe temperature. This assumption is supported by properties associated with heat conduction already addressed in this report. A statistical analysis of the data that included the reflected term revealed that all the trends associated with models (6) and (7) previously discussed were evident in this modified set of data. Figure 40 shows the only evident change, an offset (y-intercept) shifted upward when compared to the other set of data.

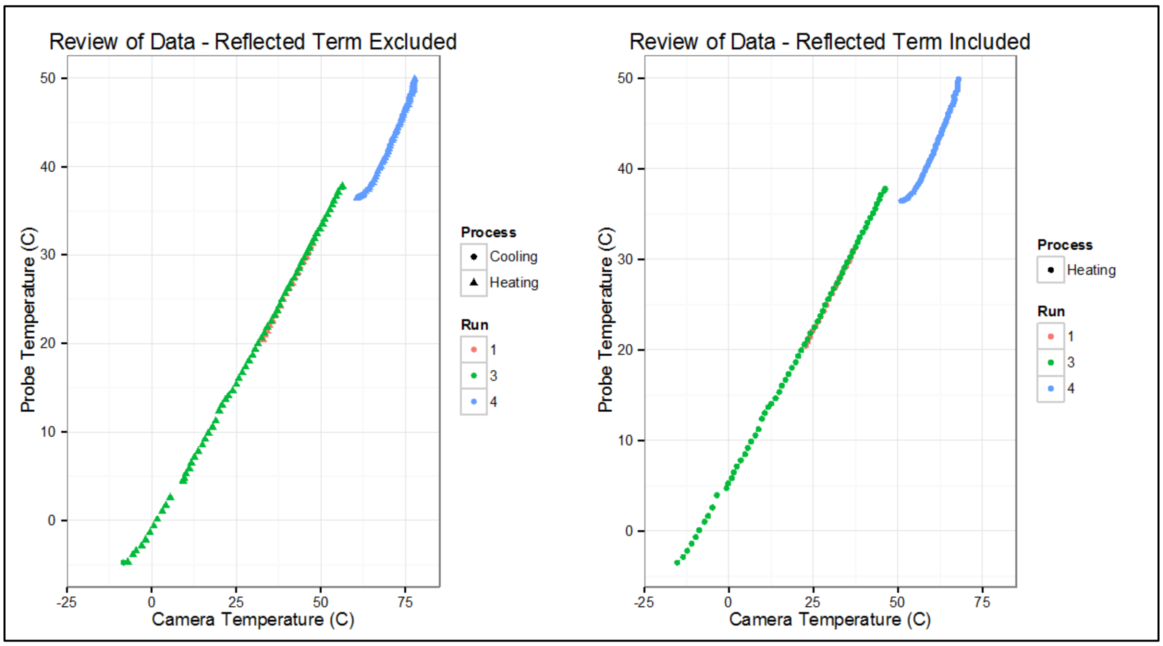

Figure 40: Scatterplots of the data analyzed. The plot on the left excluded the reflected term. The plot on the right includes the reflected term.

8.1.6 RESULTS

The results from model 6, $\mu\{T_{Probe}|T_{Cam}\} = \beta_0 + \beta_1 T_{Cam}$, are shown in Table 2 and Table 3. Reliable estimates of uncertainty can be provided only for Run 1.

	B_0	STANDARD ERROR (C)	B_1	STANDARD ERROR (C)
RUN 1	-3.69	0.17	0.74	0.004
RUN 3	-1.18	NA	0.68	NA
RUN 4	-15.50	NA	0.83	NA
FULL SET	0.08	NA	0.62	NA

Table 2: Model 6 regression results. The results are for the dataset that excluded the reflected exitance term. NA indicates that no reliable estimate could be made.

	B_0	STANDARD ERROR (C)	B_1	STANDARD ERROR (C)
RUN 1	3.74	0.13	0.74	0.004
RUN 3	5.67	NA	0.68	NA
RUN 4	8.28	NA	0.84	NA
FULL SET	6.59	NA	0.61	NA

Table 3: Model 6 regression results. The results are for the dataset that included the reflected exitance term. NA indicates that no reliable estimate could be made.

The results from model 7, $\mu\{T_{Probe}|T_{Cam}\} = \beta_0 + \beta_1 T_{Cam} + \beta_2 T_{Cam}^2$, are shown in Table 4 and Table 5.

The results indicate that including the reflected radiant exitance term in the camera derived Delrin temperature mainly had an impact on the offset (y-intercept) of the regression line. The term did not help explain the non-linearity in the probe/camera temperature relationship.

	B_0	STANDARD ERROR (C)	B_1	STANDARD ERROR (C)	B_2	STANDARD ERROR (C)
RUN 1	-5.25	1.73	0.82	0.09	-0.001	0.0011
RUN 3	-0.78	0.12	0.61	0.01	0.001	0.0002
RUN 4	94.23	11.92	-2.33	0.34	0.023	0.0024
FULL SET	-0.94	NA	0.70	NA	-0.001	NA

Table 4: Model 7 regression results. The results are for the dataset that excluded the reflected exitance term. NA indicates that no reliable estimate could be made.

	B_0	STANDARD ERROR (C)	B_1	STANDARD ERROR (C)	B_2	STANDARD ERROR (C)
RUN 1	3.57	0.96	0.75	0.06	0.000	0.0011
RUN 3	5.63	0.04	0.64	0.00	0.001	0.0001
RUN 4	85.92	9.87	-2.31	0.33	0.026	0.0027
FULL SET	6.01	NA	0.69	NA	-0.001	NA

Table 5: Model 7 regression results. The results are for the dataset that included the reflected exitance term. NA indicates that no reliable estimate could be made.

In attempting to meet the four basic assumptions that justify conclusions based on a linear regression model, the statistical analysis indicated the need to add a term that included the camera derived Delrin temperature squared (see model 7). This added term seems to address the observation stated in the introduction that provided the impetus for this study. During times of increasing temperatures the camera reported temperatures that, in general, increased at a greater rate and arrived at a greater maximum than those returned by other sensors measuring the same object. A simple linear relationship between the two sensors does not account for the non-constant difference between measured rates of temperature change. However, the temperature-squared term can account for a varying response in the camera recorded temperature encountered in the field. If the coefficient associated with the temperature-squared term is negative (as in model 7 Run 1 reflected term excluded and both full dataset regressions for model 7), as the camera measured temperature and its rate of change increase the correction to the camera measured temperature accounts for that response and offsets it. A similar correction (depending on the sign of the coefficient) occurs as the temperature decreases.

An extra sum of squares (ESS) F-test was used to provide evidence about whether the difference in the sums of squared residuals between the fuller model 7 and simpler model 6 is greater than can be explained by chance variation. That is to say, it was used to provide evidence that can be used to justify adding a term to a regression model and against a suspicion of over fitting the model. The test results are reliable only if both models meet the basic regression assumptions. In this study, this test can only be applied to Run 1. The test provided no evidence that the temperature-squared term in Run 1 should be retained (ESS F-test, p-values .38 and .86). However, Run 1 did not include any of the most extreme temperatures encountered during the study, and conclusions based on data from Run 1 are supported statistically only for the range of temperatures encountered in Run 1.

The statistical analysis seemed to support the simple linear relationship displayed in Figure 4. All model 6 results were applied to the data during the proof of concept to determine best fit with the physical system. The best fit was the full model 6 that included the camera's radiant exitance term (see equation 2 and Table 3). The calibration function used is the following:

$$T_{Probe} = 6.59 + .61T_{Cam} \tag{21}$$

In this case T_{Cam} is equivalent to T_{fol} from equation 15 from 3.3.1.2. The calibration is applied after all the filtering described in section 3.3.1 is carried out so that the relationship used to determine the foliage canopy temperature, T_{fol}, is the following:

$$T_{fol} = 6.59 + .61\left[\frac{T_{cam}^4 - \rho_{fol}\tau_{atm}\tau_{win}\left(\frac{M_{sky}}{\sigma\varepsilon_{atm}}\right) - \varepsilon_{atm}\tau_{win}T_{atm}^4 - \varepsilon_{win}T_{win}^4}{\varepsilon_{fol}\tau_{atm}\tau_{win}}\right]^{\frac{1}{4}} \tag{22}$$

8.1.7 CONCLUSIONS

Properties and effects associated with heat transfer were not dealt with in a satisfactory way in this study. For example, neither the Delrin manufacturer nor its vendor was able to provide information about how that material's thermal conductivity changed with respect to temperature. This led to the assumption that time lags (see appendix section 8.1.2 for full explanation) between camera recorded temperatures and probe recorded temperatures were constant, and data that did not appear to agree with this assumption were excluded from analysis. There was a small pump in the refrigeration unit. Convective heat transfer was not addressed at all in this analysis. Better material data and a more accurate treatment of heat transfer may have resulted in clearer results.

The FLIR SC305 camera displayed a non-linear response to temperature changes during field use. Using a calibration function model with a temperature-squared term addressed effects associated with that observation. This study produced no statistical evidence to support adding such a term. For model 6 only Run 1 produced data that met the assumptions necessary to justify statistical conclusions based on linear regression. For model 7 Runs 1, 3, and 4 produced data that met the assumptions necessary to justify statistical conclusions based on linear regression. The data in Run 4 differed significantly from that in Runs 1 and 3. Data from Runs 1 and 3 largely agreed. These at times contradictory conclusions indicated a need to apply the calibration functions developed in this study to data collected with this TIR camera to determine their goodness of fit.

9 GEOPROCESSING RESULTS

9.1 A NOTE ON THERMAL REFLECTIVITY

Figure 13 shows ‘hot spots’ in the upper regions of Watershed 1. As can be seen in Figure 2, these hot spots are actually outcroppings of bare rock. The explanation for the temperature difference is based on the differences in thermal properties between the rocks and the foliage canopy. Comments on the HJ Andrews website and a study of the geology of HJ Andrews Experimental Forest (Swanson, 1975) seem to confirm these outcrops are basalt. Basalt has a thermal reflectivity of .28 (Engineering Toolbox, 2015). This is much higher than the thermal reflectivity of .02 for the foliage canopy in the watershed. No attempt was made to mask these outcrops from the image or to apply a variable emissivity to the thermal imagery.

The camera measures the amount of incoming longwave radiation and assigns a temperature to each pixel in the image based on this information. Equation 11 form 3.3.1.2, defining the amount of reflected longwave radiation sensed by the camera, shows why the difference in thermal reflectivity is important.

$$M_{ref} = \rho_{fol}\tau_{atm}\tau_{win}\left(\frac{M_{sky}}{\sigma\varepsilon_{atm}}\right)$$

Increasing ρ_{fol} from .02 to .28 increases the amount of incoming longwave radiation the camera senses by an order of magnitude. This is what causes the rocks to look brighter than the foliage. There is a corresponding decrease in the amount of thermal longwave radiation emitted by the rocks, but changing the emissivity value from .98 to .72 does not decrease that term’s contribution by an order of magnitude. The nighttime temperature difference between the rocks and the foliage canopy is on the order of 2 K.

9.2 GEOPROCESSING TOOL STRENGTHS

The output image maintained the integrity of the data. The minimum and maximum temperatures did not change between the filtered and corrected camera image and the geoprocessed camera image. Prominent features in the output image coincide spatially with their counterparts in the base map imagery in Figure 13. Some analysis on this dataset is concerned with vertical profiles of temperature and potential temperature in the watershed. The root mean square error for the location of each pixel in the geoprocessed file is 29 m (23 m for the wider angle lens mentioned in section 2.2.2). There are some areas in Watershed 1 where uphill slopes exceed 70°. A 29 m error may correspond with nearly the same vertical rise. At a typical value for the saturated adiabatic lapse rate of 6.5 K km^{-1}, the 29 m elevation error can approximately correspond to a .2 K temperature variation. This is well within the uncertainty involved with the sensors involved in the study.

9.3 GEOPROCESSING TOOL WEAKNESSES

The input raster size was 320 x 240 pixels. The output raster size is 1133 x 657. Exactly 400,340 of the values in the output raster are simply background values that exist to maintain the rectangular shape of the raster after the image was warped. These background values are not displayed in Figure 13. The remaining number of pixels is approximately 4.5 times larger than the original number. The discrepancy is based on two facts. Firstly, the geoprocessing routine in ENVI only accepts a constant physical dimension for the input pixel size. As the image is warped to match its map coordinates the pixels change size. Secondly, from the camera's perspective there are portions of the watershed that are not visible. The ENVI routine compensates for this fact by using nearest neighbor (method is user specified) spatial interpolation. While the proof of concept portion of this study was able to compare camera derived temperatures to values from a pyrgeometer and air temperature sensors, there were no sensors *in situ* in the areas not seen by the camera. Therefore there is no way to evaluate the interpolated camera derived temperatures for accuracy.

9.4 SUMMARY AND CONCLUSIONS

The errors reported in section 9.2 suggest that the selected thermal imagery geoprocessing workflow produced results that are accurate. The root mean square error calculated for the results provides a level of certainty that spatial inaccuracies will have a very small effect on any temperature based calculations. A time series dataset of spatially referenced foliage canopy temperatures in Watershed 1 has been produced and uncertainties involving its spatial accuracy and sensors providing the data are known. This dataset can be a basis for further analysis.